Universitat Autònoma de Barcelona

Electronic properties of organic semiconductors and low-dimensional materials

Desanka BOSKOVIC

Universitat Autònoma de Barcelona

Doctoral Thesis

Electronic properties of organic semiconductors and low-dimensional materials

Thesis submitted to obtain the degree of
Doctor of Philosophy
in the program

Doctorat en Química

at the Departament de Química
of the Facultat de Ciències
of the Universitat Autònoma de Barcelona

Defined by:
Desanka BOSKOVIC

Supervisor:
Pablo ORDEJÓN RONTOMÉ

Tutor:
Mariona SODUPE ROURE

Institut Català de Nanociència i Nanotecnologia, ICN2
Consejo Superior de Investigaciones Cientficias, CSIC
Institut de Ciència de Materials, ICMAB - CSIC
Campus UAB-Bellaterra. Spain

2017

Mami i tati

Acknowledgements

Undertaking this PhD has been a truly life-changing experience for me and it would not have been possible to do without the support and guidance that I received from many people.

Foremost, I would like to express my special appreciation and thanks to my thesis advisors Pablo Ordejón and Enric Canadell for their selfless time and patience, for their motivation and immense knowledge. Without their guidance this Ph.D would not have been achievable.

Many thanks also to Prof. Miljenko Perić who convinced me during our many discussions in Belgrade that I should pursue my doctoral degree and who believed in me from the first day.

I gratefully acknowledge the funding sources that made my Ph.D. work possible: the JAEPre Ph.D fellowship from CSIC and the resources from MINECO Grant $FIS2012-37549\text{-}C05\text{-}02$. For the computing time I would like to acknowledge the resources of the MARENOSTRUM supercomputer, provided by the Barcelona Supercomputing Centre (BSC) through a grant from Red Española de Supercomputacion (RES).

My sincere thanks goes to Frank for all the inspirational discussions and invaluable advices during our work on rubrene. I would also like to thank to my group mates: Richard, Ermin, Miguel Ángel, Carlos, Mikaël, Rafa and Jose for all those great moments and for all the fun we have had working together. Thank you for making the work on my thesis enjoyable. My thanks go out to Roberto and Miguel for their great advices and assistance with my calculations. To Stephan and all the people from theory groups of ICN2 and ICMAB for helpful discussions and for their friendship during all these years. Although they were not present from the beginning of my Ph.D, I would also like to thank to Anna Paola, Francisco, Ramón, Ruben, Lorenzo, Francesca, Bernd, Sergio and Bogdan for being there for me in the last years of my thesis.

I am indebted to all my friends in Barcelona who were always so supportive and helpful in numerous ways. Special thanks to Nataša, Ana, Marko, Olja, Jovana, Igor, Mici, Radmila, Miloš, Valentina, Neda, Dina and Uroš.

Lastly, I would like to thank to my family for all their love and encouragement. To my parents who raised me with a love of science and supported me in all my pursuits and to my brothers Dejan and Dušan who taught me how to survive in this wild world. Thank you.

Index

1 Introduction **1**

2 Theoretical background **3**

2.1 Electronic Structure 3

2.2 Density Functional Theory 6

2.2.1 Hohenberg and Kohn theorems 6

2.2.2 Kohn-Sham equations 7

2.2.3 Exchange correlation approximation 8

2.2.4 The SIESTA method 9

2.3 Tight binding approximation 12

2.4 Phonons and electron-phonon coupling 15

2.5 Charge Density Waves and Lindhard response functions 20

3 Electron-phonon coupling in rubrene **25**

3.1 Introduction 25

3.2 Vibrational properties of rubrene 26

3.3 Electron-phonon coupling 30

3.4 The tight-binding calculations 33

3.5 Flipping motion of phenyl groups 37

3.6 Conclusion 40

4 Monophosphate Tungsten Bronzes **41**

4.1 Introduction 41

4.2 Electronic structure of $MPTB_p$s 43

4.3 Fermi surface and nesting vectors 45

4.4 Lindhard response function calculation 51

4.4.1 $MPTB_p$ with $m = 4$ 51

4.4.2 $MPTB_p$ with $m = 5$ 55

4.4.3 $MPTB_p$ with $m = 6$ . . . 59
4.4.4 $MPTB_p$ with $m = 7$ . . . 63
4.4.5 $MPTB_p$ with $m = 8$ . . . 66
4.4.6 $MPTB_p$ with $m = 12$ . . . 69
4.5 Conclusion . . . 72

5 Group V transition metal oxides and chalcogenides 75
5.1 Introduction . . . 75
5.2 $Sr_5Nb_5O_{17}$ . . . 76
5.3 $2H\text{-}NbSe_2$ . . . 84
5.4 $TaTe_4$ . . . 90
5.5 Ta_2NiSe_7 . . . 97
5.6 Conclusions . . . 104

6 Conclusions 107

References 111

Appndx A Electron-phonon coupling in rubrene 129

Appndx B Molecular dynamics simulations 131

Appndx C Lindhard response function calculation at finite temperatures 133

Chapter 1

Introduction

The knowledge of the electronic structure of solid materials is crucial for the understanding of their properties. In the last decades there was a great progress in the investigation of electronic structures, but our knowledge is still far from being complete. As in his talk *"There's a plenty room at the bottom"* 1959 in Pasadena the Nobel prize winner Richard Feynman pointed out, the things would have enormously grater range of possible properties if we had some control of their arrangement in the atomic scale. This prediction was based on the novel electronic properties arising in quantum mechanics when the electron is confined in the scale of its wavelength. Even if the production of miniature devices was starting to take place at this time, it took four decades to be able to walk through the path opened by this visionary talk.

Organic semiconductors gained significant scientific interest driven by many technological applications such as organic light emitting diodes (OLEDs), organic transistors and photovoltaic applications [1]. The reason for efficient application of organic semiconductors lies in their good charge-transport properties and there is a great effort in improvement of their carrier mobilities [2, 3]. Charge transport in these materials usually shows different behaviour comparing to conventional inorganic semiconductors. Therefore, understanding of several properties of these complex materials and complete quantitative characterization of their transport properties is still a challenging tusk.

Low dimensional materials are systems in which electronic state wavefunction is confined, at least in one of the three dimensions. Electronic confinement generally appears in the range from 1 nm to 100 nm, which gives rise to quantum size effects and alters their electronic properties. Low dimensional systems have shown a wide range of intriguing phenomena and extraordinary electronic, optical, thermal, mechanical and chemical properties.

There has been a great interest in low-dimensional transition metal materials in the past decades. They are extensively studied because of their specific electric, magnetic and

structural properties which originate from the possibility to obtain partial oxidation states of the transition metal atoms [4, 5]. Low-dimensional transition metal materials often show structural and electronic instabilities which lead to anomalies in their transport properties. Some of them such as monophosphate tungsten bronzes $MPTB$ or $NbSe_2$, became a subject of an intensive study because they are showing phase transitions which lead to the formation of charge density waves (CDWs) [6].

In this thesis we are going to study several aspects of the electronic properties of some organic semiconductors and low dimensional materials.

- In the Chapter 2 we briefly describe methodology and theory behind the theoretical calculations of the electronic properties of the studied materials.

- In the Chapter 3 we develop a density functional theory (DFT) model to calculate phonon modes, phonon frequencies and electron-phonon coupling in the rubrene crystal, one of the most widely studied organic semiconductor. In this chapter are also going to be shown our results of the tight binding (TB) calculations of rubrene and a practical way to remove the problem of inaccuracies with the low frequency modes which often occurs in the DFT-based methods.

- In the Chapter 4 we study electronic structure of monophosphate tungsten bronzes with pentagonal tunnels, $MPTB_p$, which are showing phase transitions with a formation of charge density waves (CDWs). In this chapter we report results of the electronic band structure, Fermi surface and Lindhard response function calculation for several $MPTB_p$ phases, with $m = 4, 5, 6, 7, 8$ and 12.

- Finally, in the Chapter 5 we study electronic structure of several low dimensional materials $Sr_5Nb_5O_{17}$, $2H\text{-}NbSe_2$, $TaTe_4$ and Ta_2NiSe_7 and investigate if the Fermi surface nesting is at the origin of the structural and resistivity anomalies exhibited by these compounds. Therefore, here are going to be presented results of their band structure, Fermi surface and Lindhard response function calculation.

Chapter 2

Theoretical background

Density functional theory (DFT) has become one of the the most frequently used methods to study the electronic structure of atoms, molecules and solids [7]. DFT is capable of determining the properties of a many-electron systems starting from the basic equations of electrons. Therefore, DFT can provide a practical way to compute ground-states of very complex systems with even thousands atoms per unit cell. However, the computational cost of DFT methods is still quite big for systems with a few hundreds of atoms, specially for structural optimisations or molecular dynamics simulations.

The formulation of density functional theory started in the mid 1960's with the works of P. Hohenberg, W. Kohn and L.J. Sham [8, 9] and since then, DFT has been in continuous development to deal with new fields of study such as electron transport or superconductivity. Nowadays, DFT is used throughout the world as many different groups have their own DFT-packages. The DFT code used throughout this thesis is SIESTA [10–14].

In this chapter, we are going to explain shortly the DFT method used in this thesis as well as the tight-binding (TB) approach, which we used in the calculation of electron-phonon coupling in rubrene. Here is also going to be explained the method for the calculation of phonons and electron-phonon coupling in rubrene. At the end of this chapter, we are going to show the theoretical background we used for the Lindhard response function calculation.

2.1 Electronic Structure

For the calculation of electronic structure of solids we will have to solve the Schrödinger equation. For the real system, which is consisting of many electrons, this is representing the

quantum mechanical problem and cannot be solved exactly because of many variables and complexity of equations. The basic Schrödinger equation is given by:

$$\hat{H}\Psi = E\Psi \tag{2.1}$$

where $\hat{H}$ is the Hamiltonian, Ψ is the wavefunction and E is the energy. Solving the time independent problems in quantum mechanics requires the solving of time independent Schrödinger equation and finding the wave functions and the corresponding eigenvalues:

$$\hat{H}\Psi_i(\vec{r}_1.....\vec{r}_n;\vec{R}_1.....\vec{R}_m) = E_i\Psi_i(\vec{r}_1.....\vec{r}_n;\vec{R}_1.....\vec{R}_m) \tag{2.2}$$

where $\hat{H}$ is the non relativistic Hamiltonian operator for the system formed of n electrons and m nuclei with the spatial coordinates $r_1.....r_n$ and $R_1.....R_m$ respectively. This operator is not considering the spin degrees of freedom and is given with the equation:

$$\begin{aligned}\hat{H} = -\frac{\hbar^2}{2m_e}\sum_{\nu=1}^{n}\nabla_\nu^2 - \sum_{\mu=1}^{m}\frac{\hbar^2}{2M_\mu}\nabla_\mu^2 - \sum_{\mu,\nu=1}^{m,n}\frac{Z_\mu e^2}{|R_\mu - r_\nu|} + \\ + \sum_{\nu<\nu'}^{n}\frac{e^2}{|r_{\nu\nu'}|} + \sum_{\mu<\mu'}^{m}\frac{Z_\mu Z_{\mu'} e^2}{|R_{\mu\mu'}|} + \hat{V}_{ext} = \\ \hat{T}_e + \hat{T}_N + \hat{V}_{Ne} + \hat{V}_{ee} + \hat{V}_{NN} + \hat{V}_{ext}\end{aligned} \tag{2.3}$$

The first two terms in the equation (2.3), $\hat{T}_e$ and $\hat{T}_N$, represent the kinetic energy of the electrons and nuclei respectively, and the next terms are dealing with the interactions between electrons and nuclei: the third term, $\hat{V}_{Ne}$ corresponds to the attraction between electrons and nuclei, fourth and fifth terms, $\hat{V}_{ee}$ and $\hat{V}_{NN}$, are repulsive electron-electron and nuclei-nuclei interactions, respectively, and the last term in the equation (2.3), $\hat{V}_{ext}$, is any other external potential, for example, electric or magnetic field, if any.

It is clear that even for the isolated atoms (except for hydrogen atoms) the analytical solution of such a complex equation as equation (2.3) would be impossible without numerical methods and approximations. The most widely used approximation for the determination of electronic structure of solids is Born-Oppenheimer approximation [15, 16]. By this

approximation, the velocity of electrons is said to be very large compared to the velocity of nuclei ($m_{nuclei} \gg m_{el} \Rightarrow p^2/2m_{nuclei} \ll p^2/2m_{el}$) and thus we can decouple the total wave function in the electronic part and the nuclear part:

$$\Psi(R,r) = \varphi_m^n(R)\Phi_m(R,r) \tag{2.4}$$

where $\varphi_m^n(R)$ is the wavefunction of the nuclei in the nth nuclear state and $\Phi_m(R,r)$ is the wavefunction of electrons in the mth stationary state of the electronic Hamiltonian, equation (2.5):

$$\hat{H}_e = \hat{T}_e + \hat{V}_{ee} + \hat{V}_{Ne} + \hat{V}_{ext} \tag{2.5}$$

The nuclear coordinates R_m enter here just as parameters because the eigenvalues of the electron Hamiltonian depend on the fixed positions of the nuclei. If we denote the electronic eigenvalues as $\varepsilon_m(R)$, we can write:

$$\hat{H}_e\Phi_m(R,r) = \varepsilon_m(R)\Phi_m(R,r) \tag{2.6}$$

After solving the equation (2.6) for the fixed nuclear positions, we would then like to solve the Schrödinger equation for the nuclei taking into account that m can be any electronic state:

$$[T_N + V_{NN} + \varepsilon_m(R)]\varphi_m^n(R) = E_m^n\varphi_m^n(R) \tag{2.7}$$

To find the solution of the equation (2.7) is very hard and another approximation is usually taken for treating big systems: the *classical nuclei approximation* which treats the dynamic of nuclei as classical particles in a potential $\varepsilon_m(R)$ generated by the electrons. Therefore, the movement of nuclei is described by Newton's equations.

In the further text, we will assume these two approximations, concentrating on the solution of the electronic Hamiltonian (2.5). At this point it has to be stressed out that this very difficult many body problem would be impossible to be solved without approximations such as Hartree-Fock (HF), density functional theory (DFT) or others.

In this chapter we will briefly discuss DFT and tight binding (TB) model, as those are the formalisms behind the numerical simulations reported in this work. Both methods are widely used for calculating the electronic structures of materials where DFT as a modern and efficient method is taking a leading role in the last decade.

2.2 Density Functional Theory

Density functional theory was born as an idea of reducing the Schrödinger equation to one-electron problem by choosing one-electron potential. The basic concept of DFT is that any property of a system can be described as a functional of the ground state electron density. In this way, we can reduce our $3N$ variable problem (wavefunction of N interacting electrons) into a 3 variable problem with the electronic density (function of position). In the following text are going to be presented the theorems that prove this statement.

2.2.1 Hohenberg and Kohn theorems

An antecedent of this theory was set up by Thomas and Fermi [17] in their independent works, where the electronic density was taken as the fundamental variable of the many body problem. In 1964 Hohenberg and Kohn [8] presented two theorems considering the electronic density as the fundamental object. They showed that this approach could be used to obtain the exact value for the ground state energy of any system of interacting electrons in the external potential.

Theorem 1: *For any system of interacting particles in an external potential, the external potential is determined uniquely by the ground state particle density, except for a constant.*

COROLLARY: Since the Hamiltonian is known except for a constant, all the many body wave functions (including ground and excited electronic wave functions) are determined by the ground state density $\rho_0(r)$.

Theorem 2: *A universal functional for the energy in terms of the density can be defined that is valid for any external potential. For a particular value of the external potential, the exact ground state energy of the system is the global minimum value of this functional, and the density that minimizes the functional is the exact ground state density.*

COROLLARY: The functional alone is enough to determine the ground state density and energy.

At this point, based on the previous theorems, we can say that we have an exact theory, although it is still abstract. This theory is just telling us that if the functional defined as a function of density is known, then by minimizing the total energy of the system we could find the exact ground state density and energy. However, the functional is not known and the

minimization problem is a complex mathematical problem. The Kohn-Sham ansatz (1965) is giving solutions to these issues.

2.2.2 Kohn-Sham equations

In the Kohn-Sham approach [9] it is assumed that the ground state density of the many body interacting system is equal to that of some non interacting system under the action of some imaginary effective potential. In this way, the many body problem is replaced with the simpler one.

The Kohn-Sham approach is based on the assumption that the exact ground state density can be represented by the ground state of an auxiliary system of non-interacting particles where the auxiliary one-electron Hamiltonian was chosen to have the form:

$$\hat{H}_{aux} = -\frac{1}{2}\nabla^2 + V_{eff}(r) \tag{2.8}$$

Here we have the kinetic energy plus an effective local potential acting on an electron at the point r. Thus, the density of the auxiliary system and the independent particle kinetic energy are given in terms of the single particle orbitals:

$$\rho(r) = \sum_{i=1}^{N} |\Psi_i(r)|^2 \tag{2.9}$$

$$T_s = -\frac{1}{2}\sum_{i=1}^{N} \langle \Psi_i | \nabla^2 | \Psi_i \rangle = \frac{1}{2}\sum_{i=1}^{N} |\nabla \Psi_i|^2 \tag{2.10}$$

In the KS approach the ground state energy functional can be written in the following form:

$$E_{KS} = T_s[\rho] + E_{NN} + E_{Hartree}[\rho] + E_{xc}[\rho] + \int d^3 r V_{ext}(r)\rho(r) \tag{2.11}$$

The term $E_{Hartree}[\rho]$ is the interaction of the density $\rho(r)$ with itself, the term $V_{ext}(r)$ is the external potential due to the nuclei and any other external fields, and E_{NN} is the interaction between the nuclei. Here we introduce Hohenberg-Kohn functional, $F_{HK}[\rho]$, which includes all internal energies of the interacting electronic system, kinetic and potential:

$$F_{HK}[\rho] = T[\rho] + V_{int}[\rho] \tag{2.12}$$

where $T[\rho]$ is the kinetic energy and $V_{int}[\rho]$ is the interaction energy of electrons with density $\rho(r)$. The functional $F_{HK}[\rho]$ is universal because kinetic energy and interaction energy of the electrons are functionals only of the electronic density. Now we can write exchange correlation energy $E_{xc}[\rho]$ in terms of the Hohenberg-Kohn functional:

$$E_{xc}[\rho] = F_{HK}[\rho] - (T_s[n] + E_{Hartree}[\rho]) = \langle \hat{T} \rangle - T_s[\rho] + \langle \hat{V}_{int} \rangle - E_{Hartree}[\rho] \tag{2.13}$$

We can see that $E_{xc}[\rho]$ is nothing else then the difference between the kinetic energies of the interacting and non interacting systems, the electron-electron interactions and the Hartree energy.

One can view the solution of the auxiliary KS problem as a minimization with respect to the density $\rho(r)$ or the effective potential $V_{eft}(r)$ [7] and, using the Lagrange multiplier, one can derive Kohn-Sham Schrödinger-like equations:

$$(H_{KS} - \varepsilon_i)\Psi_i(r) = 0 \tag{2.14}$$

where ε_i are the eigenvalues, Ψ_i the functions and H_{KS} is the effective Hamiltonian defined in (2.8) with:

$$\hat{H}_{KS} = -\frac{1}{2}\nabla^2 + V_{KS}(r) \tag{2.15}$$

$$V_{KS} = V_{ext}(r) + V_{Hartree}(r) + V_{xc}(r) \tag{2.16}$$

The theory is exact so far and the problem of one equation for the many body wave function has been reduced to a system of N single particle equations in a effective potential V_{ef}.

2.2.3 Exchange correlation approximation

To write an actual expression for the exchange-correlation potential, which is a functional of the density, we need to make some approximations. There are many approximations

for the exchange correlation term but the most commonly used ones are the local density approximation (LDA) and the generalized gradient approximation (GGA).

The LDA approximation is based on the idea that the inhomogeneous electronic system can be considered as locally homogeneous. Basically the exchange correlation potential at point r which was depending of the value of the density at the point r and also of the density in the whole space, in the LDA approximation depends only on the value of the density at r while the variations are neglected. Therefore, the exchange correlation energy can be written as [7]:

$$E_{xc}^{LDA}[\rho(r)] = \int \rho(r)\varepsilon_{xc}[\rho(r)]dr, \tag{2.17}$$

where $\varepsilon_{xc}[\rho]$ is the exchange correlation energy density of a uniform electron gas of density $\rho(r)$.

LDA works well in most cases, despite the fact that the systems are usually inhomogeneous. However, it has some deficiencies, like overbinding of molecules and solids, and the fact that it favours homogeneous systems. Nonetheless, it gives good geometries and chemical trends.

GGA is basically an extension of the local density approximation where instead of neglecting all possible variations of density it uses a gradient $\nabla\rho(r)$ to modify the behaviour when its variation is important. In this case the exchange correlation energy is given by [7]:

$$E_{xc}^{GGA}[\rho(r)] = \int f(\rho(r), \nabla\rho(r))dr. \tag{2.18}$$

GGA functionals provide better binding energies than LDA but they overestimate the bonding distances.

2.2.4 The SIESTA method

In many simulation codes we can find other approximations besides the exchange correlation approximation, which make the calculations more practical. In this thesis, the SIESTA code was used, which is relying on some approximations that are going to be given in the following text.

Pseudopotentials

The chemical properties of materials are mostly dependent on the valence electrons, while core electrons have very little or no contribution at all. Therefore, we can separate the valence electrons from the core electrons which are basically screening the nuclear charge seen by the valence electrons. For that reason, in SIESTA we use pseudopotentials, which are an effective potential that valence electrons feel [18]. Actually, introduction of pseudopotentials in the calculations reduces the computational cost because the number of electrons needed to describe an atom is reduced.

Although there are different kinds of pseudo potentials, we were working only with Troullier and Martins ones [19] in its non local form [20]. In all-electron KS calculation the pseudopotentials are generated for each atomic species and the all-electron wavefunctions are calculated for all the electron states. Then, the pseudo-wavefunctions are created by fitting functions to the all-electron wavefunctions following the criteria [7]:

- All electron and pseudo-valence wavefunctions agree beyond a chosen core radius r_c.
- All electron and pseudo valence eigenvalues agree for the chosen atomic reference configuration.
- The pseudo-wavefunctions will be nodeless (smooth) inside the core radius.
- The norm of the pseudo-wavefunctions is the same as the true wavefunctions: norm conserving pseudopotentials.

The pseudopotentials can be expressed into two fully separable parts: a local part and a non local part

1. a local part $V_I^{(local)}(r)$, where the pseudopotential depends on (r): this term is long ranged and behaves asymptotically as the electrostatic field generated by the total core plus nucleus charge (valence ion charge) as Z_V/r for $r \to \infty$.
2. a non local part V_I^{nl}: this is a separated pseudopotential for each angular momentum l and is created following the method of Kleinman [20]

There are many ways to generate a pseudopotentials and in all of them the user has to choose between the accuracy and transferability that lead to small cutoff radii or smoothness of the wavefunctions that require larger r_c cutoffs. Therefore, the Kohn-Sham Hamiltonian in equation (2.14) is modified by replacing the electron-nucleus Coulomb terms with:

$$V_I = V_I^{(local)}(r) + \hat{V}_I^{nl} \tag{2.19}$$

The KS Hamiltonian will now been given in the expression:

$$H = T + \sum_I [V_I^{(local)}(r) + \hat{V}_I^{nl} + V_H(r) + V_{xc}(r)] \tag{2.20}$$

Localized basis sets

In the SIESTA calculations we use the pseudo-atomic orbitals as basis sets to describe the Kohn-Sham orbitals:

$$\Psi_i(r) = \sum_\mu c_{i\mu} \xi_\mu(r) \tag{2.21}$$

Here, the coefficients $c_{i\mu}$ have to be determined and the $\xi_\mu(r)$ are the basis functions. Different functions in the basis set are denoted with the index μ.

The SIESTA code uses the numerical atomic orbitals which represent the product of numerical radial function and a spherical harmonic:

$$\xi_{nlm}(r) = R_{nl}(r) \times Y_{lm}(r) \tag{2.22}$$

where n is the principal quantum number that describes different functions with the same angular momentum l, and m is the azimuthal quantum number. The basis set describes only valence states because we use pseudopotentials to describe the core electrons. We say that numerical atomic orbitals are strictly localized because they are strictly zero beyond a given radius from the nucleus. Several radial functions with the different radial shape can be included in one basis set to improve accuracy.

The basis set has to be carefully chosen to be both accurate and practical. For the description of the Kohn-Sham orbitals one has to use the minimum possible number of orbitals which give sufficiently good results. The choice of the minimal number of functions in the basis will actually represent the primary valence degrees of freedom. Therefore, the minimum set to describe an hydrogen atom will be one s function ($1s$) and this is called single-ζ basis. To improve the minimum set we double the basis functions using more then one radial function per angular momentum (l). This is how we get double-ζ, triple-ζ and so on. In the case of the hydrogen atom, double-ζ means having two $1s$ orbitals with different radial shape. Further on, we can add "polarisation functions" taking into account the environment of the molecule or solid. In this thesis we used single-ζ and double-ζ polarized

basis sets, SZP and DZP respectively. In the case of hydrogen atom, DZP would mean having two orbitals of s symmetry with different radial dependence and a shell of $2p$ orbitals in the basis. There are several ways to choose the radial shape for the two orbitals in the same shell. For the multiple-ζ bases in SIESTA, the first-ζ is generated by solving the radial Schrödinger equation for an atom restricted with a potential of the form [21]:

$$V(r) = V_0 \frac{e^{\frac{r_c - r_i}{r - r_i}}}{r_c - r_i} \tag{2.23}$$

Here V_0 is a parameter that determines the shape of the confining potential, r_c is the cutoff radius of the orbitals and r_i the internal radius where the potential starts. The formation of the first-ζ is generated differently then second-ζ, triple-ζ and so on. To generate the second-ζ we chose the "split valence" scheme adapted to numerical orbitals and implemented in the SIESTA code [13]. In this method the second-ζ orbital has the same tail as the corresponding first-ζ orbital but change to a simple polynomial behaviour inside a certain "split radius" r_l^s:

$$\begin{aligned} \xi_l^{2\zeta}(r) &= r^l(a_l - b_l r^2) && \text{if} \quad r < r_l^s \\ &&& \text{or} \\ \xi_l^{2\zeta}(r) &= \xi_l^{1\zeta}(r) && \text{if} \quad r \geq r_l^s \end{aligned} \tag{2.24}$$

where a_l and b_l are determined by imposing the continuity and slope at r_l^s. Using the "split valence" scheme and following the procedure in equation (2.24), the second-ζ is then defined as $\xi_l^{2\zeta} - \xi_l^{1\zeta}$, which is zero beyond the split radius r_l^s.

2.3 Tight binding approximation

The tight binding method was developed by Bloch in 1928 which was one of the first theories of electrons in a crystal [22]. In the first formulation of this theory, Bloch considered only the simplest s-orbitals in the basis [23], while few years later, Jones, Mott and Skinner introduced different atomic orbitals [24].

The tight binding approximation is often used for large calculations as a method that efficiently solves the one electron Schrödinger equation. The tight binding model is based

on linear combination of atomic orbitals (LCAO). In calculations of electronic properties of condensed matter we usually deal with crystals which are periodic systems of atoms. Therefore, we can derive the Bloch theorem for the eigenstates by defining the basis of Bloch orbitals with the wavevector k:

$$\xi_{\mu k}(r) = A_{\mu k} \sum_{R_j} e^{ikR_j} \xi_{\mu}(r - R_j) \tag{2.25}$$

where $A_{\mu k}$ is a normalization factor and $\xi_{\mu}(r - R_j)$ are orbitals centred on atom j. Now this basis can be used to write an eigenfunction of the Schrödinger equation as:

$$\Psi_{ik}(r) = \sum_{i\mu} C_i(k) \xi_{\mu k}(r) \tag{2.26}$$

and when we introduce the wavevector k in the secular equation $H\Psi = E\Psi$ we get:

$$H_{\mu\nu}(k) C_{i\mu}(k) = E_{i\nu}(k) S_{\mu\nu}(k) C_{i\nu}(k) \tag{2.27}$$

Here, the Hamiltonian $H_{\mu\nu}(k)$ and the overlap matrix $S_{\mu\nu}(k)$ are defined as:

$$H_{\mu\nu}(k) = \langle \xi_{\mu k} | H | \xi_{\nu k} \rangle \tag{2.28}$$

$$S_{\mu\nu}(k) = \langle \xi_{\mu k} \xi_{\nu k} \rangle \tag{2.29}$$

These two expressions can be written in their integral forms as:

$$H_{\mu\nu}(k) = \sum_{R} e^{ikR} \int dr \xi^*(r) H \xi(r - R) \tag{2.30}$$

$$S_{\mu\nu}(k) = \sum_{R} e^{ikR} \int dr \xi^*(r) \xi(r - R) \tag{2.31}$$

The Hamiltonian matrix elements in (2.45) consist of kinetic part and potential part:

$$\hat{H}_e = \hat{T}_e + \hat{V}_{eff} \tag{2.32}$$

where the first term is the usual kinetic energy and the second term is the effective potential which represents all the possible interactions in the solid. If we assume that $\hat{V}_{eff}$ is a sum of the atomic potentials generated by all the atoms in the solid:

$$\hat{V}_{eff} = \sum_j v(r - R_j) \tag{2.33}$$

and introduce this potential into the equation (2.45) we would find that we have four main kinds of matrix elements:

- One-center, where both orbitals and the potential are centered on the same atom:

$$\int dr \xi^*(r - R_j) v(r - R_j) \xi(r - R_j) \tag{2.34}$$

- Two-center, where the orbitals are centered on different atoms and the potential is on one of the two:

$$\int dr \xi^*(r - R_i) v(r - R_j) \xi(r - R_j) \tag{2.35}$$

- Two-center, with both orbitals on the same atom and the potential centered on another:

$$\int dr \xi^*(r - R_j) v(r - R_i) \xi(r - R_j) \tag{2.36}$$

- Three-center, where the orbitals and the potential are all centered on different atoms.

$$\int dr \xi^*(r - R_i) v(r - R_j) \xi(r - R_k) \tag{2.37}$$

The calculation of matrix elements of the Hamiltonian that involves the multi-center integrals can be computationally very costly. Slater and Koster proposed that all the matrix

elements should be approximated with the two-center form and fitted to theoretical calculations (or experimental data) [23]. By this approach all matrix elements have the same symmetry as for two atoms in free space, which is a great simplification and useful approach in understanding of electrons in materials. The basis set is assumed to be orthogonal and is introduced in most practical tight-binding approaches as well as in our work with TB in rubrene.

2.4 Phonons and electron-phonon coupling

The theoretical method used for calculations of phonons and electron-phonon coupling in the rubrene crystal is going to be presented here.

For the calculation of the vibrational properties we build the force-constant matrix by displacing individual atoms along the Cartesian directions. The dynamical matrix is defined from the second derivative of total energy:

$$D_{i\alpha,j\beta} \equiv \frac{1}{\sqrt{m_i}\sqrt{m_j}} \frac{\delta^2 E}{\delta u_{i\alpha} \delta u_{j\beta}} \tag{2.38}$$

where i and j are the atoms, m_i and m_j their masses and $u_{i\alpha}$ and $u_{j\beta}$ are the displacements of these atoms along the Cartesian coordinates α and β, respectively. The force on atom i upon displacement $u_{i\alpha}$ is given with the equation:

$$F_{i\alpha} = -\frac{\partial E}{\partial u_{i\alpha}} \tag{2.39}$$

We take the finite differences by approximation so that the Dynamical matrix is calculated from positive and negative displacements of the atom as:

$$D_{i\alpha,j\beta} \approx \frac{\Delta F_{i\alpha}}{\Delta u_{j\beta}} \tag{2.40}$$

From the solution of the eigenvalue equation of the dynamical matrix:

$$\sum_{j\beta} D_{i\alpha,j\beta} e_{j\beta} = \omega^2 e_{i\alpha} \tag{2.41}$$

we get the eigenvectors e^p (p is the index of the mode) with the Cartesian components $e_{i\alpha}$ for atom i and phonon frequencies, ω_p. The phonon normal modes σ^p are calculated as:

$$\sigma^p_{i\alpha} = \frac{1}{\sqrt{m_i}} e^p_{i\alpha} \tag{2.42}$$

In this direct diagonalization of Dynamical matrix we could calculate vibrational properties of the crystal, such as eigenvectors of phonons e^p and their frequencies, ω_p. In order to obtain the phonon frequencies to a sufficient level of accuracy, we had to involve an alternative method for their calculation which is called a *frozen-phonons method*. In this procedure, we displace all atoms of the crystal in the direction of the mode vectors σ^p of the given phonon mode p according to:

$$\vec{u}_p = \vec{u}^0 + \lambda \vec{\sigma}_p \tag{2.43}$$

where $\vec{u}^0$ is starting position of the atom and λ is the amplitude of the phonon p. Further on, we re-calculate the total energies of the crystal with the frozen phonon and perform these calculations for every normal mode for a set of different amplitudes λ. Finally, from our results we could observe the change in total energy $E \longrightarrow E + \Delta E(\lambda)$ which is given with the equation:

$$\Delta E(\lambda) = \frac{1}{2} \sum_{i\alpha, j\beta} \lambda e^p_{i\alpha} D_{i\alpha, j\beta} \lambda e^p_{j\beta} = \frac{1}{2} \omega_p^2 \lambda^2 \tag{2.44}$$

As it will be shown later, this allows the computation of phonon frequencies with better accuracy, especially for the low-energy modes for which the problem of imaginary frequencies is avoided.

For the calculation of electron-phonon coupling in rubrene crystal we use the Holstein-Peierls Hamiltonian $H = H_{el} + H_{ph} + H_{el-ph}$ which consists of an electronic part, a phononic part and a coupling part between electrons and phonons and is given in a form:

$$H = \sum_{M,N} \varepsilon_{MN} a_M^\dagger a_N + \sum_{Q=(q,p)} \hbar\omega_Q (b_Q^\dagger b_Q + \frac{1}{2}) + \sum_{Q,M,N} \hbar\omega_Q g_{MN}^Q (b_{-Q} + b_Q^\dagger) a_M^\dagger a_N \tag{2.45}$$

where ε_{MN} are the matrix elements of the electronic coupling between states M and N and $a_M(a_M^\dagger)$ and $b_Q(b_Q^\dagger)$ are the annihilation (creation) operators for electrons and phonons respectively. Q is the coordinate of the phonon $Q = (q, p)$ where p is index of the normal mode and q is the phonon wavevector. This model stands for both intra-molecular and inter-molecular electron-phonon interactions.

The electronic part of the Hamiltonian, H_{el}, and the phononic part, H_{ph}, can be directly computed with Density Functional Theory. For the calculation of electron-phonon coupling in rubrene we have chosen the frozen-phonons method. The electron-phonon coupling constants g_{MN}^Q in the model are defined as the linear changes of the electronic matrix elements ε_{MN} with the amplitudes λ of the phonon normal mode p with wave vector q and are calculated as:

$$g^p = \frac{\partial E}{\partial \lambda^p} \frac{1}{\sqrt{2\omega_p^3 \hbar}} \tag{2.46}$$

Defined in this way, the coupling constants are dimensionless and explicitly depend on the phonon wave vector q.

To calculate the electron-phonon coupling constants of each mode in the finite differences approach, we followed the changes of energies in the electronic band structure when each mode σ^p is applied on the rubrene crystal. The changes in the band structure for different amplitudes λ would enable the extraction of the electron-phonon coupling constants from the linear slope of the changes in the electronic energies [25, 26].

In this thesis we are also going to present results of the tight binding calculations of electron-phonon coupling in rubrene. Therefore, here we will briefly explain the tight binding model used for these calculations of the rubrene crystal.

Beyond the numerical calculation of electronic energy bands and vibrational properties, we derive a tight-binding model to parametrize electronic properties and electron-phonon coupling interactions in rubrene. Thereby, we focus on the states derived from the highest

occupied molecular orbitals (HOMO) of rubrene, i.e. the up most valence band in the crystal. We look for a simple TB model in which only one state per molecule is included, the HOMO orbital. The basis set in our TB approach is made only of HOMO orbitals which are orthogonal as in usual TB models. In order to obtain TB parameters from DFT calculations we need to employ a basis transformation from the atomic orbital basis used in the SIESTA calculations into the basis set made of HOMO orbitals. Therefore, we start from the basis of atomic orbitals for which the Kohn-Sham Hamiltonian, $\hat{H}$, is described as:

$$H_{\mu\nu} = \langle \xi_\mu | \hat{H} | \xi_\nu \rangle \tag{2.47}$$

and the overlap matrix as:

$$S_{\mu\nu} = \langle \xi_\mu | \xi_\nu \rangle. \tag{2.48}$$

Here ξ_μ and ξ_ν are representing atomic orbitals of the atoms μ and ν. The transition from the basis set used in density functional theory calculations and the desired orthogonal tight binding model can be achieved in two steps. First we project onto the molecular HOMO orbitals $|\Psi_M^{HOMO}\rangle$ known from gas-phase calculations:

$$|\Psi_M^{HOMO}\rangle = \sum_\mu c_{\mu M} |\xi_\mu^M\rangle \tag{2.49}$$

where M indicates the molecule on which the HOMO orbital is located, $|\xi_\mu^M\rangle$ are the basis functions associated to M and $c_{\mu M}$ are the coefficients which can be obtained from the SIESTA calculations of single molecules. In this way we can express the Hamiltonian of two molecules M and N in the non-orthogonal HOMO basis while neglecting other types of molecular orbitals as:

$$\begin{aligned} H_{MN} &= \langle \Psi_M | \hat{H} | \Psi_N \rangle \\ &= \sum_{\mu\nu} c_{\mu M}^* c_{\nu N} \langle \xi_\mu^M | \hat{H} | \xi_\nu^N \rangle \end{aligned} \tag{2.50}$$

and

$$S_{MN} = \langle \Psi_M | \Psi_N \rangle = \sum_{\mu\nu} c^*_{\mu M} c_{\nu N} \langle \xi^M_\mu | \xi^N_\nu \rangle \tag{2.51}$$

is the molecular overlap matrix of the molecules M and N. The other molecular states are neglected as we are interested only in the parameters of the HOMO orbitals of rubrene molecules.

The second step in the tight binding approach was the orthogonalization of the molecular orbitals for which we have chosen the Löwdin orthogonalization method with the overlap matrix represented with the equation (2.51). In this method, from the given initial set of normalized but non-orthogonal wave functions, $|\Psi_M\rangle$, we generate a new set of orbitals $|\Psi'_M\rangle$ defined as:

$$|\Psi'_M\rangle = |\Psi_M\rangle - \frac{1}{2}\sum_N S_{MN} |\Psi_N\rangle \tag{2.52}$$

This single step mixing is repeated until the wave functions are orthogonal to the desired degree of accuracy. For the HOMO orbitals of rubrene it turns out that a single step of orthogonalization is sufficient as the overlap matrices are negligibly small after the first iteration. If we apply this orthogonalization for undisplaced atoms of the rubrene crystal we can calculate the electronic part of the Hamiltonian (2.45) H_{el}. Applying this approach for the crystal structures with the frozen-phonon distortions, we can obtain the Holstein and Peierls electron-phonon coupling constants, which are now going to be the coupling constants in the orthogonal molecular HOMO basis, g^Q_{MN}. The local Holstein coupling constants are defined for the case when $q = 0$ and can be calculated as:

$$g^p_{Holstein} = \frac{1}{\sqrt{2\hbar\omega^3_p}} \left(\frac{\partial \varepsilon_0}{\partial \lambda}\right) \tag{2.53}$$

They are averaged over the four molecules in the unit cell. The Peierls coupling constants:

$$g^p_{Peierls} = \frac{1}{\sqrt{2\hbar\omega^3_p}} \left(\frac{\partial \varepsilon_i}{\partial \lambda}\right) \tag{2.54}$$

are defined by the transfer integrals ε_i between HOMO states of the neighbouring molecules.

2.5 Charge Density Waves and Lindhard response functions

A Charge Density Wave (CDW) represents a state with spontaneously broken translational symmetry, which is specific to anisotropic low dimensional materials. The phase transition to the CDW state is accompanied by the development of periodic lattice distortions and often, to the opening of energy gaps at the Fermi level [27, 28].

In the 1930's Peierls gave a prediction of CDW showing that a one-dimensional material would be unstable to the formation of energy gaps on the positions $\pm k_F$ at the Fermi level. Later on, in the 1950's Fröhlich explained that the opening of the gap at the Fermi level happens as a consequence of interactions of electrons with phonons which have the wavevector $\vec{q} = 2k_F$ [29]. In the 1960's Little suggested that some organic materials with high polarizability could exhibit superconductivity at considerably high critical temperature. This suggestion launched a large activity and molecular organic metals were soon prepared. However, instead of superconducting transitions, these compounds were showing Peierls transitions. The first evidence for CDW transport in inorganic linear chain compounds was first reported in 1976 by Monceau et al. [30], who observed anomalous electric behaviour in $NbSe_3$.

The question one could ask is how are charge density waves connected with one-dimensionality? One dimensional materials have sections of Fermi surface which are parallel to each other and provide an optimal condition for nesting. When a piece of Fermi surface can be translated by wavevector $\vec{q}$ and superimposed on another piece of Fermi surface, then the Fermi surface is said to be nested by a wavevector $\vec{q}$, Figure 2.1 [31].

When the Fermi surface is nested then the system shows electronic instability and usually undergoes a charge density wave transition. The CDW is a periodic modulation of charge density followed by distortion of crystal lattice. Sometimes it is more energetically convenient for charge carriers to take this configuration and atoms just follow the new periodic potential, Figure 2.2. The temperature at which CDW transition happens is called transition temperature or Peierls temperature, T_p, and the transition is called a Peierls transition.

Figure 2.2a shows the one electron band structure of the unperturbated 1D system. Here, the charge density, ρ, and the atomic distances, a, are uniform throughout the crystal. Under

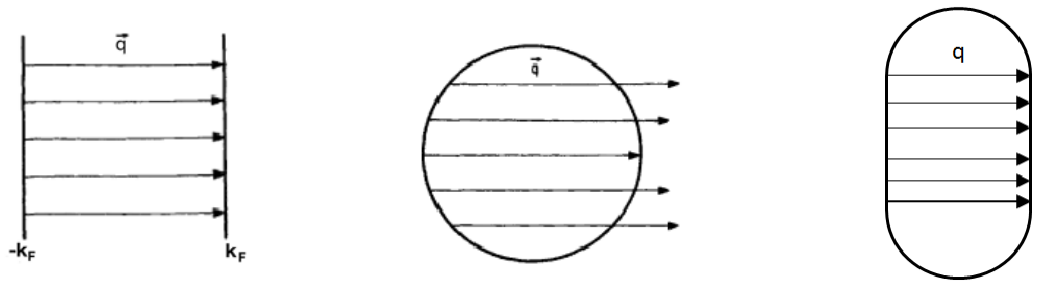

(a) (b) (c)

Fig. 2.1 Fermi surface nesting: (a) 1D Fermi surface - possible nesting, (b) 2D Fermi surface - no nesting, (c) quasi-2D Fermi surface with partial nesting.

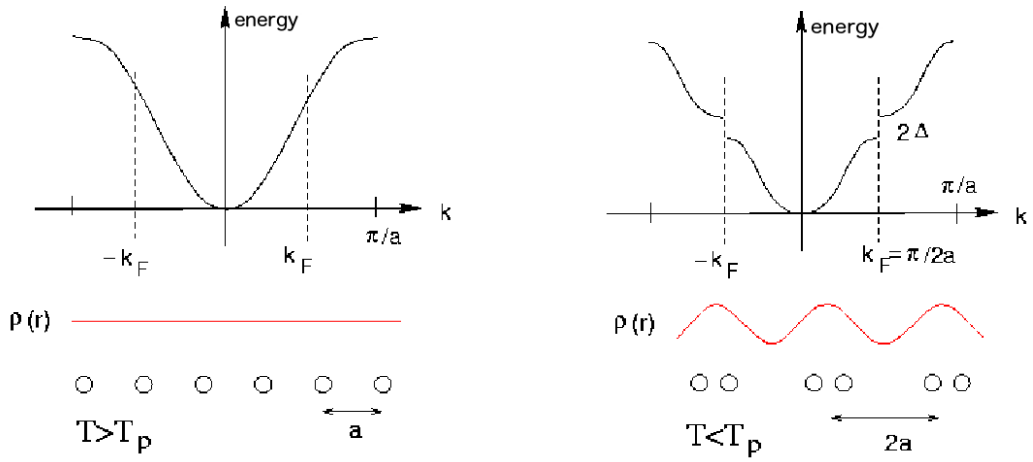

(a) (b)

Fig. 2.2 Charge density wave instability and opening of the gap at the Fermi level.

some perturbation, lowering the temperature below the transition temperature, T_p, the system undergoes a CDW transition and the gap opens on the Fermi surface at the positions $\pm k_F$, Figure 2.2b. The electron bands just below the Fermi level combine in such a way that electrons are having lower energies than before the perturbation and energy bands above the Fermi level are moving towards higher energies. In this way the band gap opens which is followed with distortion of the crystal lattice [32].

Without specifying the perturbation, let us assume that some external potential $\phi^{ext}(\vec{r})$ leads to a density fluctuation, $\rho^{ind}(\vec{r})$, and therefore to a potential $\phi^{ind}(\vec{r})$ induced by $\rho^{ind}(\vec{r})$:

$$\phi^{ext}(\vec{r}) \Longrightarrow \rho^{ind}(\vec{r}) \Longrightarrow \phi^{ind}(\vec{r})$$

The Fermi surface nesting is inducing electronic instability and hence a phase transition to the charge density wave (CDW) state. The electron charge redistribution is induced by the perturbed electric potentials. The response of the electron gas to the time independent potential, $\phi^{ind}(\vec{r})$, and the rearrangement of the electronic charge, $\rho^{ind}(\vec{r})$ are described with these equations [6]:

$$\phi^{ind}(\vec{r}) = \int_q \phi^{ind}(\vec{q}) e^{i\vec{q}\cdot\vec{r}} d\vec{q} \qquad \rho^{ind}(\vec{r}) = \int_q \rho(\vec{q})^{ind} e^{i\vec{q}\cdot\vec{r}} d\vec{q}$$

If the potential is given as:

$$\phi(\vec{q}) = \phi^{ext}(\vec{q}) + \phi^{ind}(\vec{q})$$

the induced charge density can be expressed as:

$$\rho^{ind}(\vec{q}) = \chi(\vec{q})\phi(\vec{q}) \tag{2.55}$$

$\chi(\vec{q})$ is the so-called Lindhard response function and it is defined by equation:

$$\chi(\vec{q}) = -\frac{1}{(2\pi)^d} \int_{1BZ} d\vec{k} \frac{f(\vec{k}+\vec{q}) - f(\vec{k})}{E_{\vec{k}+\vec{q}} - E_{\vec{k}}} \tag{2.56}$$

Here d is the dimensionality, $f(\vec{k})$ represents the Fermi function and $E_{\vec{k}}$ denotes the free electron energy at the momentum $\vec{k}$ (the Fermi function has values $f(\vec{k}) = 1$ for electrons and $f(\vec{k}) = 0$ for holes at $T = 0$ K).

On the figure 2.3 is shown a Lindhard function for one-, two- and three-dimensional electron gas at $T = 0$ K as a function of the wavevector. One can see that for one-dimensional case, at the position of $2k_F$ a divergence is expected, which would be the origin of charge density wave.

In the definition of Lindhard susceptibility, equation (2.56), the Fermi function $f(\vec{k})$ indicates that only electron-hole pairs at $\vec{k}$ and $\vec{k}+\vec{q}$ contribute to the development of CDW

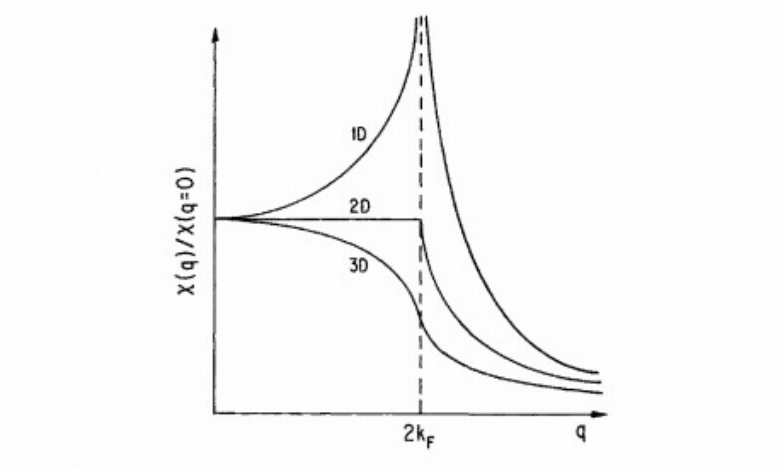

Fig. 2.3 Lindhard response function as a function of wavevector for one-, two- and three-dimensional free electron gas at zero temperature, [6].

states, since $f(\vec{k}+\vec{q}) - f(\vec{k}) \neq 0$ only for $(f(\vec{k}+\vec{q}), f(\vec{k})) = (1,0)$ and $(0,1)$. The peak structure of $\chi(\vec{q})$ is associated with the selected $\vec{q}$ vectors that give the smallest denominator $E_{\vec{k}+\vec{q}} - E_{\vec{k}} \approx 0$ or $E_{\vec{k}+\vec{q}} \approx E_{\vec{k}}$ over large regions in $\vec{k}$ space available for integration. The electron-hole pairs nested by such a wavevector $\vec{q}$ have a relatively high density of states at the Fermi level and CDW phase transition is dominated by the energy of states which are close to the Fermi level, E_f. Thus, the $\chi(\vec{q})$ peak structure strongly depends of the Fermi surface topology. Low dimensional materials have more regions of Fermi surface parallel to each other, which give more density of states available for nesting, and are more strongly susceptible to the electron energy instability and CDW phase transition. This often allows a simple graphical interpretation of Fermi surface nesting as the origin of the CDW. Thus, the CDW instability is driven by the electronic structure and the Fermi surface topology. Indeed, Fermi surface nesting has provided a powerful tool to understand various examples of the CDW states observed in many low dimensional materials.

For 1D, at finite temperatures, the numerator in the equation (2.56) is given by:

$$\frac{1}{exp(-E_k/k_BT)+1} - \frac{1}{exp(E_k/k_BT)+1} = tanh\frac{E_k}{2k_BT} \tag{2.57}$$

where E_k is now measured from the Fermi level, E_f. Therefore, the equation (2.56) becomes:

$$\chi(q=2k_f,T) = -e^2 n(E_f) \int_0^{E_0/2k_BT} \frac{tanh\, x}{x} dx \tag{2.58}$$

E_0 is an arbitrarily chosen cutoff energy which is usually taken to be equal to the Fermi energy, E_f. The integral can be evaluated giving:

$$\chi(2k_fT) = -e^2 n(E_f) ln \frac{1.14E_0}{k_BT} \tag{2.59}$$

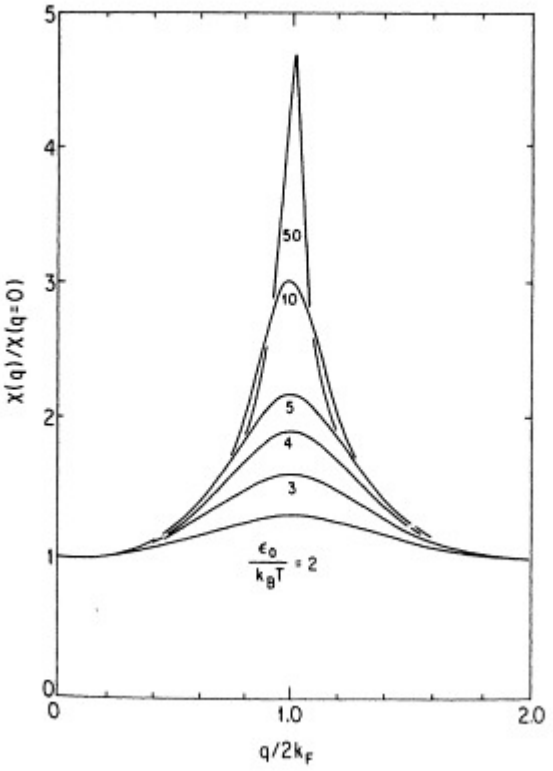

Fig. 2.4 Lindhard function of one-dimensional free electron gas at various temperatures, [6].

We have studied the Lindhard function for several well-known low-dimensional materials in order to analyze if the structural modulations that they exhibit originate from some Fermi surface instability. In all cases, in contrast to the previous methodological approach, we have carried out the study taking into account the real structure of the systems by using first-principles density functional theory calculations. It is important to emphasize that large sets of k points are needed in these very anisotropic materials in order to have accurate Lindhard functions.

Chapter 3

Electron-phonon coupling in rubrene

3.1 Introduction

The scientific interest in organic semiconductors is constantly growing driven by many technological applications. These organic materials are particularly interesting from the processing point of view (e.g. low temperature, solution processable, chemical modifications, etc.) [33–37]. Efficient charge transport in organic semiconductors is the main reason for their application in the organic electronics [1–3, 38–41] and there is a huge effort in improving the carrier mobilities by means of available tools such as chemical and structural modifications of these organic materials. Thereby, theoretical input can provide guidelines towards possible realizations of high mobility of charge carriers and production of highly functional materials [42]. Nonetheless, theoretical interpretation and understanding of several properties of these materials sometimes remains incomplete. Charge transport in some organic semiconductors often displays very different behaviour compared to the conventional inorganic semiconductors.

One of the prototypical materials studied frequently is rubrene (5,6,11,12- tetraphenyltetracene), a red coloured polycyclic aromatic hydrocarbon [43–48]. Rubrene, as many other organic semiconductors, found applications in organic light emitting diodes (OLEDs) and organic field effect transistors (OFETs) [49–55]. At first it was expected from rubrene to have small carrier mobilities due to the weak intermolecular interactions and bulky phenyl rings attached to the side of the tetracene backbone, Figure 3.1. However, most interestingly, rubrene holds the distinction of being the organic semiconductor with the highest carrier mobility, which can reach $40 cm^2/Vs$ for holes [56]. Therefore, rubrene is often used as a model compound for experiments [56–63] and simulations [43, 45, 64–66]. The most recent advances for rubrene research include novel kind of growth by means of van der Waals epitaxy [67] or the detailed analysis of defect formation.[68].

Theoretically, rubrene has been characterized by means of semiempirical methods and methods that have been carried beyond the rigid molecule approximation [43, 69]. However, to date a full analysis of the electronic properties and electron-phonon coupling (including Holstein and Peierls type of couplings) has not been shown. This might be due to the structure of rubrene, which exhibits a relatively large unit cell with 280 atoms and results in 840 phonon modes, Figure 3.2, or to the difficulties in density functional theory (DFT) based methods with accuracy to describe the low frequency modes.

Fig. 3.1 The molecule of rubrene consisting of the central tetracene backbone and four attached phenyl groups.

We performed density functional theory (DFT) calculations of phonon modes, phonon frequencies, electron-phonon coupling and the calculation of the distorted structure of rubrene crystal. The theoretical and computational methods used for these calculations in rubrene are given in the Chapter 2. Here we are also going to show our results of the tight binding (TB) calculations of rubrene and a practical way to remove the problem of inaccuracies with the low frequency modes that often occur in the DFT-based methods and are problematic for the systems with a large number of atoms.

3.2 Vibrational properties of rubrene

The molecule of rubrene $C_{42}O_{28}$ is made of tetracene backbone with four phenyl groups attached on each side of the backbone, Figure 3.1. The phenyl groups are rotated out of the molecular plane due to the steric hindrance between the phenyls. The crystallization of rubrene can result in different structures. Depending on the growth conditions, crystals of rubrene can be monoclinic, triclinic and orthorhombic. In our calculations we were using a non-primitive orthorhombic unit cell made of four molecules of rubrene: two molecules exchanged with rototranslation and two more molecules obtained by a non-primitive translation, Figure 3.2 [70]. We start from the experimental coordinates [58], and

perform a conjugate gradient optimization to obtain relaxed atomic coordinates and lattice constants of the crystal. For this relaxed unit cell, we calculate electronic properties, phonon modes and frequencies as well as electron-phonon coupling parameters.

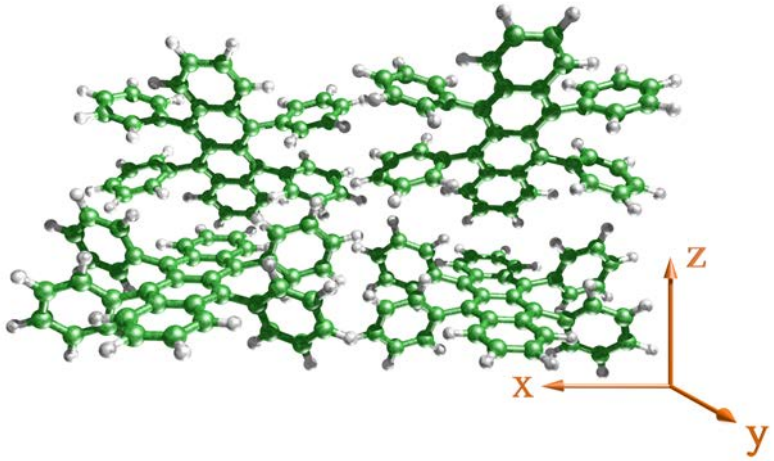

Fig. 3.2 Perspective view of the rubrene unit cell with four molecules.

All calculations were done with the SIESTA code [10, 13] using the local density approximation (LDA) [71, 72]. We used double-ζ polarized basis set of numerical orbitals optimised for the bulk structure of rubrene [21]. The basis set parameters for H and C are given in the Table 3.1. The pseudopotentials used for calculations of rubrene crystal are the Troullier-Martins type [19] in their nonlocal form [20].

	r_c(Bohr)					V_0(Ry)			r_i(Bohr)			Q(e)
	$s_{1\zeta}$	$s_{2\zeta}$	p	$d_{1\zeta}$	$d_{2\zeta}$	s	p	d	s	p	d	
H	7.50	1.85	4.75	–	–	45.4	40.1	–	4.20	2.96	–	0.76857
C	6.50	2.86	8.50	2.95	3.70	39.4	95.7	62.5	3.61	4.31	0.66	0.074

Table 3.1 Parameters that define the basis for H and C: r_c is the cutoff radius of each of the orbitals, V_0 and r_i are the parameters which determine the confining potential for each shell and Q is a charge assigned to the atom in the solution of the free atom problem.

After the diagonalization of the dynamical matrix (see Chapter 2 section 2.4) we obtain frequencies, ω_p, and eigenvectors, $e_{i\alpha}$, of all normal modes, which in the case of our unit cell made of four molecules or 280 atoms results in 840 normal modes. After careful analysis of calculated modes it turns out that some phonons have unrealistically small or even imaginary frequencies. This is a general problem which may seriously jeopardise further calculations

of electron-phonon coupling constants in rubrene as for these calculations we will be using phonon frequencies.

The origin of this behaviour lies in the general difficulty to describe collective crystal vibrations in soft materials like organic crystals. This inaccuracy and the appearance of the imaginary frequencies are one of the major problems when DFT methods are used in the systems with the large number of atoms, such as rubrene. Collective molecular modes, such as libration modes or translations, involve the motion of many atoms. This means that many force constants will enter in the resulting vibrational frequency. This is in contrast to e.g. a *C-H*-stretch mode, where the force constant related to the *C-H* bond will mostly define the frequency of the mode. Considering that forces $\Delta F_{i\alpha}$ for displaced atom i (equation (2.39) in Chapter 2) may have some small numerical error, this error can accumulate in the phonon frequency ω^p which results from all forces. Therefore, if the frequency of the mode is low, the relative error can then be very large for such modes.

However, detailed inspection of all low-frequency modes shows that vibrational patterns are correct and orthogonal which leads us to the conclusion that phonon vectors σ^p are correct in contrast to the vibration frequencies. Therefore, we need to re-calculate the mode frequencies and we do that by applying the frozen-phonon method explained in the Chapter 2. We re-calculate the changes in the total energy ΔE around the equilibrium configuration for different normal mode amplitudes λ for all vibrations using the equation:

$$\Delta E(\lambda) = \frac{1}{2} \sum_{i\alpha, j\beta} \lambda e^p_{i\alpha} D_{i\alpha, j\beta} \lambda e^p_{j\beta} = \frac{1}{2} \omega_p^2 \lambda^2$$

A list of some selected low-frequency modes with frequencies $\omega_I < 50 cm^{-1}$ is given in the Table 3.2. Here we denote the phonon frequencies obtained from the direct diagonalization of the dynamical matrix as ω_I and the re-calculated phonon frequencies using the frozen-phonons approach as ω_{II}. The Table 3.2 shows how the frequencies of the low-frequency modes can be strongly corrected by the frozen-phonon method.

On the Figure 3.3a is shown an example to illustrate the difference between the frequency calculated in direct diagonalization (ω_I) and the re-calculated one with frozen-phonons method (ω_{II}) for a chosen mode. The frequency obtained from the direct diagonalization of $D_{i\alpha j\beta}$ is $\hbar\omega_I = 5.5$ meV ($44.4 cm^{-1}$), while the quadratic fit to the total energy in the frozen-phonon method yields the corrected mode energy $\hbar\omega_I = 7.4$ meV ($59.6 cm^{-1}$). This is a typical example of the general behaviour of the low-frequency modes because the new value is increased by 34.5% compared to the original frequency of this mode. In the Figure 3.3b are shown relative frequency differences:

ω_I (cm^{-1})	ω_{II} (cm^{-1})	symm.	mode descr.
-19.9	17.0	B_{2g}	$R_{\parallel\ tetracene}$
0.06	16.4	B_{2u}	$T_y + B_{molecule}$
0.08	21.8	B_{1g}	$R_{\perp\ tetracene}$
5.5	20.8	B_{1u}	$T_z + B_{phenyl}$
9.4	31.7	B_{1u}	$B_{molecule}$
16.1	24.0	A_u	$T_x + tor_{phenyl}$
18.9	41.6	B_{3u}	$T_x + tor_{phenyl}$
21.4	41.6	B_{2g}	$R_{\perp\ tetracene} + tor_{phenyl}$
22.2	46.8	B_{2u}	$B_{molecule}$
29.5	43.5	B_{1g}	$R_{\perp\ tetracene}$
30.1	37.7	A_u	$T_x + W_{phenyl}$
38.1	52.2	B_{2u}	$B_{molecule}$
38.9	46.4	B_{1g}	$R_{\perp\ tetracene} + W_{phenyl}$
42.7	47.7	B_{1g}	$R_{\parallel\ tetracene}$
44.4	59.6	A_g	tor_{phenyl}
46.9	57.8	A_g	tor_{phenyl}
47.4	60.3	B_{3u}	tor_{phenyl}
48.3	55.5	B_{2g}	$R_{\parallel\ tetracene}$
48.5	49.0	B_{1u}	T_y
48.6	55.0	B_{1u}	$T_y + B_{molecule}$

Table 3.2 Phonon frequencies in both approaches with symmetry assignement and mode description with abbreviations: (T_{axis})-translation, (R_{axis})-rotation, (B)-butterfly mode, tor-torsion and W-wagging

$$\Delta\omega_{rel} = \frac{\omega_{II} - \omega_I}{\omega_{II}}$$

Evidently, with the new re-calculated frequencies we obtain higher energies especially for the low-frequency modes which are corrected by up to 50% and even more. On the other hand, higher frequencies are only slightly changed which indicated that only collective modes are affected and the frequencies for the high frequency modes are described well by the initial diagonalization of the dynamical matrix. For the further calculations we will only use the corrected frequencies, ω_{II}. With this method for phonon frequencies re-calculation we achieve the higher accuracy for all the phonon frequencies but most importantly, higher accuracy for the soft modes or low frequency modes and disappearance of the imaginary frequencies.

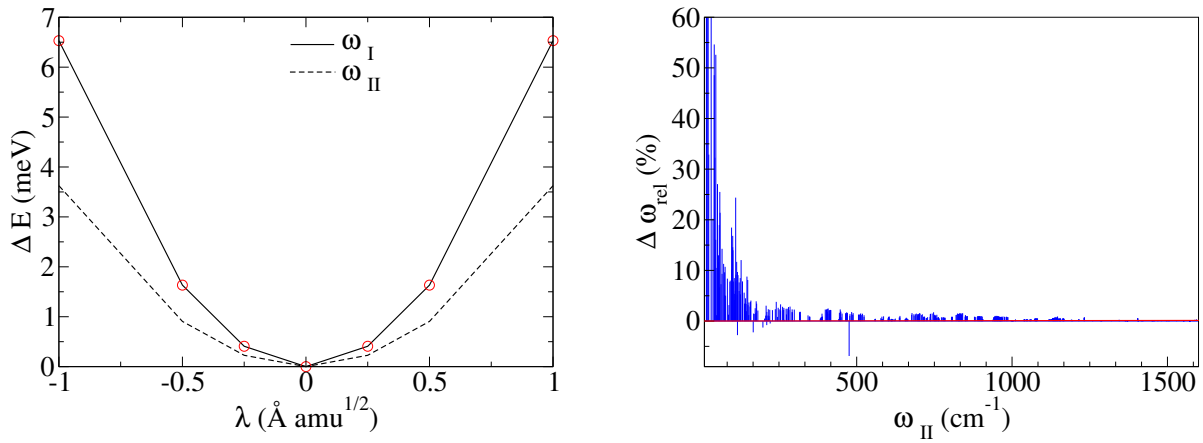

(a) (b)

Fig. 3.3 (a) Change of the total energy of the system with the amplitude of the phonon, (b) Relative frequency change.

3.3 Electron-phonon coupling

Electronic transport in organic semiconductors is dominated by several factors, with the interaction of electrons and phonons being of great importance. The strong electron-phonon interaction taking place in these materials has a much stronger impact on organic semiconductors compared to inorganic ones, as the band widths are much smaller. As a consequence, this interaction implies specific transport characteristics which cannot be described by conventional approaches.

We performed calculation of the electron-phonon coupling in rubrene by using the frozen-phonon method described in the Chapter 2. This method implies displacing the atoms of rubrene by adding each phonon and then calculating the electronic band structure for all frozen-phonons systems. On the Figure 3.4a is shown the calculated band structure of the rubrene crystal without phonon and when one phonon is added. From this figure we can se the impact of specific phonon p on the band structure of rubrene and how the energies of bands are changing by the influence of phonons.

This example illustrates the impact of a vibration of frequency 1593.3 cm^{-1} on the rubrene HOMO bands. This mode is an intramolecular *C-C* stretch mode and as such strongly changes the onsite energy. Each HOMO band in the Figure 3.4a is representing the highest occupied molecular orbital of each molecule in the unit cell. If we follow the changes in the band structure for different amplitudes λ, we can extract the electron-phonon coupling

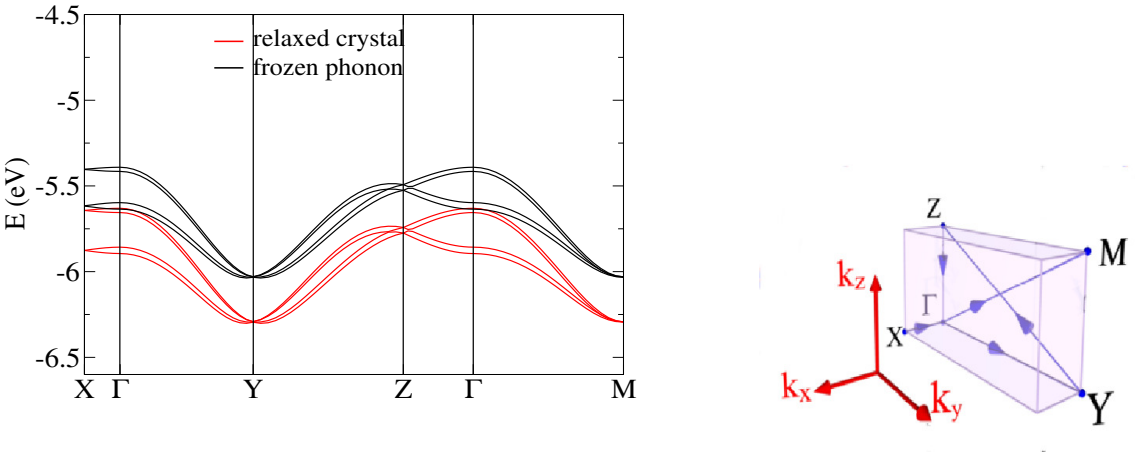

(a) (b)

Fig. 3.4 (a) Changes in the band structure of rubrene with distorted geometry, namely without phonon (red) and with phonon with $\omega^p = 1593.3\ cm^{-1}$ (black); (b) Brillouin zone and definition of special points.

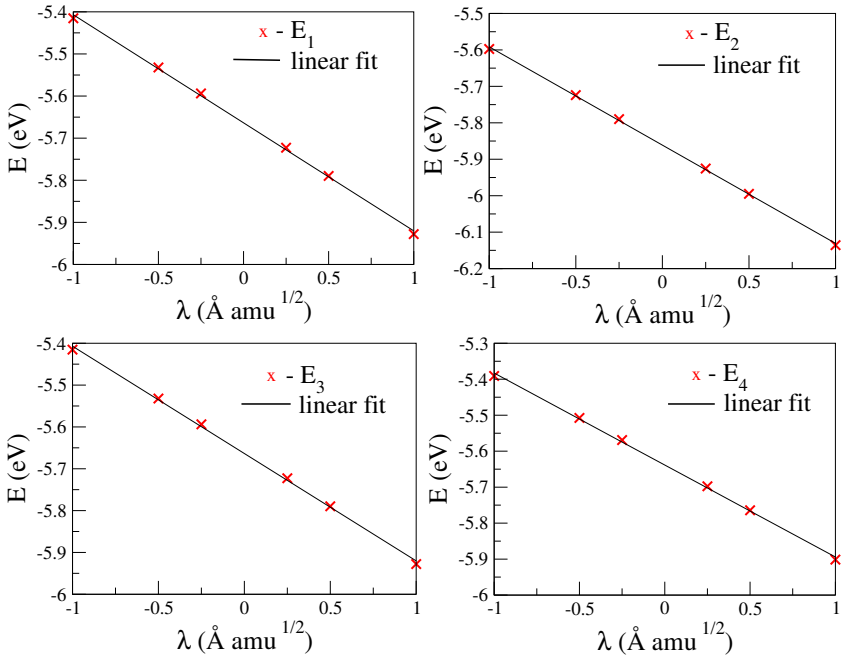

Fig. 3.5 Linear fit for the changes of energy with amplitude for the phonon with $\omega = 1593.3 cm^{-1}$. E_1, E_2, E_3 and E_4 are corresponding to the energies of four HOMO bands at the Γ point calculated for different amplitudes λ.

constants g^p. On the Figure 3.5 are shown the changes in energies of four HOMO bands of the example phonon with $\omega^p = 1593.3\ cm^{-1}$ as the function of amplitude λ for Γ point.

From the linear slope of the changes in electronic energies, $\Delta E/\Delta\lambda$ we can calculate the dimensionless electron-phonon coupling constant using the equation:

$$g^p = \frac{\partial E}{\partial \lambda^p} \frac{1}{\sqrt{2\omega_p^3 \hbar}}$$

Therefore, the averaged electron-phonon coupling constant for the observed mode is $g^{1593.3} = 0.21$. By linear fitting to band structures for all normal modes we could calculate the electron-phonon coupling constants of all phonon modes. On the Figure 3.6 are shown results of the calculation of electron-phonon coupling constants g^p for each phonon p as a function of their frequencies, ω^p. The four graphs are corresponding to the four HOMO bands of the four molecules of rubrene and these results are for the Γ point. The results for the X, Y and Z points of the Brillouin zone are given in the Appendix A.

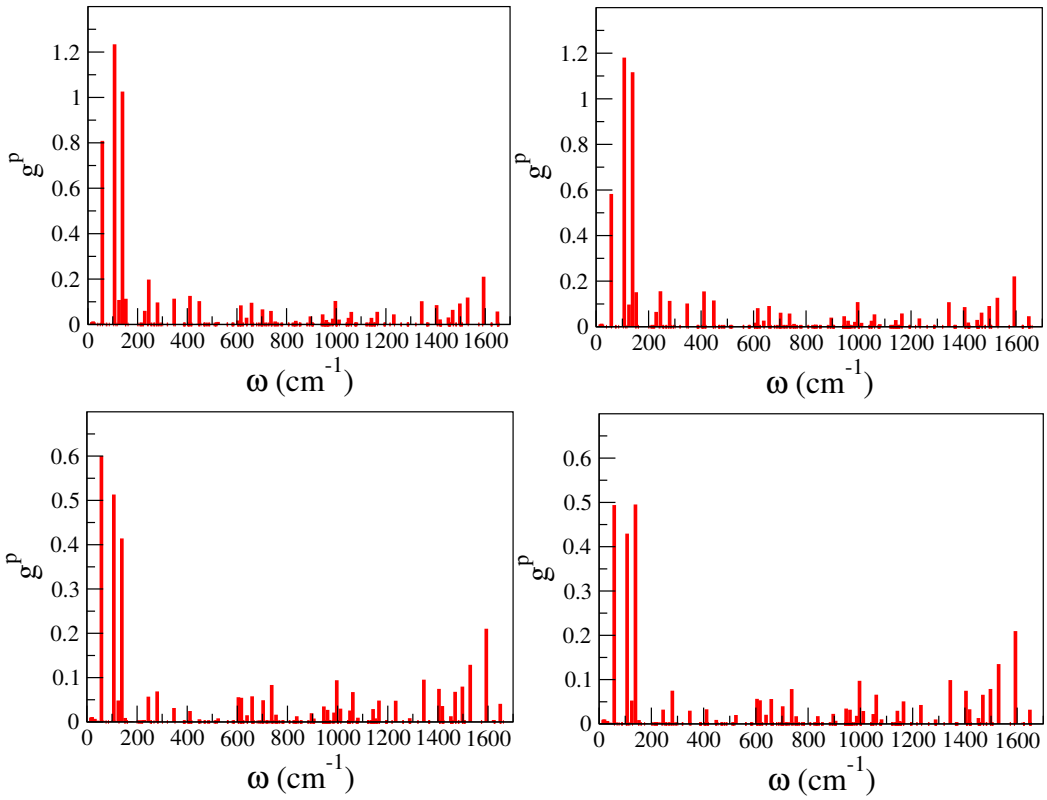

Fig. 3.6 Calculated electron-phonon coupling constants g for the four molecules of rubrene as a function of phonon frequencies ω.

The results show that the highest electron-phonon coupling constants are coming from the low frequency modes. The reason for this is that the most of the low-frequency modes correspond to the vibrations of side phenyl groups around the tetracene backbone of rubrene

molecules and side phenyl rings are mostly responsible for the hopping of charge carriers from one molecule to another in rubrene crystal [43]. Therefore, for the modes with higher frequencies which are mostly corresponding to vibrations of the tetracene backbone we find much weaker electron-phonon interactions. The highest electron-phonon coupling constants in the Figure 3.6 are coming from the three low-frequency modes with averaged coupling constants: $g^{107.3} = 0.83$, $g^{139.1} = 0.76$ and $g^{57.8} = 0.62$.

3.4 The tight-binding calculations

To parametrize electronic properties of rubrene, we perform tight-binding (TB) calculations using the method described in the Chapter 2. Let us first define the transfer integrals in rubrene. From the Holstein-Peierls Hamiltonian:

$$H = \sum_{M,N} \varepsilon_{MN} a_M^\dagger a_N + \sum_{Q=(q,p)} \hbar\omega_Q (b_Q^\dagger b_Q + \frac{1}{2}) + \sum_{Q,M,N} \hbar\omega_Q g_{MN}^Q (b_{-Q} + b_Q^\dagger) a_M^\dagger a_N$$

the first term represents the electronic Hamiltonian which depends on the full set of transfer integrals ε_{MN} of molecules M and N. Due to the high symmetry of the unit cell this set can be reduced such that TB model of rubrene requires only few relevant transfer integrals. On the Figure 3.7 is shown the supercell of rubrene with definition of transfer integrals.

According to the assignments to the molecules in the Figure 3.7, the remaining symmetry-reduced electronic transfer integrals are: ε_{AC}, ε_{AD}, ε_{AB}, ε_{AA+b} and $\varepsilon_{AA\pm 2b}$. Here b indicates a lattice vector in vertical direction and $A+b$ denotes the HOMO orbital of the molecule A in the neighbour unit cell. The coupling between the molecules A and D is negligible and the transfer integral $\varepsilon_{AD} = 0$. For the same reasons we are neglecting ε_{AA+2b} because the values are very small comparing to other transfer integrals.

Applying the TB approach described in the Chapter 2 on the structures including the frozen-phonons distortion we can determine by finite differences the linear changes in the transfer integrals and obtain the Holstein and Peierls coupling constants defined as:

$$g_{Holstein}^p = \frac{1}{\sqrt{2\hbar\omega_p^3}} (\frac{\partial \varepsilon_0}{\partial \lambda})$$

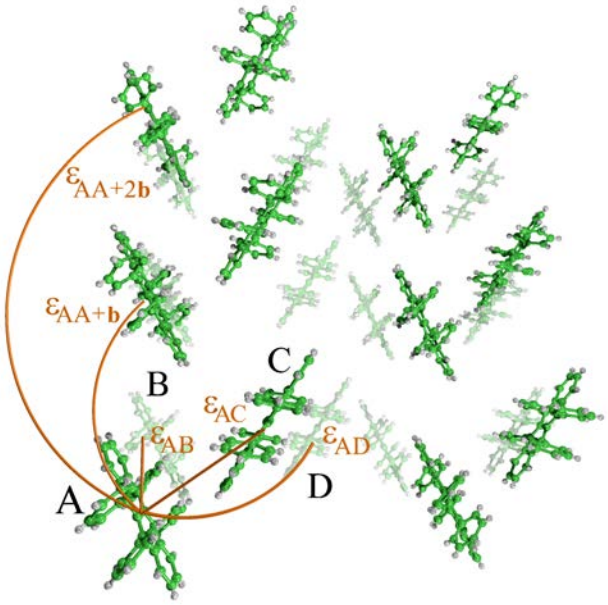

Fig. 3.7 Supercell of rubrene with definition of transfer integrals. A, B, C and D are the four molecules within the unit cell where ε_{AC}, ε_{AD}, ε_{AB}, ε_{AA+b} are the four nearest-neighbour transfer integrals and ε_{AA+2b} is a second neighbour transfer integral along the lattice vector b.

and

$$g^p_{Peierls} = \frac{1}{\sqrt{2\hbar\omega_p^3}}\left(\frac{\partial\varepsilon_i}{\partial\lambda}\right)$$

where ε_i can be ε_{AA+b}, ε_{AB} or ε_{AC}.

The strength of the Holstein and Peierls coupling is expressed by the polaron binding energy, E_H, and by the lattice distortion energy, E_P, respectively, defined as:

$$E_H = \sum_p E^p_H = \sum_p \hbar\omega_p (g^p_0)^2$$

$$E_P = \sum_p E^p_P = \sum_p \hbar\omega_p (g^p_i)^2$$

Here E^p_H and E^p_P are mode-resolved Holstein and Peierls contributions respectively and E_P consists of all Peierls coupling constants for all nearest neighbours of a specific molecule.

On the Figure 3.8 are shown results of the calculated E_H and E_P. As we can see from the figure, the majority of the 840 modes have electron-phonon coupling close to zero. Modes with non-local couplings dominate the low-frequency part ($< 150 cm^{-1}$) with E_P over 4 meV from strongly coupled B_{3g} modes (blue lines). In the high-frequency part dominate local couplings and a few strong coupling modes can be found around 1600 cm^{-1} (red lines). A selected list of the calculated values is shown in the Table 3.3 and compared with the results from the Ref. [69].

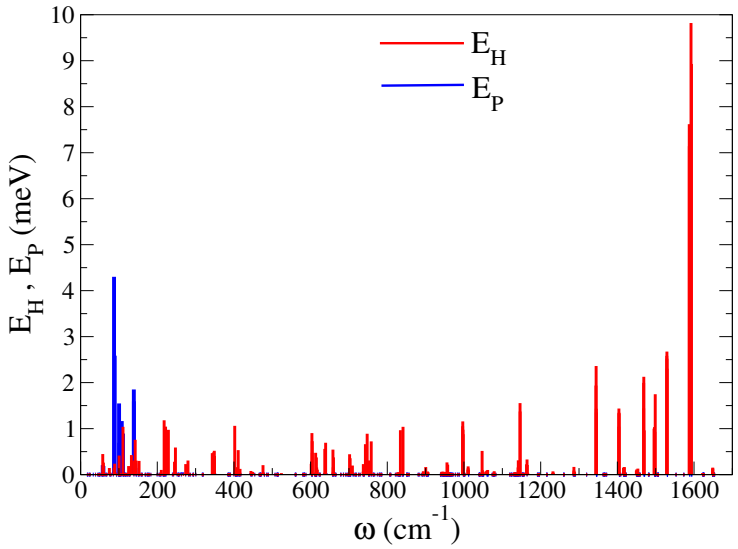

Fig. 3.8 Calculated polaron binding energy (red lines) and lattice distortion energy (blue lines) and a function of phonon frequencies.

From our results we can see that only the inversion symmetric modes A_g and B_{2g} would affect the onsite energies of the molecules and would contribute to g_H^p. According to the general symmetry of rubrene, ant-symmetric modes are not playing important role in the electron-phonon interaction as they are coupling very weakly with the crystal lattice.

From the Table 3.3 most of the strongly coupled modes are in agreement with the values from Ref. [69]. Only for the low-frequency modes we observe some deviations between the literature and our results in the electron-phonon coupling constants. However, comparing the integral values of E_H and E_P for all 840 modes to those derived in Ref. [69] in table 3.4 we find rather good agreement. The calculated polaron binding energy and lattice distortion values coincide well with Refs. [45] and [69]. Deviations of the coupling strengths of single modes in low-frequency range in our results comparing to the literature can be explained by

this work			Ref. [69]		
ω_p (cm^{-1})	$\omega_p g_0^p$ (meV)	$\omega_p g_i^p$ (meV)	ω_p (cm^{-1})	$\omega_p g_0^p$ (meV)	$\omega_p g_i^p$ (meV)
57.8	−1.7	0.85	37.4	−0.9	3.4
59.6	1.4	−0.83	66.6	1.6	6.6
89.0	1.6	−4.8	87.7	−0.6	−9.3
107.3	−0.14	2.8	106.3	0	−4.4
139.1	−2.3	−3.7	125.1	1.4	−4.7
639.1	−7.5	1.0	631.2	−10.8	1.3
1011.2	−3.6	−0.04	1002.3	24.6	0
1344.7	19.8	0.04	1348.6	49.9	0
1593.3	−42.0	0.12	1593.8	−45.6	1.6

Table 3.3 Comparison of electron-phonon coupling strength for several phonons.

different treatment of the intermolecular interaction. Further useful quantities for comparison with literature are effective Holstein ω_H and Peierls ω_P mode frequencies defined as:

$$\hbar\omega_H = \frac{\sum_p (\hbar\omega_P g_0^p)^2}{E_H}$$

$$\hbar\omega_P = \frac{\sum_{p,i} (\hbar\omega_P g_i^p)^2}{E_P}$$

Our results show larger effective Peierls mode frequency ω_P comparing to the reference values because of the different low-frequency electron-phonon coupling constants.

	This work	Ref. [45]	Ref. [69]
ε_{AA+b} (meV)	134.0	143	125
ε_{AC} (meV)	28.9	23	−6
ε_{AB} (meV)	4.1	-	-
ε_{AB} (meV)	−10.7	-	-
E_H (meV)	106.8	159	99
E_P (meV)	21.9	-	20
ω_H (cm^{-1})	1208.9	1400	1277
ω_P (cm^{-1})	117.9	50	77

Table 3.4 Transfer integrals and effective electron-phonon coupling parameters E_H, E_P, ω_H and ω_P in the present work and comparison to literature values

In the Figures 3.9a and 3.9b are shown the calculated dimensionless Holstein and Peierls coupling constants g_0^p and g_{AA+b}^p respectively. The highest values for Holstein coupling constants are $g_0^{110.6} = 0.28$, $g_0^{57.8} = 0.25$ and $g_0^{1593.3} = 0.21$, which was an example phonon shown in the Figure 3.4a and for which the DFT and TB calculated electron-phonon coupling constants have the same values. The Peierls coupling constants g_{AA+b}^p are high for the low-frequency modes but after 800 cm^{-1} they vanish.

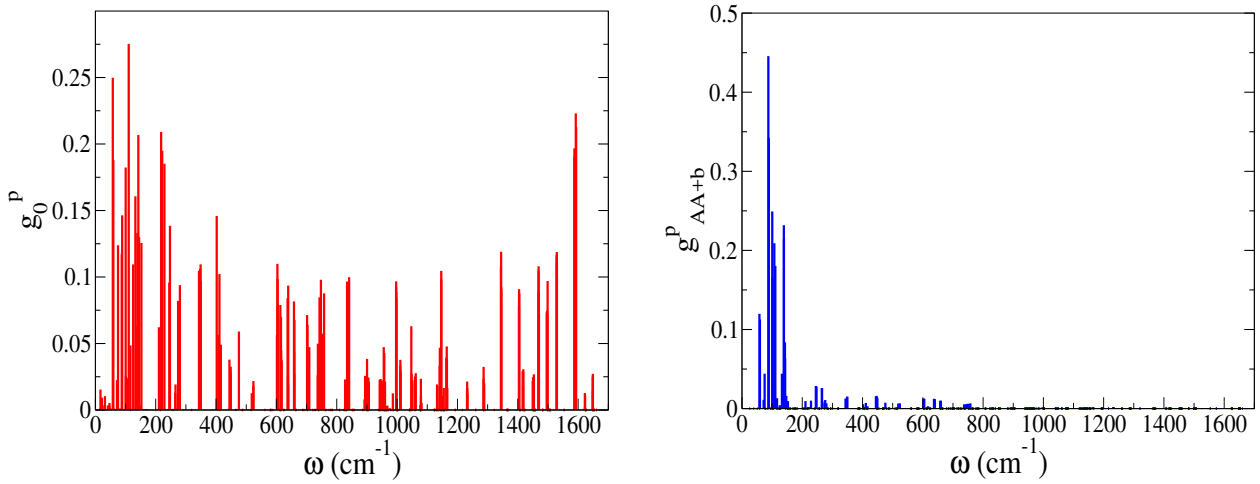

(a) (b)

Fig. 3.9 Spectrally resolved (a) dimensionless Holstein g_0^p and (b) Peierls g_{AA+b}^p coupling constants.

From the given mode patterns of relevant modes we notice that the inter-molecular electron-phonon coupling is associated with the motion of phenyl rings. This in particular corresponds for the modes with torsion of the phenyl rings like e.g. mode from Figure 3.3a with $\omega_p = 59.6\ cm^{-1}$ with dimensionless coupling constants $g_0^p = 0.19$ and $g_{AA+b}^p = 0.12$. However, phenyl ring wagging modes that move perpendicular to the tetracene plane, couple only weakly to the molecular orbitals. The impact of those flipping motions, which has been discussed in literature [73], is investigated in the following section.

3.5 Flipping motion of phenyl groups

In this section we investigate if the motions of the side phenyl groups can be stronger than suggested by the weak electron-phonon coupling associated to these vibrations. Motivated by the work of Kloc et al. [73], we performed Molecular dynamics simulations in the constant

temperature ensemble using a Nose-Hoover thermostat and time step of 0.5 fs. According to the model suggested in Ref. [73], the two phenyl groups from the same side of the of rubrene would change their positions relative to the tetracene backbone from above to below the tetracene plane and vice versa.

Rubrene is a molecular crystal which molecules are bounded to each other via van der Waals forces, Figure 3.2. The tetracene backbone of rubrene molecule is made of four fused benzene rings. On each side of the tetracene backbone are two substituted phenyl groups which are very flexible and are vibrating around their equilibrium positions above and bellow the backbone plane on each side due to mutual repulsion.

We investigate the possibility of flipping phenyl groups by calculations with a supercell which is twice the original cell and consists of eight molecules of rubrene. For one of the eight molecules we changed the positions of the phenyl rings to the other side of the tetracene backbone and let the structure relax its energy in the DFT simulations. Observing the relaxation of supercell we saw that the starting configuration is not a stable minimum and that the phenyl groups are moving back to their original positions of the undistorted crystal.

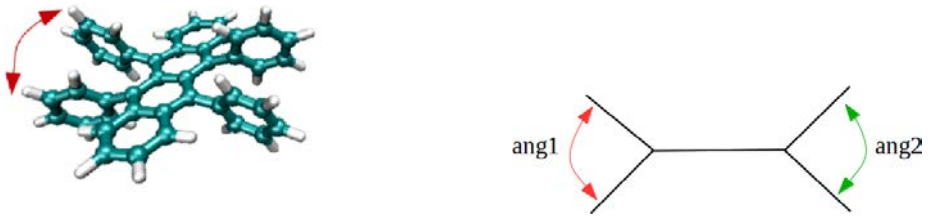

(a) (b)

Fig. 3.10 Definition of the two angles between phenyl groups perpendicular to the tetracene backbone plane in (a) perspective and (b) schematic views.

To analyze the influence of finite temperature on the phenyl groups dynamics we studied their motions with Molecular dynamics simulations. The expectation was that increasing the temperature, the phenyl groups would vibrate so much that they would gain enough energy to flip to the other side of the tetracene plane. For these simulations we define the bonding angles ang_1 and ang_2 as in the Figure 3.10 and follow the change of the angles over time for various temperatures up to 500 K.

On the Figure 3.11 is shown the dynamics of the phenyl groups only for the highest temperature of 500 K for all eight molecules, while the results for 100 K, 200 K and 300 K are given in the Appendix B. We see that the phenyl groups are vibrating strongly but that there are no changes in the sign of angles which would indicate that the phenyl groups flipped to the other side of the tetracene plane. As the phenyl groups are not flipping even at extremely high temperatures such as 500 K suggests that, they are most likely unable to cross

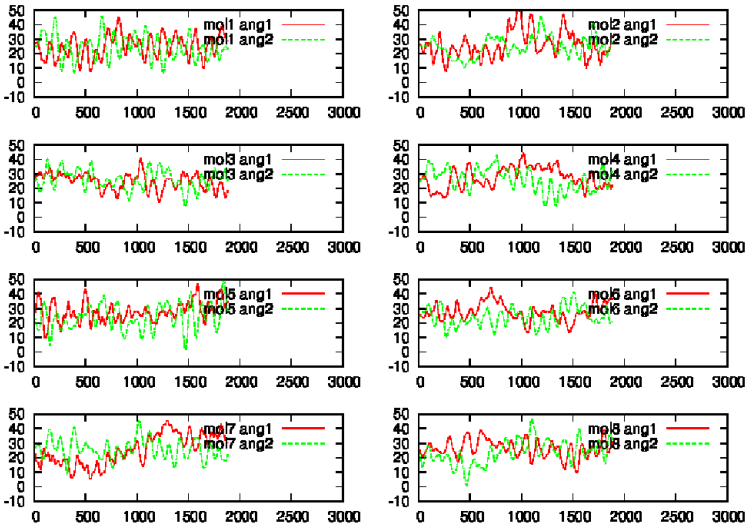

Fig. 3.11 Phenyl group dynamics measured with angles ang_1 (red) and ang_2 (green) at $T = 500$ K. Eight graphs correspond to the eight molecules of the supercell.

the backbone plane at ambient temperatures in comparable time. Therefore, we conclude that the scenario suggested in Ref. [73] could not be confirmed in our calculations nor its possible influence on the transport properties of rubrene.

For lower temperatures we have similar results as the one on the Figure 3.11 but with weaker oscillations of the angles. In the Table 3.5 are given the results of the analysis of the average angles by interpreting the MD trajectory as statistical ensemble and averaging over ang_1 and ang_2. These results are for all temperatures. Notice that the average angle is independent of T but that its standard deviation increases with T and reaches 22% at 300 K. In addition, we do not eliminate the possibility of the flipping occurrence in rubrene at larger time scales, but we do not observe them in our calculations in the time scale of one picosecond and we do not find such flipping configurations to be a (meta)stable minimum.

T (K)	Ref $\overline{angle}$ (deg)	$\sigma(angle)$ (deg)
100	25.6	3.0
200	25.3	4.3
300	24.9	5.4
500	25.8	7.6

Table 3.5 Temperature dependent mean value and standard deviation of the angular difference ang_i averaged over each molecule and each side i.

3.6 Conclusion

We derived reliable and efficient method for calculation of material parameters from DFT approach and applied it on rubrene. DFT-based methods were used to compute all relevant electronic, phononic and electron-phonon coupling parameters of rubrene which served as a prototype of a complex organic material build from a molecular core and functional side groups. We showed a practical way to get accurate frequencies and avoid imaginary frequencies in low-frequency modes that often occur in DFT-based methods. From DFT calculations we derived TB model to compute parameters for the Holstein-Peierls type Hamiltonian which can be directly applied in charge transport calculations and studies of specific properties of materials such as density of states, conductivity, carrier mobility, etc. Calculation of phonon modes, electron-phonon coupling and phenyl group motions in rubrene has led us to the following conclusions:

- The accuracy of phonon frequencies is of the highest importance in the calculations of electron-phonon interactions. This particularly refers to the low-frequency modes which frequencies may contain accumulated numerical errors from the forces in the direct diagonalization of the dynamical matrix.
- The highest electron-phonon coupling constants are coming from the low-frequency modes which correspond to the vibrations of side phenyl groups around the tetracene backbone in rubrene. Therefore, we find that electron-phonon interaction in rubrene is mostly dependent of the vibrations of phenyl groups.
- The results from TB calculations presented in this work are in very good agreement with the ones in literature. This confirms that our computational method is correct and assures us in reliability of our results.
- In the calculation of phenyl group motions we do not find the flipping configuration is stable and we could not reproduce the model suggested in Ref. [73] in the time scale of one picosecond. Nonetheless, we do not dismiss the possibility of the flipping phenyl rings occurrence in rubrene at larger time scales.

Chapter 4

Monophosphate Tungsten Bronzes

4.1 Introduction

There has been a great interest in low dimensional transition metal bronzes for several decades. The term *bronze* is commonly used for a variety of transition metal oxides with the general formula $A_xM_yO_z$ where A is an alkali or alkali-earth metal and M is a transition metal [74]. They were discovered in the nineteenth century by Wöhler who called them "bronzes" because of their metallic gloss [75]. The bronzes have intense colour with metallic sheen, they are chemically inert and exhibit metallic or semiconducting behaviour. Although there has been a great interest in bronzes, the research in this area boosted after the discovery of charge density waves (CDW) in the blue and purple bronzes in the early 1980's [76, 77]. Transition metal bronzes are now extensively studied because of their electric, magnetic and structural properties [78–85]. Such specific characteristics originate from the possibility to obtain partial oxidation states of the transition metal atoms.

Monophosphate tungsten bronzes (MPTB) rank among the more intensely studied bronzes. They are showing phase transitions as a function of temperature such that a series of charge density waves (CDWs) is apparently established [31, 86–93]. The structure of these materials leads to anisotropic physical properties evidenced by the electrical conductivity and magnetoresistance [80–82, 91, 93, 94].

The crystal structure of monophosphate tungsten bronzes is three dimensional where a series of perovskite related W-O octahedral step layers are linked by PO_4 tetrahedra [79, 83, 95–105]. The crystal structure of one of these bronzes, $P_4W_8O_{32}$, is shown on the Figure 4.1. As for all members of this family, octahedral step layers are linked by PO_4 tetrahedra generating pentagonal tunnels. The different members of the series differ in the number of octahedra in the repeat unit of the layer which, in the case of Figure 4.1, is four. At the junction of WO_6 octahedral layers through PO_4 tetrahedra, the pentagonal or

hexagonal tunnels can be created, and for that reason, the monophosphate tungsten bronzes with pentagonal tunnels are called the $MPTB_p$s and the ones with hexagonal tunnels the $MPTB_h$s. The $MPTB_h$ phases are found with alkali-metal atoms Na or K in their hexagonal channels and their formulas are given by $A_x(PO_2)_4(WO_3)_p(WO_3)_q$, where A represents the alkali-metal atom.

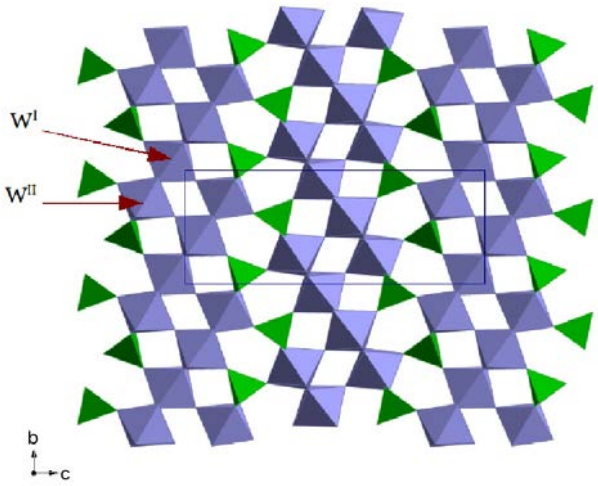

Fig. 4.1 View of the crystal structure of the $m = 4$ member of the $MPTB_p$ along the a-axis: the purple objects are WO_6 octahedra and the green ones PO_4 tetrahedra.

All MPTB phases have two perovskite-based W-O layers per unit cell. The general formula for $MPTB_p$s can be written as $(PO_2)_4(WO_3)_p(WO_3)_q$. The indices p and q are even or odd integers. They show the number of WO_6 octahedra used to form each W-O layer. Usually p and q are identical, thereby leading to the alternative formula $(PO_2)_4(WO_3)_{2m}$. However, in some cases p and q are not identical, as in $(PO_2)_4(WO_3)_4(WO_3)_6$. This member contains two W-O layers per unit cell where one layer contains four and the other layer six WO_6 octahedra per repeat unit [96]. The value of integer m determines the width of the W-O layer, or actually the parameter c of the unit cell, while a and b parameters are practically not changing with m. Although not all $MPTB_p$ structures are described with the same crystallographic axes, in this general introduction to the electronic structure of $MPTB_p$ phases we will use the system of axes shown on Figure 4.1 for all members of the series.

The Magnéli phases, γ- and $\eta - Mo_4O_{11}$, contain the same perovskite-type layers and are isostructural with the $MPTB_p$ and $MPTB_h$ with $m = 6$, respectively [106–109]. Therefore it is expected to observe also very similar electronic properties, since W-O layers of the MPTB phases have the same structure as Mo-O layers of the Magnéli phases and since W and Mo

atoms are in the same family of the Periodic Table [110, 111]. However, note that the band filling is slightly different.

Electronic transport and magnetic properties measurements imply metallic behaviour of monophosphate tungsten bronzes [80–82, 91, 94, 112–114]. Previous electronic structure studies show that $MPTB_p$ phases have well-nested 1D and 2D Fermi surfaces [31, 90, 115, 116] and it has been found that they are showing different resistivity anomalies [80–82, 85, 86, 88, 91, 93, 94, 116–118]. Thus, it was proposed that these resistivity anomalies are originating from charge density wave (CDW) instabilities associated with the Fermi surface nesting. This was initially predicted from similarity with the Magnéli phases, which are exhibiting well characterized resistivity anomalies and CDWs associated with the partially filled t_{2g}-block bands of their perovskite Mo-O layers [110], and later verified by electronic structure calculations [31].

The tungsten atoms with their partially filled d-orbitals from the perovskite W-O layers are responsible for the conduction properties of $MPTB_p$s [31, 90, 92]. As we could see from the crystal structures, the thickness of tungsten layers in $MPTB_p$s depends of the integer m but, as we will show later, the number of electrons per layer filling the partially filled bands is always 2 independently of m. In the $MPTB_h$ phases electron counting is slightly different because of the alkali-metal atoms in their hexagonal channels.

In order to understand the electronic properties of the $MPTB_p$ phases, one has to examine how their electronic structures are related to the crystal structure, the octahedral distortion and the average oxidation state of tungsten. The crystal structure of $MPTB_p$ series shows that the octahedral distortions in the W-O layers are not uniform. Although it has been proposed that the complex resistivity curves of these materials are due to the occurrence of successive CDWs, it is not yet clear that all of these modulations can be explained by a Fermi surface driven mechanism. This is the reason why we decided to reconsider the electronic structure with special emphasis on the calculation of the Lindhard response function. In this chapter we will report the electronic band structure, Fermi surface and Lindhard response function for several $MPTB_p$ phases, with $m = 4, 5, 6, 7, 8$ and 12 in order to characterize the origin of their structural modulations and resistivity anomalies.

4.2 Electronic structure of $MPTB_p$s

In our study the band structure and Fermi surface calculations were done using density functional theory (DFT) as implemented in the SIESTA code [10–13]. Several members of $MPTB_p$ phases, the ones with $m = 4, 5, 6, 7, 8$ and 12, were taken into account and their experimental crystal structures were used in our study. The calculations were carried out with

generalised gradient approximation (GGA) using an energy cut off of 350 Ry and k-point meshes of $20 \times 20 \times 10$. There have been several theoretical investigations of the electronic band structure of monophosphate tungsten bronzes done in the past [31, 87, 90, 92, 115, 116, 119]. However, these calculations were mostly done using the extended Hückel tight-binding method [120] and, only more recently, *ab initio* methods have been used [89, 121, 122].

In Figure 4.2 is shown an example of the calculated electronic band structure near the Fermi level for the member $m = 4$ of the $MPTB_p$s. Six bands, the lowest bands of the t_{2g}-block, are crossed by the Fermi level. In the previous tight-binding calculations, only the isolated octahedral layers were considered. Consequently, the number of partially filled t_{2g} bands was half the number of bands in DFT calculations which takes into account the full structure. The use of isolated octahedral layers in the tight-binding studies is justified by the fact that the PO_4 tetrahedra almost completely decouple different layers as shown in the Figure 4.2 (see the Γ-Z line associated with the interactions along the c-axis, where the splitting of the bands within any pair is very small).

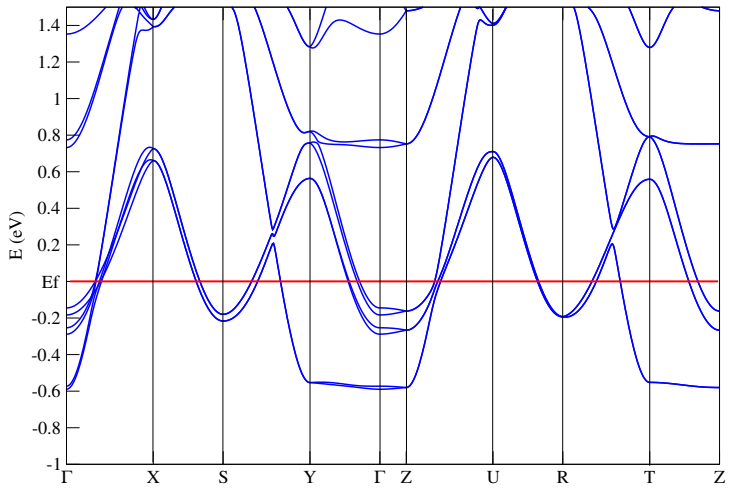

Fig. 4.2 The electronic band structure for the $m = 4$ member of the $MPTB_p$ (see Figure 4.3 for the labeling of the high symmetry points).

The Brillouin zone appropriate to the orthorhombic structure of most of the $MPTB_p$s is shown in the Figure 4.3. Note that although the $MPTB_p$s with $m = 4, 6, 8$ and 12 have orthorhombic crystal structures, those with $m = 5$ and 7 have monoclinic lattices [79]. However, since the derivation from the orthorhombic symmetry is very small, in all the band

structures we have used an orthorhombic representation. This helps in comparing results for different systems.

The band structure calculations have shown that the electronic structure of all compounds of the $MPTB_p$ family is very similar. The Figure 4.2 shows that, as predicted, the lowest part of the t_{2g} bands is always made of three pairs of bands which are almost degenerate [123]. This is because there is a weak interaction between the two layers of the unit cell. From the calculated band structures we can see that one pair of bands has quasi 1D character: it is flat along the Γ-Y and Γ-Z directions but dispersive along Γ-X. There are also two pairs of bands which are apparently 2D. As it will be shown later, this is not correct; it is due to the nature of the symmetry lines displayed in the band structure. These two pairs of bands look as 2D but really are also 1D bands along the $a+b$ and $-a+b$ directions.

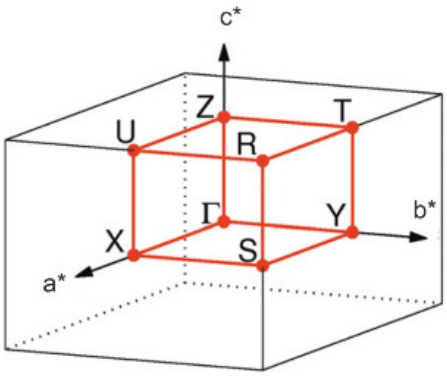

Fig. 4.3 Brillouin zone for the orthorhombic $MPTB_p$ phases showing the high symmetry directions.

4.3 Fermi surface and nesting vectors

Before looking in more detail at the DFT results we need to have a clear idea of the general shape of the partially filled bands of these bronzes as well as how they are related to the actual crystal structures. With the typical oxidation scheme of P^{5+} and O^{2-}, the average oxidation state of W in a $MPTB$ with formula $A_x(PO_2)_4(WO_3)_p(WO_3)_q$ is given by $6-(4+x)/(p+q)$. Consequently, a unit cell of an $MPTB$ phase has $4+x$ electrons or, in the case of $MPTB_p$ with $p=q=m$, 2 electrons per octahedral layer. Consequently, only the lower t_{2g} bands of the octahedral layers may be filled [31, 90, 92].

Let us now describe the structural patterns of the perovskite type octahedral layers by considering the case of $m=4$ [95]. The W_4O_{21} unit of Figure 4.4a is built from four WO_6 octahedra by sharing the equatorial corners, and the W_4O_{18} chain of Figure 4.4b is obtained

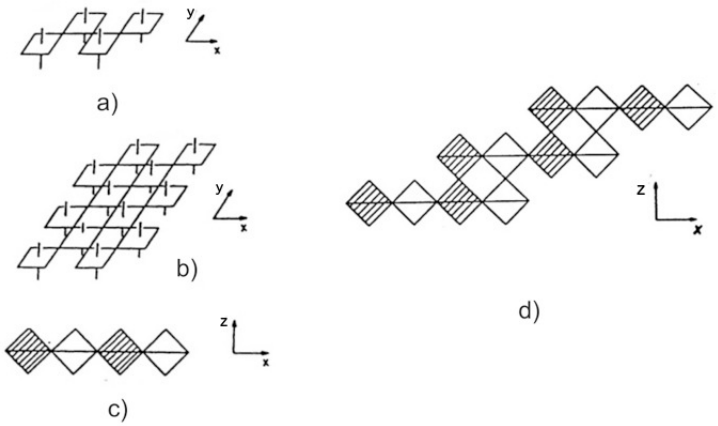

Fig. 4.4 Building up of the octahedral layers of $MPTB_p$ with $m = 4$.

by condensing these W_4O_{21} units. The W_4O_{18} chain can be represented by the projection view shown in Figure 4.4c along the chain direction. The W_4O_{18} chains of Figure 4.4c can be condensed to lead to the W_4O_{16} layers of Figure 4.4d by sharing their axial oxygen atoms. In the W_4O_{16} layer, the first octahedron of one W_4O_{18} chain shares its axial oxygen atoms with the third octahedron of the adjacent W_4O_{18} chain (i.e., a 1,3-condensation).

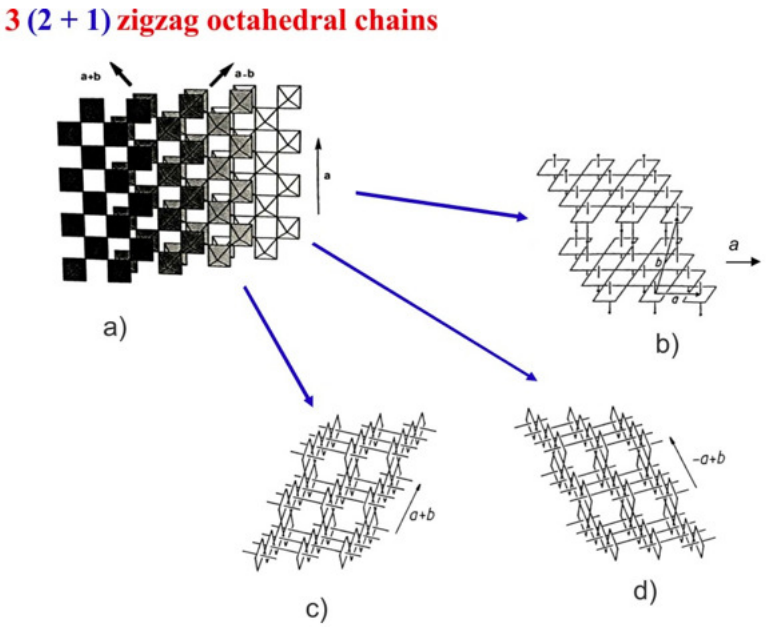

Fig. 4.5 Schematic diagram showing the occurrence of zigzag chains along the a, $a+b$ and $-a+b$ directions in the octahedral lattice of $MPTB_p$ with $m = 4$.

If the W_4O_{16} layer of Figure 4.4d is seen from the top (i.e., the z direction), it can be represented as in Figure 4.5a. This layer can be redrawn in three different ways, as done

in Figures 4.5b, 4.5c and 4.5d, showing that the step layers of the $m = 4$ member of the $MPTB_p$ family, contains octahedral zigzag chains along a, $a+b$ and $-a+b$ directions. This structural description is completely general and applies to all phases of the $MPTB_p$ series. The only difference is the number of octahedra in the initial octahedral cluster (Figure 4.4a).

The t_{2g} orbitals of one of the WO_6 octahedra are such that the d-orbital containing planes can be chosen to be aligned along the a, $a+b$ and $-a+b$ directions of the step layers of $MPTB_p$ (i.e., those shown in Figures 4.5b, 4.5c and 4.5d), respectively. Every t_{2g} orbital thus makes δ type interactions with those of neighbouring parallel chains but π type interactions along the chain [90].

For a given elementary unit like that of Figure 4.4a, the lowest t_{2g} orbital combination that can be built is shown in Figure 4.6. Repeating this type of orbital combination with the appropriate phases and adjusting the oxygen p-orbital contributions in the shared positions, one of the three lowest t_{2g} bands of each layer, that being strongly dispersive along the a direction, may be generated. The remaining two t_{2g} orbitals lead to the other two low lying t_{2g} bands of each layer (i.e., those strongly dispersive along $a+b$ and $-a+b$ directions) by the same process.

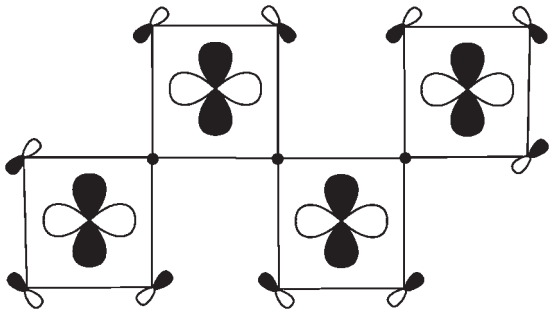

Fig. 4.6 Lowest lying combination of one of the three t_{2g} orbitals leading to one of the three low lying t_{2g} bands of $MPTB_p$ with $m = 4$. Black dots denote positions where oxygen p-orbitals do not mix because of the local symmetry.

Thus, we conclude that there will be three t_{2g} low lying bands per layer dispersive along one of the three intrachain directions (a, $a+b$ and $-a+b$) but dispersionless along the interchain directions. In addition, due to the local orthogonality of the t_{2g} orbitals the three bands are practically independent from one another to a first approximation. Consequently, the three t_{2g} bands per layer of the $MPTB_p$s can be approximated by three independent 1D bands resulting from the three t_{2g} orbitals [90]. This description applies to all systems considered in the chapter.

As we saw from the calculated band structure, there are three pairs of bands of which one pair has quasi 1D character and the other two pairs quasi 2D character. However, the

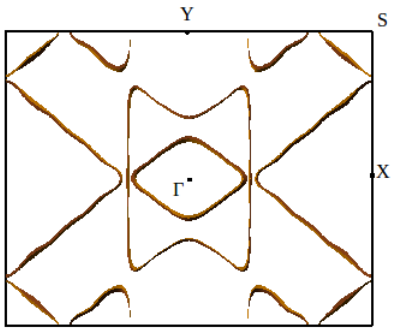

Fig. 4.7 View along c^* of the Fermi surface for the $m = 4$ member of the $MPTB_p$. $\Gamma = (0,0,0)$, $X = (a^*/2,0,0)$, $Y = (0,b^*/2,0)$ and $S = (a^*/2,b^*/2,0)$.

qualitative analysis of the band structure leads to the prediction that there must be three 1D partially filled bands per layer and thus, three 1D Fermi surfaces per layer. The calculated Fermi surface for the $m = 4$ member of the $MPTB_p$s is shown in Figure 4.7. As it will be seen along this chapter, the Fermi surfaces of all $MPTB_p$s have a similar shape.

As shown in Figure 4.8, this Fermi surface can be considered to result from the combination of a pair of 1D Fermi surfaces (Figure 4.8b) and the "rhombus shape" Fermi surfaces of Figure 4.8c. The Fermi surfaces of Figure 4.8b are 1D along the a^* direction (i.e., they are made of two pairs of planes perpendicular to the a^* direction and to the plane of the paper) and are associated with the 1D bands of Figure 4.2. Thus, according to the previous analysis of the band structure, the Fermi surface of the Figure 4.8c should result from the combination of the two pairs of 1D Fermi surfaces along the $a+b$ and $-a+b$ directions. Indeed, this is exactly what is found in the Figure 4.8c, which can be considered to be the combination of a series of planes perpendicular to the a^*+b^* and $-a^*+b^*$ directions of the Brillouin zone. In other words, the Fermi surface of Figure 4.7 can be decomposed into a set of three pairs of 1D Fermi surfaces, as schematically shown in Figure 4.9.

At a first look, the Fermi surface of Figure 4.7 may seem to be built from a series of closed and poorly nested portions. This is specially so when the individual contributions of the different bands are separately plotted. A low-dimensional metal with several partially filled bands may lead to apparently unnested Fermi surfaces even if their "intended" surfaces (i.e., those expected in the absence of the avoided crossings) are all nested. In this case, the nesting is "hidden" by the avoided crossings [124]. Such hidden, nested Fermi surfaces can lead to CDWs thereby destroying the nested portions of the combined Fermi surfaces.

In the case of $MPTB_p$s, the Fermi surface has "hidden" one-dimensionality: the final Fermi surface reveals that there are many parallel parts of Fermi surface perfect for nesting [31, 90, 92]. From previous analysis one can draw the expected nesting vectors, like in

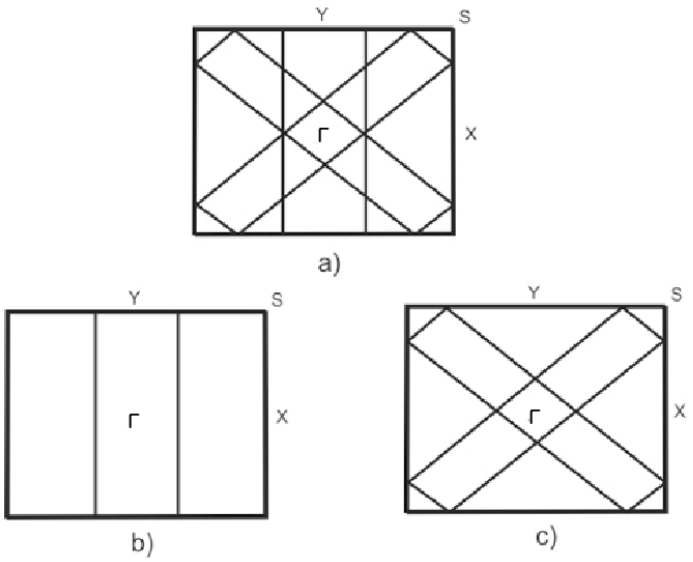

Fig. 4.8 Schematic decomposition of the Fermi surface of the Figure 4.7 (a) into a pair of 1D Fermi surfaces associated with 1D bands (b), and the contribution of the apparently 2D bands (c). We assume nil interactions between the different octahedral layers: every line in this diagram is really the superposition of two identical lines associated with one of the two layers.

the Figures 4.10a and 4.10b. In doing so, we must take into account that in one case like in that of Figure 4.7 (or as the idealized version of Figure 4.8a) there are several nesting vectors, common to two pairs of 1D Fermi surfaces. Since the lattice distortion associated with a CDW induces a lattice strain, the lattice vibration most likely to couple with the CDW instability of a nested Fermi surface is that leading to a maximum electronic energy stabilization, i.e. that whose wave vector provides the maximum possible nesting. Thus, in these cases it is frequently observed that the nesting vector associated with the CDW is one of the common nesting vectors for several Fermi surface components. For instance, given the Fermi surface of Figure 4.9, there are two kinds of possible maximum nesting vectors: (i) those being common to the two Fermi surfaces originating from 1D chains along the diagonal directions (i.e. those in Figures 4.9b and 4.9c), (ii) those being common to one of these Fermi surfaces and that along a. Some examples of both types are shown on the Figures 4.10a and 4.10b. Note that some possible nesting vectors are redundant. For instance, q_3 and q_5 in Figure 4.10b have the same component along a^* whereas the components along b^* are related by $q_3^{b^*} = b^* - q_5^{b^*}$.

The calculated Fermi surfaces are somewhat warped compared to the hidden ones of the Figure 4.9. Since the warping in general is small, the common nesting vectors derived from the hidden Fermi surfaces are most likely the relevant ones for actual compounds. In

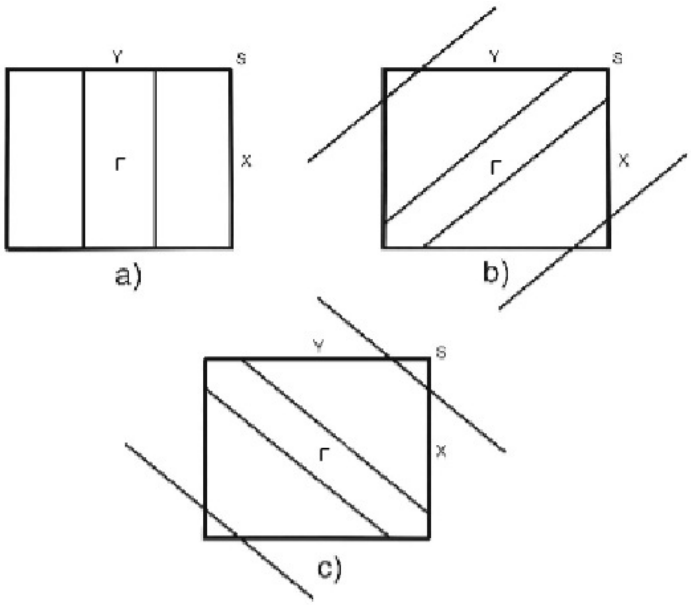

Fig. 4.9 Decomposition of the Fermi surface of Figure 4.7 into the hidden 1D Fermi surfaces associated with chains running along the a direction (a), the $-a+b$ direction (b) and the $a+b$ direction (c). We assume nil interactions between the different octahedral layers: every line in these diagrams is really the superposition of two identical lines associated with one of the two layers.

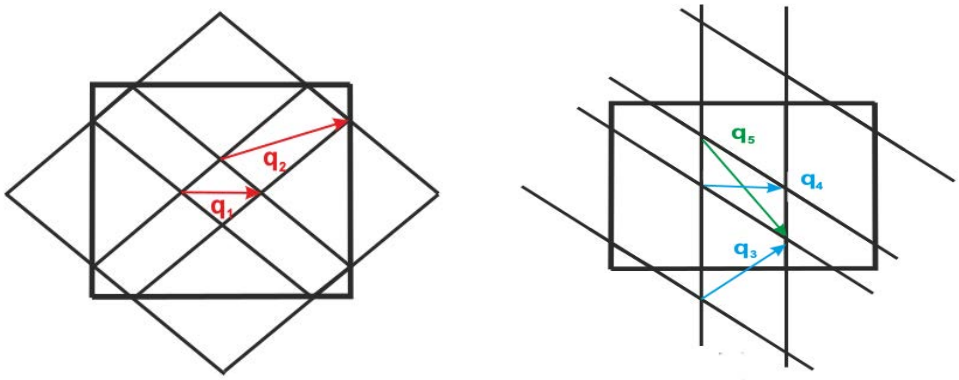

(a) (b)

Fig. 4.10 Illustration of common nesting vectors associated with (a) two 1D chains along the diagonal directions and (b) one 1D chain along a and one 1D chain along a diagonal direction.

that case, the CDW may not completely remove the Fermi surface thereby creating small electron and hole pockets. In some cases, the resulting pockets may even lead to an additional CDW formation. In any case, the Fermi surface driven CDWs expected in $MPTB_p$ will never completely destroy the Fermi surface and thus, will be associated to metal-metal transitions.

The analysis developed up to now provides a simple yet convenient framework to understand the results of the detailed DFT calculations reported in this chapter.

4.4 Lindhard response function calculation

A CDW instability is coupled to the lattice via the electron-phonon coupling. In linear response theory, the relevant response of the electrons in band n to a static modulation of the underlying ionic lattice with wave vector $\vec{q}$ is given by the electron-hole Lindhard response function [6]:

$$\chi(\vec{q},T) = -\sum_{\vec{k}} \frac{f(E_n(\vec{k}+\vec{q})) - f(E_n(\vec{k}))}{E_n(\vec{k}+\vec{q}) - E_n(\vec{k})}$$

where $E_n(\vec{k})$ is the energy associated with the band n at the point $\vec{k}$ of the Brillouin zone and $f(E_n(\vec{k}))$ the Fermi-Dirac distribution function associated with this state. The Lindhard response function is large when many states at the Fermi level are coupled with the wave vector $\vec{q}$. This occurs when the Fermi surface contains portions which may be superimposed onto one another through a translation by a vector $\vec{q}$, which is the so-called nesting vector. As discussed in the first chapter, for a purely 1D metal at $T = 0$ K, the Fermi surface is perfectly nested with $q = 2k_f$ and the Lindhard response function then exhibits a divergence leading to a CDW state. In higher dimensionality systems, the Lindhard response is more complex and needs careful evaluation.

Here are going to be presented the results of Lindhard response function calculation for the members of monophosphate tungsten bronzes ($MPTB_p$s) with $m = 4,5,6,7,8$ and 12. The comparison of calculated Lindhard response function with observed modulation vectors will be used to discuss the likeliness of the Fermi surface nesting mechanism as the origin of the different modulations observed in these materials.

4.4.1 $MPTB_p$ with $m = 4$

The $m = 4$ member along with the $m = 6$ member, has been studied extensively [31, 80, 88, 94, 112, 113, 125–128]. This compound is made of WO_6 octahedra, which as described previously (see Figure 4.4), lead to W_4O_{16} step layers. These step layers are linked to each other across a plane of PO_4 tetrahedra forming layers along the (ab) plane of the unit cell (see Figure 4.1). This junction creates pentagonal tunnels, formed by the corner sharing of the three WO_6 octahedra and two PO_4 tetrahedra. The orthorhombic unit cell parameters are

$a = 5.285$ Å, $b = 6.569$ Å and $c = 17.351$ Å, and the compound crystallizes in the $P2_12_12_1$ space symmetry group [95].

There are two nonequivalent tungsten atoms W^I and W^{II} (see Figure 4.1) in the W_4O_{16} layers of $(PO_2)_4(WO_3)_4(WO_3)_4$. Every W^IO_6 octahedron shares five oxygen atoms with other WO_6 octahedra, while every $W^{II}O_6$ octahedron shares three oxygen atoms with other WO_6 octahedra and three oxygen atoms with PO_4 tetrahedra [115]. The oxidation states calculated by the bond valence sum analysis [129] are for W^I +5.82 and for W^{II} +5.18, and therefore, the average oxidation state of tungsten in $P_4W_8O_{32}$ is +5.5.

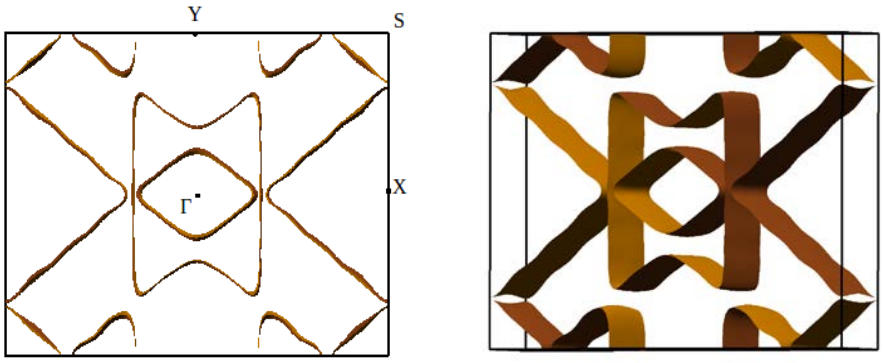

(a) (b)

Fig. 4.11 The Fermi surface of $P_4W_8O_{32}$: (a) projection along the c^* direction, and (b) 3D representation.

In the Figure 4.2 is shown the band structure of $P_4W_8O_{32}$. There are two d electrons per layer, and thus four d electrons per unit cell. The band structure shows that there is one pair of 1D bands and two pairs of 2D bands. The 1D character is due to the apparently very weak interactions (δ type interactions) between the adjacent W_4O_{18} chains along the b axis and strong interaction along the a axis. The calculated Fermi surface of $P_4W_8O_{32}$ is presented in the Figures 4.11a and 4.11b. There are six Fermi surface pairs of sheets coming from the six bands that are crossing the Fermi level. The Fermi surface on the Figures 4.11a and 4.11b is the superposition of these six pairs of sheets. Although the contribution of the apparently 2D bands are closed loops, Figure 4.11 clearly shows that the total Fermi surface is the superposition of three sets of 1D Fermi surfaces. Thus, the Fermi surface has very good nesting conditions because of its "hidden" one-dimensionality.

Two anomalies have been found in electrical resistivity for this compound, indicating the existence of two electronic instabilities. These instabilities are occurring at $T_{p1} = 80K$ and at $T_{p2} = 52K$ [93, 94]. The X-ray diffuse scattering studies have demonstrated that they

are corresponding to the incommensurate charge density waves with the modulation vectors $q_1 = (0.33, 0.295, 0)$ and $q_2 = (0.34, 0, 0)$ [89, 128, 130], respectively.

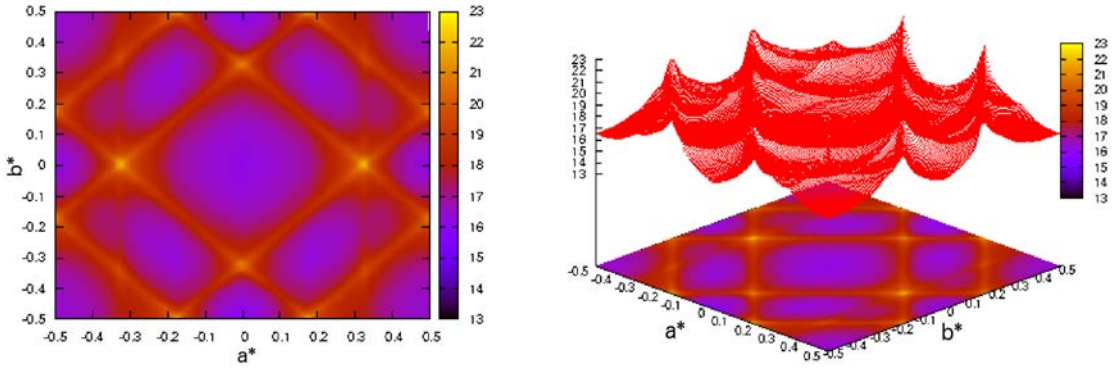

(a) (b)

Fig. 4.12 (a) (a^*, b^*) section and (b) 3D representation of the Lindhard response function for the $m = 4$ member of $MPTB_p$.

The results of the Lindhard response function calculation are presented graphically on the Figures 4.12a and 4.12b and the nesting vectors, which are associated with the maxima are given in the Table 4.1 and compared with the experimental ones [89, 128, 130]. These values are in good agreement with the previous theoretical results by Sandré et al [121] As can be seen in the table, there is a very good agreement between two of the maxima in the Lindhard response function and the experimental determination of the two modulation vectors (i.e., $q_1 \approx Q_5$ and $q_2 \approx Q_1$).

	calculation	experiment
Q_1	$0.325, 0.0, 0.0$	$0.34, 0.0, 0.0$
Q_2	$0.0, 0.325, 0.0$	
Q_3	$0.19, 0.5, 0.0$	
Q_4	$0.5, 0.175, 0.0$	
Q_5	$0.325, 0.35, 0.0$	$0.33, 0.295, 0.0$

Table 4.1 The maxima of Lindhard response function calculation for $P_4W_8O_{32}$.

With this information in mind several scenarios can be proposed to explain the experimental results. First, since the lower temperature transition (i.e. that leading to a smaller stabilization) is associated with a wave vector with approximately $1/3$ component along a^*, the associated modulation should in principle affect either the two chains along $a+b$ and $-a+b$, or the chains along a only. In the first case, the higher temperature transition, associated with a modulation having components approximately $1/3$ along both a^* and b^*

should be associated with the chains along a (scenario I). It may seem surprising to associate a diagonal nesting vector to the destruction of the Fermi surface associated with the chains along a. However, since this Fermi surface is made of two planes perpendicular to the a^* direction, all nesting vectors with an $\sim 1/3a^*$ component and any b^* component will lead to the full destruction of the remaining Fermi surface planes of Figure 4.11 (this is the reason for the existence of diffuse lines perpendicular to a^* for $a^* \sim 0.33$ in Figure 4.12). However it seems surprising that the higher temperature transition, which should be associated with the largest energy gain, affects only one type of chain whereas the second affects two types of chains thus leading in principle to a larger stabilization.

If we now assume that the lower temperature transition is associated with the chains along a, it is not possible to nest the Fermi surfaces of the two types of diagonal chains with a single nesting vector having components approximately $1/3$ along both a^* and b^*. Such a diagonal nesting vector allows the destruction of only one type of diagonal chain. Thus no common nesting vector would be used in this process (scenario II) and at least one-third of the Fermi surface will remain after the two distortions. This is very unlikely since it would be associated with a modest gain in electronic energy.

We can also consider a third scenario in which the high temperature transition would be associated with one of the diagonal chains (either those along $a+b$ or $-a+b$) and those along a. In that case the second transition would be associated with the remaining diagonal chain (scenario III). This scenario would lead to the destruction of the Fermi surface associated with two types of chains in the case of the higher temperature transition and the remaining one in the lower temperature transition so that it is free from the criticism raised for scenario I. One must take into account that by considering the Lindhard response function we do not take into account the elastic energy cost of the different distortions which may become decisive in leading to one or the other structural modulations. However, only from the viewpoint of the Lindhard response function calculation it can thus be proposed that the modulation occurring at 80 K is associated with the chains along a and one of the diagonal chains, and the second modulation occurring at 52 K affects the remaining type of diagonal chains (scenario III). This scenario has the additional advantage over scenario I of being consistent with one important experimental observation. The X-ray diffuse scattering experiments [89, 128, 130] clearly show the occurrence of pretransitional fluctuations in the form of diffuse lines perpendicular to the a direction and to broader diffuse lines perpendicular to the $a+b$ and $-a+b$ directions. In other words, the pretransitional fluctuations affecting the chains along a dominate from room temperature down to the high temperature transition. This means that the instability of the chains along a dominates the regime of fluctuations at

high temperature. Taking into account the experimental and theoretical results we conclude that it must be scenario III which is at work.

In view of all this facts we finally conclude that the high temperature transition is associated with an instability of the chains along a which induce a modulation in both chains along a and one of the two diagonal directions. The lower temperature transition is associated with the remaining diagonal type of chains. After he two transitions, closed pockets associated with hybridization of the three types of Fermi surface hidden planes will remain, keeping the metallic character of the bronze. These closed pockets should be responsible for the Shubnikov-de Haas oscillations observed for this system at temperatures well bellow that of the second transition [84, 85, 112].

Finally, we should inquire what is the physical meaning of the fact that the three types of planes of the Fermi surface intersect the a^* direction at the same point. Noting the occupation of the bands associated with a, $a+b$ and $-a+b$ directions as f_a, f_{a+b} and f_{-a+b} respectively, it must hold that $f_{a+b} = f_{-a+b} = 1/2(1-f_a)$, since the total number of electrons in one layer is 2 and chains along $a+b$ and $-a+b$ are equivalent. An equal occupation of the three bands is only possible when $f_{a+b} = f_{-a+b} = f_a = 1/3$. For a 1D system, as for instance the chains along a, $f_a = 1/3$ means that $q_a = 2k_f = 1/3$. Consequently, as far as the number of electrons is 2, only when the three hidden 1D bands are equally filled (i.e., $f_{a+b} = f_{-a+b} = f_a = 1/3$) the three types of planes of the Fermi surface can intersect the a^* direction at the same point. Consequently, for the $m = 4$ member of the $MPTB_p$ the filling of the three types of bands is the same even if there are two different types of chains.

The previous discussion provides an easy way to discuss the occupation of the two different types of bands of the $MPTB_p$ since for any member of this family it holds that $f_{a+b} = f_{-a+b} = 1/2(1-f_a)$: just looking at the separation between the hidden planes perpendicular to a^* in the Fermi surface the filling of the different bands is known.

4.4.2 $MPTB_p$ with $m = 5$

This compound has been found to exist in two different varieties [89, 96, 102]. The crystal structure of the first type is built of regular stacking of layers corresponding to $m = 5$ [102]. The second type is consisting of two layers with different thickness: $m = 4$ and $m = 6$ [89, 96]. For a long time, the "regular" $2m = 5+5$ structure couldn't be detected, neither by X-ray nor by electronic diffraction. There was a belief that the phase $2m = 4+6$ is the only stable one and the regular one is non-existent. Later on, the $2m = 5+5$ missing crystal variety was successfully identified and investigated.

Here are going to be presented results for the regular structure $2m = 5+5$. The crystal structure of this $MPTB_p$ member is monoclinic and is built up of a regular stacking of layers

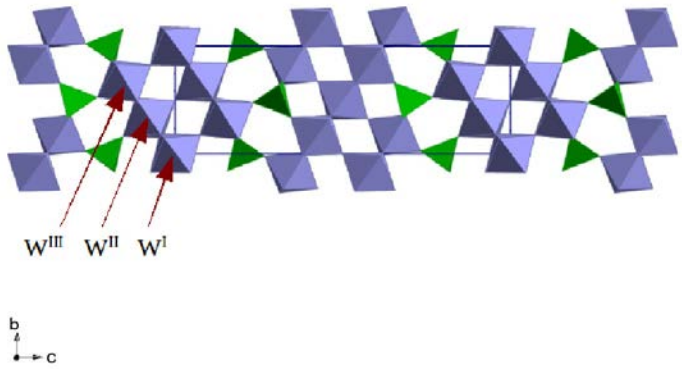

Fig. 4.13 View of the crystal structure of the $P_4W_{10}O_{38}$ $MPTB_p$ ($m = 5$) along the a axis.

corresponding to $m = 5$. Five WO_6 octahedra are forming the W_5O_{26} units which are joining to form W_5O_{22} chains which are running along a and $a \pm b$ crystallographic directions. These chains are further condensed to produce W_5O_{19} step layers, of which are two in the unit cell of $P_4W_{10}O_{38}$, Figure 4.13. The unit cell parameters are $a = 5.283$ Å, $b = 6.567$ Å , $c = 20.451$ Å and $\beta = 90.40°$, and the compound crystallizes in the monoclinic $P2_1/n$ space symmetry group [102]. The synthesised crystals of $2m = 5+5$ member are blue-purple with golden edges, while those of the $m = 4$ member they are purple.

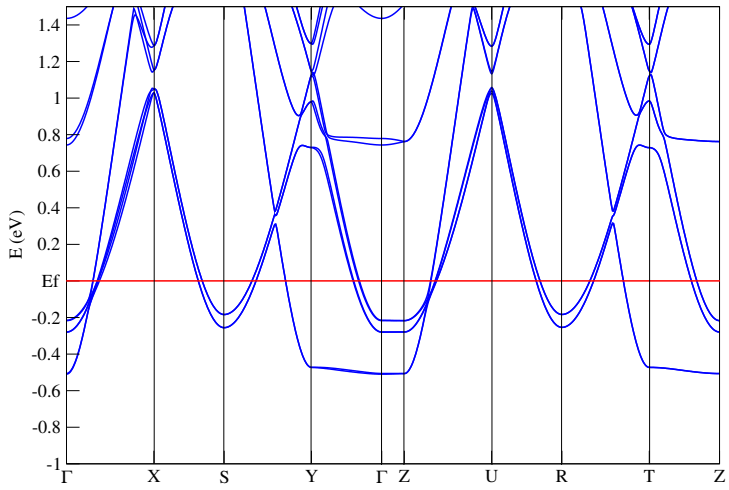

Fig. 4.14 Calculated band structure of $P_4W_{10}O_{38}$.

On the Figure 4.14 is presented the band structure of this $MPTB_p$ member. As expected, it is very similar to the band structure of the $m = 4$ member. There are six bands crossing the Fermi level with practically no dispersion along c^* and thus, making in that way three pairs of bands, like in the case of $m = 4$. One pair of bands has 1D character and is not dispersive along Γ-Y direction but shows dispersion along Γ-X. The other two pairs of bands apparently have 2D character and come from the chains of interactions along the $a^* + b^*$ and $-a^* + b^*$ directions.

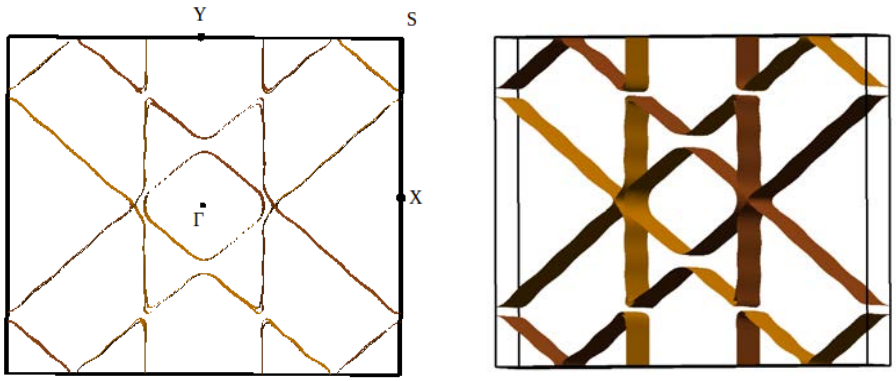

(a) (b)

Fig. 4.15 The Fermi surface of $P_4W_{10}O_{38}$: (a) projection along the c^* direction; (b) 3D representation.

On the Figure 4.15 is presented the calculated Fermi surface of $P_4W_{10}O_{38}$. Again, it is a superposition of six pairs of Fermi surface sheets which are representing the contribution of six bands crossing the Fermi level (Figure 4.14). The Fermi surface of the $m = 5$ member looks very much like the Fermi surface of the $m = 4$ member although the filling of the three pairs of bands is somewhat different. As shown in Figure 4.15a, $f_a = 2k_{f_a} = 0.30$, i.e., a 10% smaller than for the $m = 4$ member, and thus, $f_{a+b} = f_{-a+b} = 0.35$. Consequently, the 1D bands along a are filled with 0.6 electrons whereas each of those along $a + b$ and $-a + b$ are filled with 0.7 electrons. On the Figures 4.16a and 4.16b are presented the results of the Lindhard response function calculation for this compound.

The $P_4W_{10}O_{38}$ shows two successive Peierls transitions at $T_{p1} = 83K$ and at $T_{p2} = 60K$ [131]. although only the latter is detected in transport measurements [114]. Two sets of diffuse lines parallel to the $a^* \pm b^*$ directions are already present at room temperature in the diffuse X-ray scattering measurements [131]. The fluctuations associated with these diffuse lines diverge, leading to satellite reflections at the $q_a = (0.32, 0.29, 0)$ wave vector below 83 K. Lowering the temperature, below the 60 K, a second set of satellite reflections at the $q_b = (0.36, 0, 0)$ wave vector appear [102, 131].

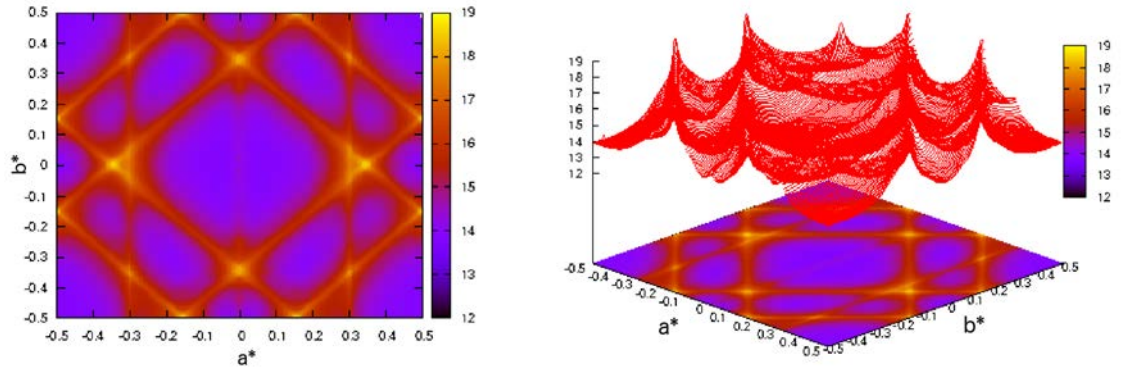

(a) (b)

Fig. 4.16 (a^*, b^*) section of the Lindhard response function for the $m = 5$ member of the $MPTB_p$.

The nesting vectors associated with the maxima of the Lindhard response function as well as the experimentally determined modulation vectors for this bronze are shown in Table 4.2. The calculated nesting vectors Q_1 and Q_5 are in a good agreement with the superlattice reflections occurring at 60 K and 83 K, respectively. Thus, we conclude that these modulations are Fermi surface driven CDWs.

	calculation	experiment
Q_1	$0.345, 0.00, 0.0$	$0.36, 0.0, 0.0$
Q_2	$0.00, 0.345, 0.0$	
Q_3	$0.16, 0.50, 0.0$	
Q_4	$0.50, 0.15, 0.0$	
Q_5	$0.30, 0.355, 0.0$	$0.32, 0.29, 0.0$
Q_6	$0.30, 0.04, 0.0$	

Table 4.2 The maxima of Lindhard response function calculation for $P_4W_{10}O_{38}$.

Note that five of the six maxima in Table 4.2 are very similar to those for the $m = 4$ member of the series (Table 4.1). However, in the present case there is one additional maxima. The reason is that as analysed above, the filling of the three bands of a layer is not the same. As a result, the vertical and "diagonal" planes of the Fermi surface do not cross at the same point of the a^* axis. Consequently, what was a single maxima in the Lindhard response function of the $m = 4$ member becomes three maxima (two of which are symmetry related) in that of the $m = 5$ member. Consequently, the discussion concerning the relationship between the observed modulations and the Lindhard response function results for the $m = 4$ member does not directly apply to the present member.

The good agreement between the low temperature modulation and the q_1 nesting vector suggests that this modulation affects the chains along the $a+b$ and $-a+b$ directions. On the other hand, the quite reasonable agreement between the high temperature modulation and the Q_5 nesting vector suggests that this modulation affects both the chains along a and one of the diagonal directions. Thus, we believe that the high temperature transition is associated with the destruction of the hidden planes of the Fermi surface associated with the chains along a and $a+b$ (or $-a+b$) whereas the low temperature transition is associated with the destruction of the hidden planes associated with the other diagonal plane, $-a+b$ (or $a+b$). The situation is thus similar to that of the $m=4$ member of the series but with one important difference: at high temperatures only the diagonal chains exhibit pretransitional fluctuations. Thus, the high temperature transition is associated with both the chains along a and one diagonal direction but is induced by the instability in the diagonal chains. After the two transitions, closed pockets associated with the hybridization of the three types of the Fermi surface hidden planes will remain, keeping the metallic character of the bronze [102, 131].

The previous results point to a drop of the influence of the instability in the chains along a when going from the member $m=4$ to $m=5$ of the series since the pretransitional fluctuations in these chains are not observed at high temperatures for the $MPTB_p$ with $m=5$ [131]. This is consistent with the decrease of the population of the 1D band along a, ($\sim 10\%$), when going from the $m=4$ to $m=5$ members, as can be deduced from the Fermi surfaces of Figures 4.11a and 4.15a.

4.4.3 $MPTB_p$ with $m=6$

The $m=6$ member of $MPTB_p$ series (see Figure 4.17) has been studied extensively [89, 93, 112, 113, 116, 122, 132–134]. This compound is isostructural with $\gamma-Mo_4O_{11}$, with PO_4 tetrahedra replacing the MoO_4 tetrahedra and WO_6 octahedra replacing the MoO_6 octahedra [106–109]. The W_6O_{22} step layers of $P_4W_{12}O_{44}$ are built up of W_6O_{26} chains, which are condensed by (13)-condensation [97]. This compound is orthorhombic and the cell vectors are $a=5.29$Å, $b=6.57$Å and $c=23.55$Å. It has the same space group symmetry as the $m=4$ compound: $P2_12_12_1$. The crystals of $P_4W_{12}O_{44}$ are dark blue.

There are three types of W atoms with different oxidation number: W^I with $+5.54$, W^{II} with $+5.67$ and W^{III} with $+5.79$. The average oxidation number of tungsten atoms is $+5.67$. On the Figure 4.18 is represented the band structure of $P_4W_{12}O_{44}$. As in the previous cases of $MPTB_p$ series, the band structure consists of six bands that are crossing the Fermi level. As for the $m=5$ member, the interaction between step layers is very small. The calculated Fermi surface for $P_4W_{12}O_{44}$ is shown on the Figures 4.19a and 4.19b. From this figure we can estimate the filling of the different 1D bands. Since $2k_{f_a}=0.27$, it follows that $f_a=0.27$,

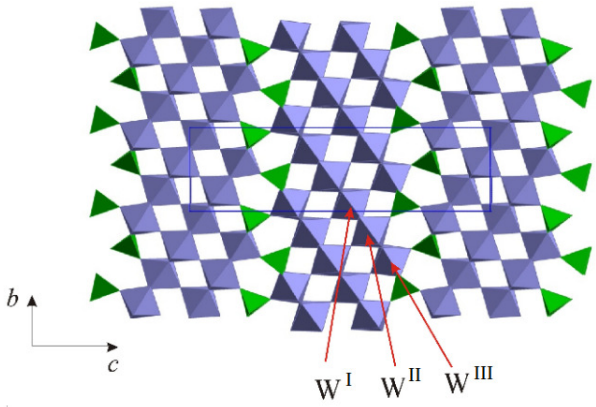

Fig. 4.17 View of the crystal structure of the $P_4W_{12}O_{44}$ $MPTB_p$ ($m = 6$) along the a axis.

$f_{a+b} = f_{-a+b} = 0.365$. Consequently, the 1D band along a contains 0.54 electrons and each of the 1D bands along the diagonal direction contain 0.73 electrons. Again, we find that increasing m leads to depletion of the 1D band along a.

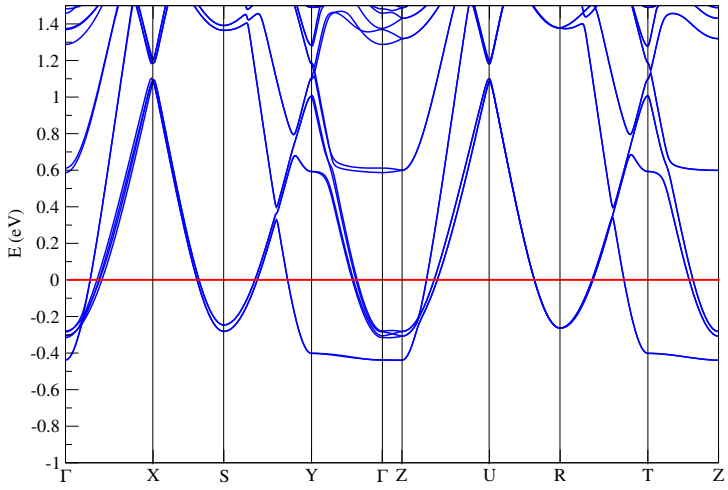

Fig. 4.18 Calculated band structure of $P_4W_{12}O_{44}$.

This member shows three Peierls instabilities: at $T_{p1} = 120$K, $T_{p2} = 62$K and $T_{p3} = 30$K and the experimentally determined critical wavevectors are $q_1 = (0.385, 0, ?)$, $q_2 = (0.31, 0.295, ?)$ and $q_3 = (0.29, 0.11, ?)$ respectively [88, 130, 134]. They correspond to metal-to-metal transitions. Note that already at room temperature this metal exhibits 1D fluctuations parallel to the $a^* + b^*$ and $-a^* + b^*$ directions [134]. The results of Lindhard

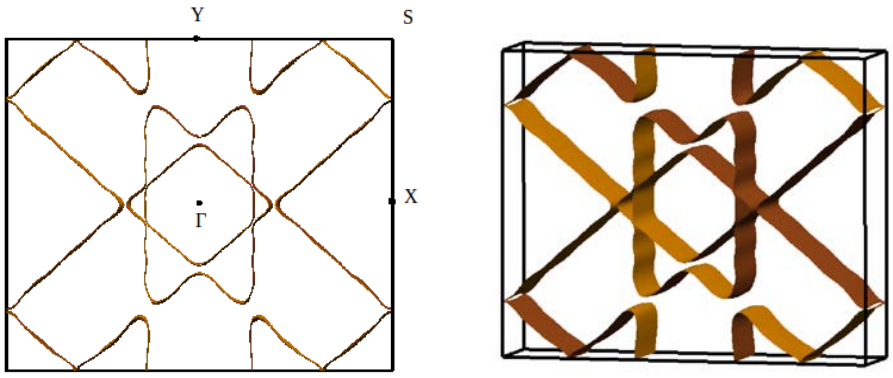

(a) (b)

Fig. 4.19 The Fermi surface of $P_4W_{12}O_{44}$: (a) projection along the c^* direction; (b) 3D representation.

response function calculation are given on the Figures 4.20a and 4.20b. The quantum transport measurements show that the size of carrier pocket that remains after CDW gap opening is much smaller in $m = 6$ than in the $m = 4$ compound [112]. This may indicate larger Fermi surface nesting for the $m = 6$ compound and therefore bigger Fermi surface destruction after the CDW transition.

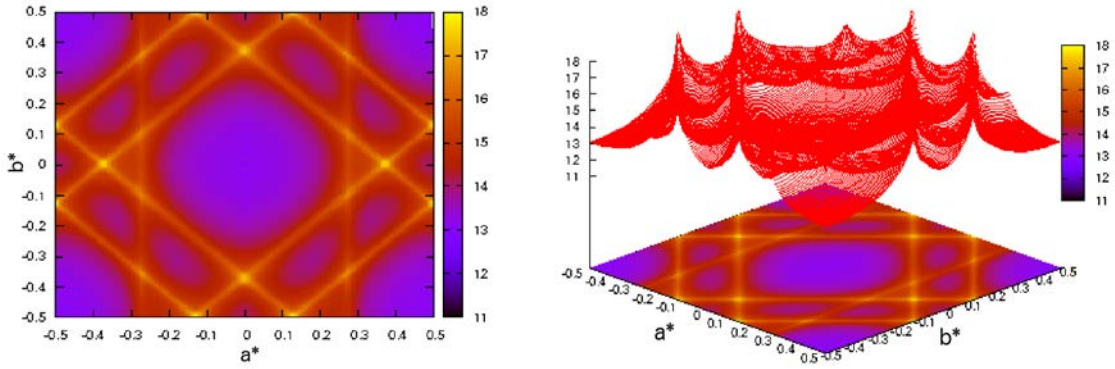

(a) (b)

Fig. 4.20 (a^*, b^*) section of the Lindhard response function calculated for $P_4W_{12}O_{44}$.

In the table 4.3 are shown the nesting vectors associated with the maxima of the calculated Lindhard response function as well as the experimental modulation vectors [88, 130, 134]. We find that the vectors Q_4 and Q_6 are in very good agreement with the first and third experimentally found transitions and that the Q_5 nesting vector does not considerably differ from the second measured one. Again we conclude that these modulations are Fermi surface driven CDWs. One must also take into account that after the first modulation the Fermi

surface is slightly modified because of the structural change. Thus, the agreement between the calculated and experimental modulation vectors should slightly deteriorate.

Note that five of the six maxima in Table 4.3 are very similar to those for the $m = 5$ member of the series (Table 4.2); the numerical differences can be understood from the different filling of the bands noted before. The increase of the population of the 1D bands along the diagonal directions is clearly visible when comparing Figures 4.19a, 4.15a and 4.11a: the separation between the intersections of the Fermi surface planes along the diagonal directions and those perpendicular to a increases when m increases.

	calculation	experiment
Q_1	$0.13, 0.50, 0.0$	
Q_2	$0.50, 0.125, 0.0$	
Q_3	$0.0, 0.37, 0.0$	
Q_4	$0.375, 0.00, 0.0$	$0.385, 0.001, ?$
Q_5	$0.27, 0.36, 0.0$	$0.31, 0.295, ?$
Q_6	$0.27, 0.10, 0.0$	$0.29, 0.11, ?$

Table 4.3 The maxima of Lindhard response function calculation for $P_4W_{12}O_{44}$.

On the basis of our discussion for the $m = 5$ member and the good agreement between the 120 K modulation and the Q_4 nesting vector suggests that the modulation affects the chains along the $a+b$ and $-a+b$ directions. On the other hand, the quite reasonable agreement between the 62 K and ~ 30 K modulations and the q_5 and q_6 nesting vectors suggests that these modulations successfully destroy the Fermi surface planes associated with the 1D bands along a. Note that the high temperature transition for the $m = 6$ corresponds to the low temperature transition for the $m = 5$ according to the experimental modulation vectors. On the basis of our calculations we propose that the high temperature modulation is associated with the two 1D chains along the diagonal directions. Since the high temperature transition should be associated with the larger energy gain, this observation is consistent with the fact that the diagonal bands are more filled in the present compound and the well-known fact that the maximum stabilization for a Peierls like distortion in a 1D system is maximum at half filling. The absence of pretransitional fluctuations perpendicular to a^* and the fact that the 62 K transition seems to be associated with the nesting vector common to the Fermi surface planes perpendicular to a and one of the diagonal directions means that the modulation in the chains along a is induced by the instability of the diagonal chains. Again this is consistent with the noted depletion of the 1D bands along a in the $m = 6$ member with respect to the $m = 5$ one. The nesting vector associated with the ~ 30 K modulation, perfectly nests the regions of the crossing of the Fermi surface planes perpendicular to a and the diagonal

ones in the region near the a-axis. This means that the third transition is most likely due to coupling of the closed pockets generated in this region after the second modulation. That this modulation does not occur in the lower members of the series is consistent with the observation that the carrier pockets remaining after the different CDWs are smaller in the present compound.

4.4.4 $MPTB_p$ with $m = 7$

This odd member of $MPTB_p$ family has peculiar transport properties and doesn't show "classical" CDW transitions, as the other $MPTB_p$ members [128, 130, 134]. The purple crystals of $P_4W_{14}O_{50}$ are monoclinic with the space group $P2_1/n$ and cell vectors $a = 5.291$ Å, $b = 6.557$ Å and $c = 26.654$ Å and $\beta = 90.19°$. The detailed structure analysis [104] reveals that $m = 7$ member has exactly the same structure with successive slabs of the same width as all the even members of the series (Figure 4.21). The structure analysis show that $P_4W_{14}O_{50}$ crystallizes in centrosymmetric group, which is an unique characteristics among odd $MPTB_p$ members.

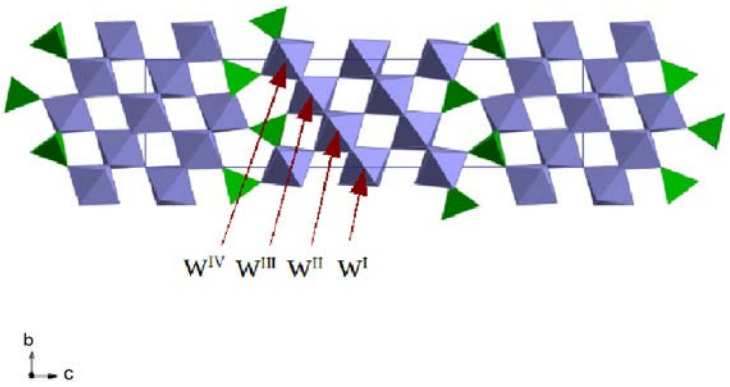

Fig. 4.21 Crystal structure of the $P_4W_{14}O_{50}$.

There are four types of tungsten atoms in $P_4W_{14}O_{50}$ with different oxidation states: $+5.58$ for W^I, $+5.68$ for W^{II}, $+5.75$ for W^{III} and $+5.85$ for W^{IV} so that the average oxidation state of W atoms in the layer is $+5.71$ [104]. The formal valence state of W atoms decreases as the distance from the PO_4 tetrahedra increases. Therefore the W atoms in the middle of the slab are going to have the lowest oxidation number and the ones on the edges the highest.

On the Figure 4.22 is shown the calculated band structure for this member. As for the other members of $MPTB_p$ series, $P_4W_{14}O_{50}$ shows six bands crossing the Fermi level. The features of this six bands are the same for all $MPTB_p$s.

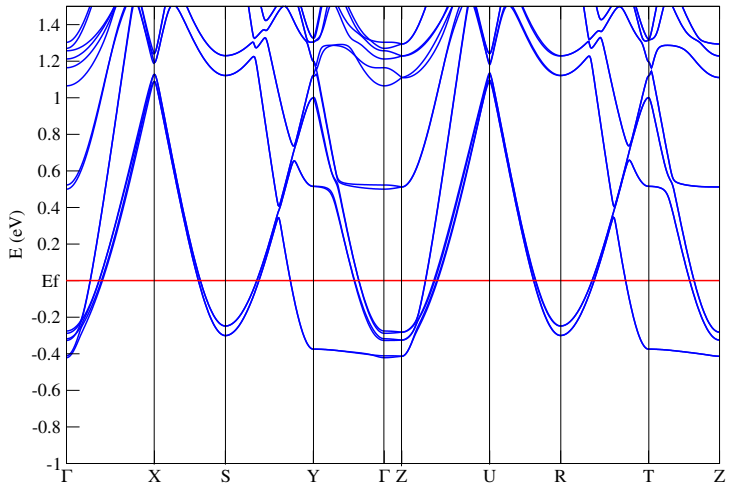

Fig. 4.22 Calculated band structure of $P_4W_{14}O_{50}$.

The calculated Fermi surface is shown in Figure 4.23. It shows, as for the other $MPTB_p$ members, that the global Fermi surface has hidden one-dimensionality with hidden 1D sheets along directions which are perpendicular to a^* and $a^* \pm b^*$ directions. Therefore, similar nesting vectors are expected as in the other $MPTB_p$ members. From this figure the filling of the different bands can be estimated as: $f_a = 0.26$, $f_{a+b} = f_{-a+b} = 0.37$. Consequently, the 1D band along a contains 0.52 electrons and those along the diagonal directions contain 0.74 electrons each. Again, the 1D band along a is depleted with respect to these of the lower m members.

Electrical resistivity data and X-ray diffuse scattering studies have shown the existence of two transitions, at $T_{p1} = 188$ K and at $T_{p2} = 60$ K [80, 88, 128, 130, 134]. There have been found several harmonics of the CDW satellite wavevectors for both transitions. This compound is the only member of the $MPTB_p$ series showing superconducting properties (below 0.3 K) [117].

In the Figures 4.24a and 4.24b are represented the results of Lindhard response function calculation and in the Table 4.4 the calculated nesting vectors, extracted from the Figures 4.24a and 4.24b and compared with the experimental data [128, 134].

The six maxima of the Lindhard response function reported in Table 4.4 are very similar to those of the $m = 5$ and $m = 6$ members of the series (Tables 4.2 and 4.3) with the small differences being the result of the different electron fillings of the three pairs of 1D bands. However, when these bands are compared with the observed modulation wave vectors (Table

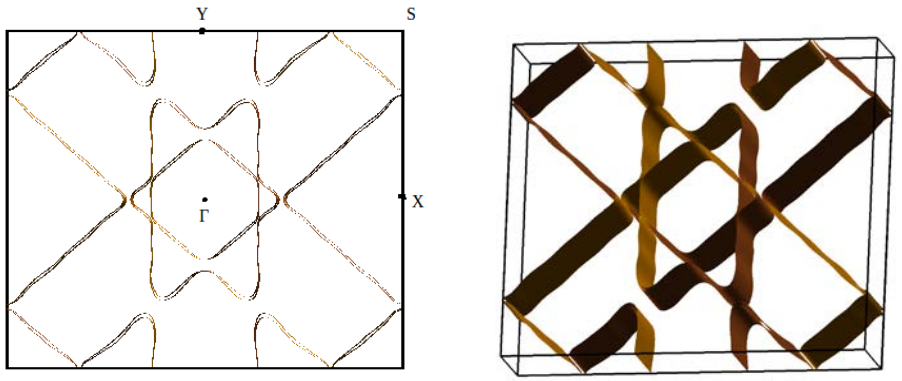

(a) (b)

Fig. 4.23 The Fermi surface of $P_4W_{14}O_{50}$: (a) projection along the c^* direction; (b) 3D representation.

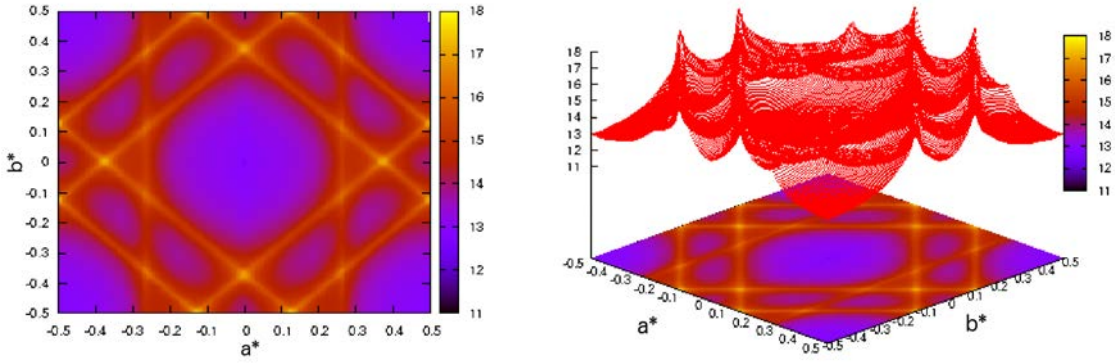

(a) (b)

Fig. 4.24 (a^*,b^*) section of the Lindhard response function calculated for $P_4W_{14}O_{50}$.

4.4) we face a different situation than that described for the lower m members. In that case, only one of the observed wave vectors, that corresponding to the high temperature modulation ($q = (0.26, 0.073, 0.27)$) can be compared with one of the calculated ones ($Q_6 = (0.26, 0.12, 0)$). Let us point that the experimental wave vector contains one component along c^*. From the viewpoint of the electronic structure this point is irrelevant since as it is clear from the band structure there is no interaction between the step layers so that the nesting is equally good for any value of the c^* component. This component along the interlayer direction must be due to either strain or purely coulombic interactions between modulations.

The Q_6 nesting vector provides an excellent overlap of the Fermi surface planes associated with the 1D diagonal chains. In addition, the X-ray diffuse scattering study showed that pretransitional fluctuations parallel to the $a^* + b^*$ and $-a^* + b^*$ directions occur since 300 K until the 188 K transition [134]. In view of the results of Figure 4.24 we conclude that the

	calculation	experiment
Q_1	$0.125, 0.50, 0.0$	
Q_2	$0.50, 0.125, 0.0$	
Q_3	$0.00, 0.375, 0.0$	
Q_4	$0.37, 0.0, 0.0$	
Q_5	$0.26, 0.365, 0.0$	
Q_6	$0.26, 0.12, 0.0$	$0.26, 0.073, 0.27$
		$0.12, 0.03, 0.15$

Table 4.4 The maxima of Lindhard response function calculation for $P_4W_{14}O_{50}$.

188 K transition in the present $MPTB_p$ is due to Fermi surface nesting driven CDW in the diagonal chains but affects one of the diagonal chains and those along a. Since it will be of importance later, let us note that the transition exhibits a large series of harmonics (up to six), something very unusual for traditional Peierls distortions, which suggests a non sinusoidal character of the modulation.

The second modulation occurring at 60 K does not coincide with any of the nesting vectors leading to maxima of the Lindhard response function. This fact is not due to inadequacy of the calculated Fermi surface. Since the first modulation coincides very well with the nesting vector associated with the Fermi surface diagonal and vertical (i.e. perpendicular to a) planes, it is not possible that the a^* component of the nesting vector associated with the 1D chains along a^* can be much different from the calculated value of $0.26a^*$ if the modulation is Fermi surface driven. This value is, however, twice larger than the a^* component of the modulation wave vector occurring at 60 K ($0.12a^*$). Consequently, the 60 K transition cannot be associated with a Fermi surface driven CDW. This conclusion is confirmed by the fact that this transition is not associated with pretransitional diffuse lines but with very isotropic fluctuations in the (a^*, b^*) plane. Let us note also that several harmonics have also been detected in that case [128, 130, 134].

4.4.5 $MPTB_p$ with $m = 8$

This even m member of $MPTB_p$ series is well studied along with the $m = 4$ and 6 even m members. Dark blue crystals of $P_4W_{16}O_{56}$ are built up in the same fashion as the crystals of $m = 4$ and 6. The W_8O_{34} chains are condensed together to make W_8O_{28} layers of which there are two in the unit cell, Figure 4.25. This compound is orthorhombic with the space group $P2_12_12_1$ and cell vectors are $a = 5.29$ Å, $b = 6.55$ Å and $c = 26.7$ Å [97].

There are four types of tungsten atoms with the different oxidation numbers in $P_4W_{16}O_{56}$: W^I with $+5.73$, W^{II} with $+5.71$, W^{III} has $+5.76$ and W^{IV} $+5.81$, and the average oxidation

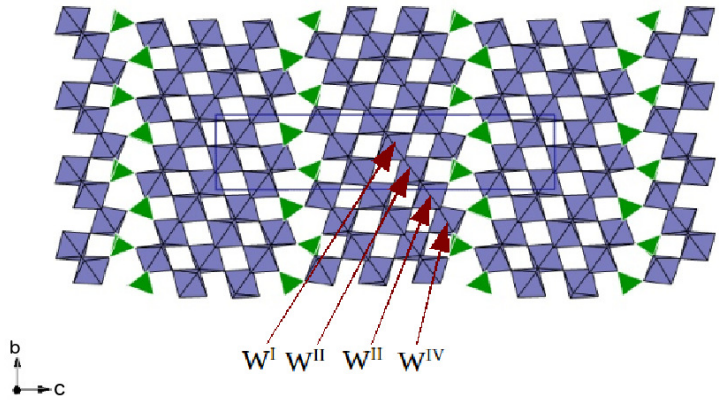

Fig. 4.25 Crystal structure of the $P_4W_{16}O_{56}$.

state of W atoms in the layer is +5.75. On the Figure 4.26 is shown the calculated electronic band structure for $P_4W_{16}O_{56}$. As well, it consists of six bands that are crossing the Fermi level and practically making three pairs of bands without any splitting due to interlayer interactions.

Figures 4.27a and 4.27b show the calculated Fermi surface of $P_4W_{16}O_{56}$. It shows that there are hidden one dimensional sheets along directions which are perpendicular to a^* and $a^* \pm b^*$ directions, as for all the other $MPTB_p$ members. The calculated value for f_a is 0.25 and consequently, $f_{a+b} = f_{-a+b} = 0.375$. The occupation of the 1D band along a is thus 0.5 electrons and that of the bands along the diagonal directions is 0.75 electrons.

This compound shows two very close CDW transitions at $T_{p1} \sim 220$ K and $T_{p2} \sim 200$ K [90] associated with $q_1 = (0.47, 0.02, 0.15)$ and $q_2 = (0.19, 0.03, 0.06)$ structural modulations, respectively [128]. This is the only member of the series which shows no long range order in the CDW state. At high temperature this compound is metallic, which can be attributed to the undistorted Fermi surface in the normal state. The resistivity measurements show semiconducting behaviour and enormous anisotropy along the c direction [91].

On the Figures 4.28a and 4.28b are presented the results of Lindhard response function calculation for $P_4W_{16}O_{56}$.

The nesting vectors in Table 4.5 are very similar to those of the $m = 7$ member (Table 4.4) and also to those of the $m = 6$ member (Table 4.3). This is understandable because the crystal structure and thus the band structures are very similar. The different occupation of the bands follows a depletion of the 1D band along a and consequently, an increase of the population of the 1D bands associated with the diagonal chains when m increases. However, the differences in band occupation are every time smaller as m increases. Thus, it is normal that the Fermi surface and Lindhard response functions of $m = 7$ and $m = 8$ $MPTB_p$ are very similar. However, the two experimental wave vectors of modulations are not in agreement

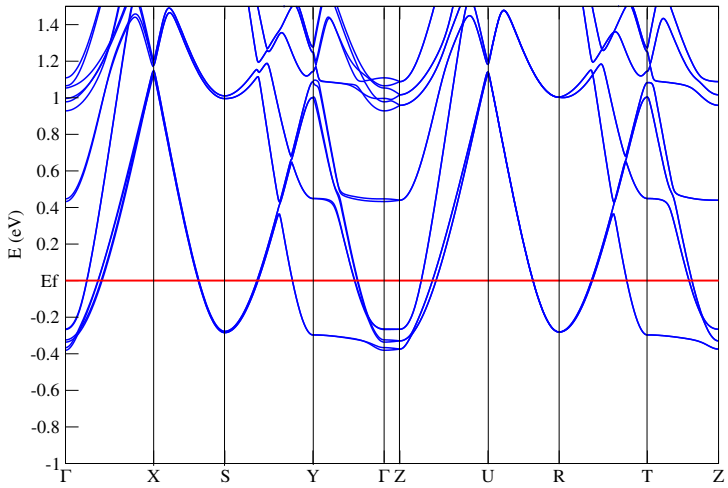

Fig. 4.26 Calculated band structure of $P_4W_{16}O_{56}$.

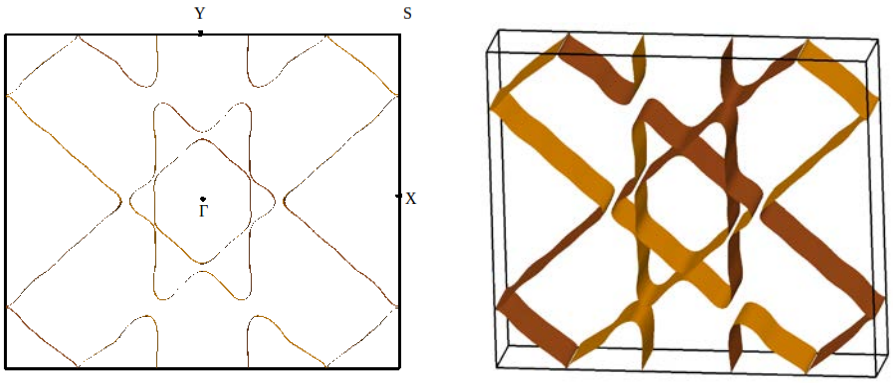

(a) (b)

Fig. 4.27 The Fermi surface of $P_4W_{16}O_{56}$: (a) projection along the c^* direction; (b) 3D presentation.

with the calculated ones. One of the two, $q_2 = (0.19, 0.03, 0.06)$, is strongly related with the modulation that we concluded that is not originating from the Fermi surface instability for the $m = 7$ member and thus, it has probably the same origin in the present system. The other modulation, $q_1 = (0.47, 0.02, 0.15)$, is not at all related with the wave vector of the modulation that is shown to be due to a Fermi surface nesting driven mechanism for the $MPTB_p$ with $m = 7$. We thus conclude that none of the two modulations in the $m = 8$ member of the $MPTB_p$ are due to an instability of the Fermi surface. We note that the second

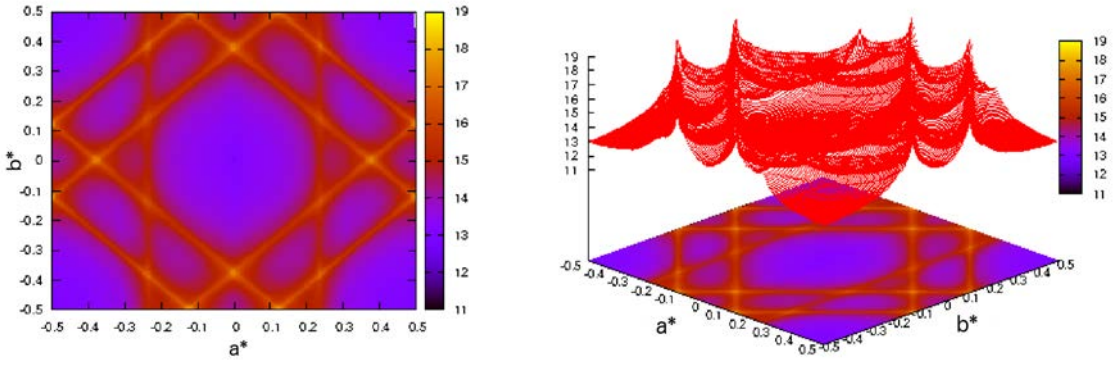

(a) (b)

Fig. 4.28 (a^*, b^*) section of the Lindhard response function calculated for $P_4W_{16}O_{56}$.

modulation has an a^* component very near the commensurate 0.5 value. Thus it seams that there is a net progression from Fermi surface driven to non Fermi surface driven as m increases with coexistence of the two mechanisms for the $m = 7$ member. Let us remark that there is no long range order of the modulations in the $m = 8$ compound [128].

	calculation	experiment
Q_1	$0.125, 0.5, 0.0$	
Q_2	$0.5, 0.125, 0.0$	
Q_3	$0.0, 0.375, 0.0$	
Q_4	$0.37, 0.0, 0.0$	
Q_5	$0.235, 0.39, 0.0$	
Q_6	$0.235, 0.14, 0.0$	
		$0.47, 0.02, 0.15$
		$0.19, 0.03, 0.06$

Table 4.5 The maxima of Lindhard response function calculation for $P_4W_{16}O_{56}$.

4.4.6 $MPTB_p$ with $m = 12$

The $m = 12$ member of $MPTB_p$ series belongs to the larger m members ($8 \leq m \leq 14$) which show commensurate and incommensurate modulations at high transition temperatures, $T > 500$ K [79]. The crystal structure contains $W_{12}O_{40}$ step layers and is shown in Figure 4.29. From the structural viewpoint this bronze is similar to the low m members of the series. Plate-like blue crystals of $P_4W_{24}O_{80}$ are orthorhombic with the cell vectors $a = 5.31$ Å, $b = 6.55$ Å and $c = 42.196$ Å and space group $P2_12_12_1$ [105].

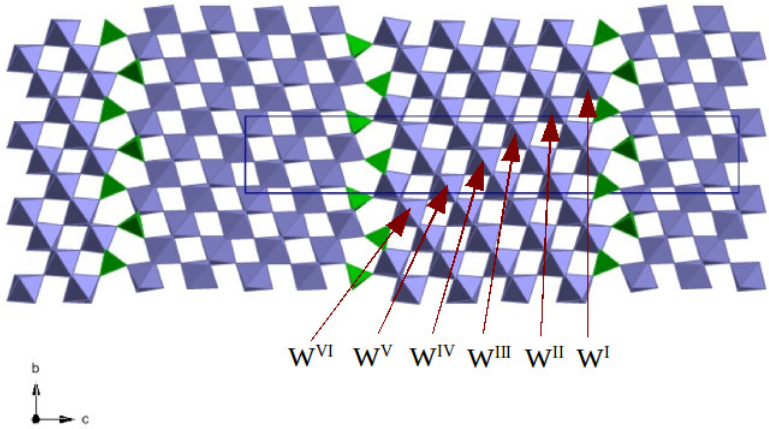

Fig. 4.29 Crystal structure of the $P_4W_{24}O_{80}$.

On the Figure 4.30 is shown the calculated electronic band structure for $P_4W_{24}O_{80}$ which exhibits the same features as all the other $MPTB_p$. Note again, an almost nil interaction between step layers. The Fermi surface (Figure 4.31) shows hidden one-dimensionality as in all other $MPTB_p$. The value of f_a is 0.23 and consequently, $f_{a+b} = f_{-a+b} = 0.385$. The numbers of electrons filling the 1D band along a is 0.46 whereas that in the 1D bands along the diagonal directions is 0.77.

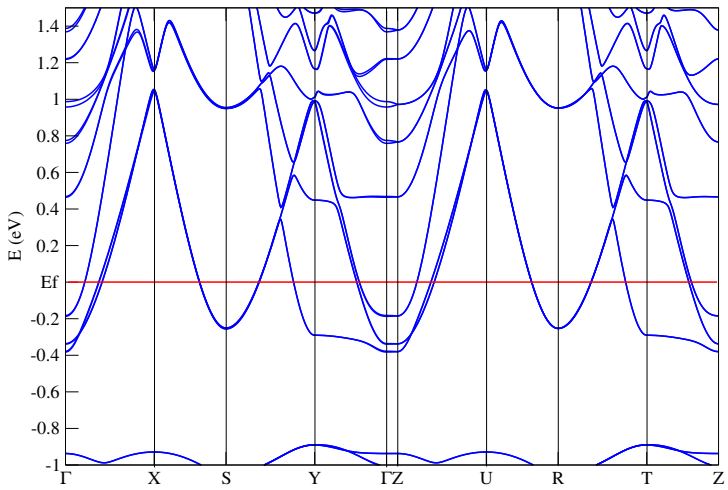

Fig. 4.30 Calculated band structure of $P_4W_{24}O_{80}$.

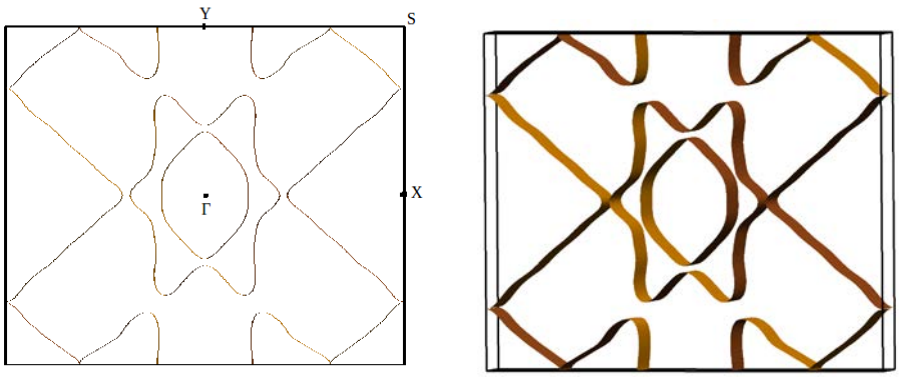

(a) (b)

Fig. 4.31 The Fermi surface of $P_4W_{24}O_{80}$: (a) projection along the c^* direction; (b) 3D representation.

On the Figures 4.32a and 4.32b are shown results of the calculated Lindhard response function. The maxima of the Lindhard response function are shown in Table 4.6. The shape of this Lindhard response function is similar to those of the low m members of the series.

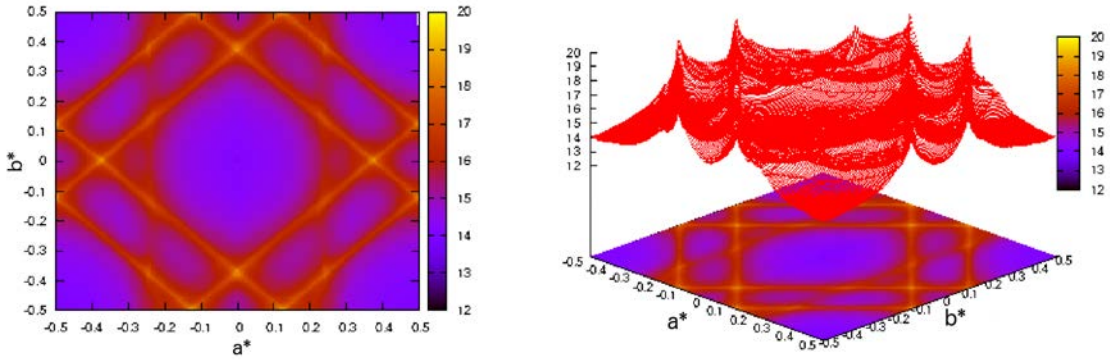

(a) (b)

Fig. 4.32 (a^*,b^*) section of the Lindhard response function calculated for $P_4W_{24}O_{80}$.

The $m = 12$ member shows two instabilities at $T_{p1} = 535K$ and $T_{p2} = 500K$ with the modulation vectors $q_1 = (0.12,0,0)$ and $q_2 = (0.5,0,0.5)$ respectively [79, 128]. Single crystal X-ray diffraction patterns show commensurate modulation wavevectors which correspond to the structural transitions [128].

Shown in Table 4.6 are listed the maxima of the Lindhard response function for the $m = 12$ member. Again and for the same reasons explained before, these values are very similar to those of the $m = 7$ and $m = 8$ members. The two experimentally observed modulations do not coincide with the theoretical values expected for Fermi surface nesting driven modulations.

	calculation	experiment
Q_1	$0.135, 0.5, 0.0$	
Q_2	$0.5, 0.125, 0.0$	
Q_3	$0.0, 0.375, 0.0$	
Q_4	$0.37, 0.0, 0.0$	
Q_5	$0.24, 0.12, 0.0$	
Q_6	$0.24, 0.38, 0.0$	
		$0.5, 0.0, 0.5$
		$0.12, 0.0, 0.0$

Table 4.6 The maxima of Lindhard response function calculation for $P_4W_{24}O_{80}$.

One of the two modulations ($q_1 \sim (0.12, 0.0, 0.0)$) is strongly related with one of those occurring in the $m = 8$ ($q \sim (0.19, 0.03, 0.06)$) and $m = 7$ members ($q \sim (0.12, 0.03, 0.15)$), and which we have attributed to non Fermi surface driven mechanisms. The other modulation has two commensurate components, a^* and c^* of 0.5, almost the same as the a^* component of the second modulation occurring in the $m = 8$ member. The presence of 0.5 commensurate components along both a^* and c^* strongly suggests that this modulation is related to the well known antiferroelectric distortion of pure WO_3, which is not a Fermi surface driven instability. This is not that surprising since the WO_3 is the $m = \infty$ limit of the series and for the large m members of the series, we should expect the same type of instabilities as for WO_3. Thus we conclude that in this $MPTB_p$, like all high m members of the series, the observed modulations do not find their origin in instabilities of the Fermi surface.

4.5 Conclusion

The $MPTB_p$ are low dimensional bronzes with a peculiar electronic structure made of the superposition of 1D bands even if the crystal structure is 3D. The crystal structure contains W-O step layers of different width depending on the number of octahedra (m) condensed to give the elementary repeat unit of the layer. Because of the low electron filling of the t_{2g} block bands of this family of bronzes, the Fermi surface results from the superposition of planes perpendicular to the a^*, $a^* + b^*$ and $-a^* + b^*$ directions of the Brillouin zone. Calculation of the band structure, Fermi surface and Lindhard response function for a series of $MPTB_p$ for values of $m = 4, 5, 6, 7, 8$ and 12 has led to the following conclusions:

- The Lindhard response function for all the $MPTB_p$s that we have studied ($m = 4, 5, 6, 7, 8, 12$) except for the $m = 4$ case, contains six different maxima which are associated with common nesting vectors for two of the three different 1D partially

filled bands of these bronzes. For the $m = 4$ member, there are only five as a result of the fact that the three 1D bands are equally filled. Only three of these common nesting vectors seem to be relevant to explain the electronic instabilities of the low m members of the series.

- The electronic filling of the bands associated with the 1D chains along a and the diagonal directions changes along the series. The three bands are equally filled for $m = 4$ (0.66 electrons) and then the 1D band along a is progressively depleted down to 0.46 electrons for $m = 12$, while each of the 1D bands along the diagonal direction are increasingly populated up to 0.77 electrons for $m = 12$.

- The structural modulations occurring in the low members of the series $m = 4, 5$ and 6 originate from Fermi surface driven CDWs of the step layers. For the high m members of the series $m = 8, 12$, the structural modulations (which exhibit many harmonics) are due to non Fermi surface related mechanisms which are most likely related to the antiferroelectric instability of WO_3 or to antiferrodistortive transitions related to the different types of rotations of WO_6 octahedra in that phase. The $m = 7$ phase is a borderline compound where one of the modulations originates from the Fermi surface instability whereas the other is unrelated to the Fermi surface. Thus, the rich physical and structural behaviour of this phase is due to the competition between CDWs resulting from the nesting of the Fermi surface and antiferrodistortive distortions of the octahedral lattice.

- Among the low m members of this family the nature of the modulations change according to the filling of the different 1D bands. For $m = 4$ the higher temperature modulation originates from the instability of the 1D chains along a coupled with the instability of one of the diagonal chains whereas the low temperature transition originates from the instability of the other 1D chain along the diagonal directions. For $m = 5$ the high temperature transition is still associated with the destruction of the hidden planes of the Fermi surface associated with the chains along a and one of the diagonal directions although the 1D chain along a does not play anymore the leading role. For $m = 6$ the high temperature modulation is associated with the instability of the chains associated with the diagonal directions and the low temperature one, with the instability of the chains along a. Thus, there is a progressive decrease of the influence of the chains along a in imposing the kind of CDWs in these low m $MPTB_p$, which can be easily related to the decreased filling of the band associated with the chains along a. The high temperature modulation of the $m = 7$ member is due to the instability of one of the diagonal chains coupled with the instability of the 1D chains along a.

However, the competition with another non Fermi surface driven instability can subtly modify the filling of the bands so that it is not clear if the situation is apparently more similar to the $m = 5$ member; the existence of multiple harmonics makes clear that the mechanism is not that of a traditional CDW type mechanism.

The theoretical data reported in this chapter provide a firm basis for the discussion of a large body of the structural and transport properties of the much debated $MPTB_p$.

Chapter 5

Group V transition metal oxides and chalcogenides

5.1 Introduction

Transition metal oxides and chalcogenides have been extensively studied on experimental and theoretical bases for decades [4, 5, 135–137]. This group of compounds are particularly interesting because of their specific physical properties such as metal-to-insulator transition, magnetism and superconductivity [138–143].

This chapter is about of some *Ta* and *Nb* compounds which are found to be low dimensional with layered or chain-like structure. The physical properties of these low dimensional materials are dominated by their structural characteristics. All studied compounds in this chapter include one member of the group V transition metals, *Ta* or *Nb*. The electronic properties of these materials strongly depend on the coordination of the transition metal (*Ta* or *Nb*) and the number of its d-electrons which is giving rise to an array of properties from metallic to semimetallic and semiconducting [144–151].

Low-dimensional transition metal oxides and chalcogenides often exhibit structural and electronic instabilities leading to anomalies in their transport properties. This was one of the reasons why some of the compounds in this chapter were the subject of an intensive study for many years [152–160]. We have investigated the electronic structure of four compounds: $Sr_5Nb_5O_{17}$, $2H\text{-}NbSe_2$, $TaTe_4$ and Ta_2NiSe_7 and here are going to be presented results of their band structure, Fermi surface and Lindhard response function. Our goal is to understand if Fermi surface nesting is at the origin of the structural and resistivity anomalies exhibited by these compounds. This question has been debated for a longtime in the four cases.

5.2 $Sr_5Nb_5O_{17}$

$Sr_5Nb_5O_{17}$ belongs to the family of low dimensional materials of the homologous series $A_nB_nO_{3n+2}$. This group of materials has a perovskite related layered structure which differs only slightly from the three-dimensional network of the parent ABO_3 perovskite structure because of the presence of excess oxygen. In the formula $A_nB_nO_{3n+2}$, A can be Ca, Sr or La and B is usually Ti or Nb. $Sr_5Nb_5O_{17}$ is the most intensively studied $A_nB_nO_{3n+2}$ type of compound because of its unusual chemical and physical properties [152, 161–164].

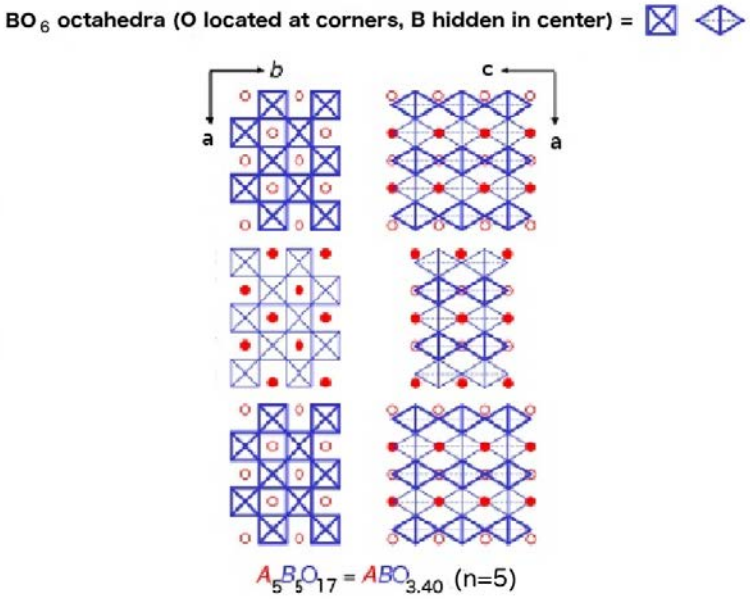

Fig. 5.1 Sketch of the crystal structure of the $n = 5$ member of perovskite-related layered homologous series $A_nB_nO_{3n+2}$. Circles represent the A cations. Within the layers the corner-shared BO_6 octahedra extend zig-zag-like along the b-axis and chain-like along the c-axis.

The $A_nB_nO_{3n+2}$ type oxides are very often expressed as ABO_x, whereby the corresponding oxygen content x of a structure type n is calculated as $x = 3 + 2/n$. Depending of the oxygen stoichiometry, these oxides exhibit different physical properties. Thus, when A is an alkali-earth cation, the $n = 4$ (or $x = 3.5$) compounds are insulators and display ferroelectricity with very high transition temperatures while compounds with $n = 4.5$ (compounds where layers with $n = 4$ and $n = 5$ alternate) and $n = 5$ (or $x = 3.4$) are metallic conductors and some of them show quasi-one-dimensional (1D) metallic behaviour at high temperatures [152]. When lowering the temperature the $n = 5$ compounds show metal-to-semiconductor transition.

Crystal structure of compounds from the series $A_nB_nO_{3n+2} = ABO_x(x = 3 + 2/n)$ is derived from the ABO_3 perovskite-type structure with slabs of vertex-sharing BO_6 octahedra, Figure 5.1. The B_nO_{3n+2} slab is built from B_nO_{5n+1} zigzag units of n octahedra, Figure 5.2a.

These zigzag units assemble together forming B_nO_{4n+2} chains by sharing $n-1$ equatorial oxygen atoms, Figure 5.2b, and finally forming the B_nO_{3n+2} layer upon sharing all of their apical oxygen atoms, Figure 5.2c [152, 165]. The crystal structure of $Sr_5Nb_5O_{17}$ is shown in Figure 5.3. The consecutive slabs are shifted with respect to each other by half of the cell. The cations reside in the empty tunnels of these layers except those of the outer part of the layer which are somewhat shifted towards the other layer and occupy the interslab region. The octahedra on the opposite sides of the interslab region do not share oxygen atoms leaving in that way to an extra layer of oxygen atoms compared to the ideal perovskite structure.

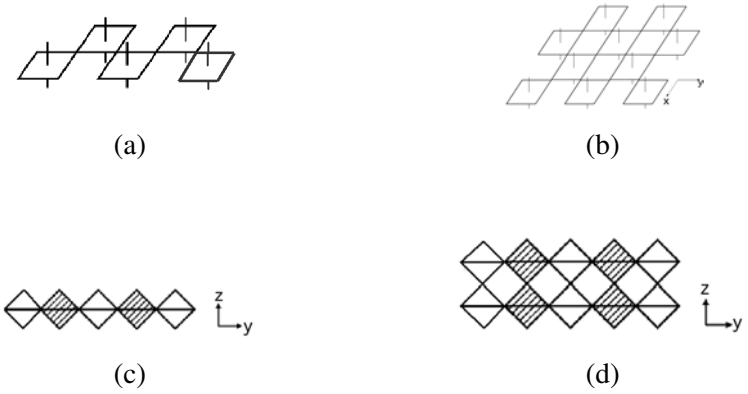

Fig. 5.2 Building up of the perovskite like structure of $A_nB_nO_{3n+2}$ type compound with $n=5$.

The ideal perovskite structure is corresponding to $n=\infty$. Systems with non-integral values of n, like $n=4.5$, are built up of successive slabs with different n values (i.e. alternatively slabs with $n=4$ and $n=5$ for the 4.5 case). The A cations usually exhibit an irregular coordination.

$Sr_5Nb_5O_{17}$ is a one-dimensional metal along the c-axis according to resistivity, far infrared spectroscopy and angle-resolved photoemission [150, 161, 163]. This is in contrast with the $n=4$ member of the series, $Sr_4Nb_4O_{14}$ which is a room-temperature semiconductor as a result of a high temperature (1615 K) ferroelectric distortion. Around 40 K, $Sr_5Nb_5O_{17}$, exhibits a metal to semiconductor transition opening a small gap of a few meV [161]. The microscopic origin of this transition is still unknown. The 1D character of the conductivity makes us to suspect that it could be due to Fermi surface nesting.

The NbO_6 octahedra in the slabs of $SrNbO_{3.40}$ are found to be $(4+1+1)$ distorted. Distortion of BO_6 octahedra is a common feature of the members of $A_nB_nO_{3n+2}$ series [150, 165–168]. Distortion is the highest for the octahedra at the edges of the slab and is the lowest for the ones in the middle of the slab, Figure 5.1. It has been believed that distortions

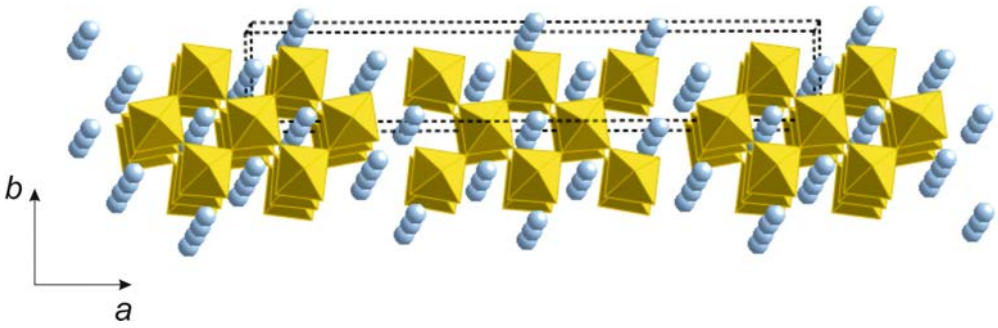

Fig. 5.3 Polyhedral representation of the crystal structure of $Sr_5Nb_5O_{17}$.

of the octahedra are responsible for the one-dimensionality in this compound [169, 170] but, as it has been shown later, this cannot be the case [171] because the one-dimensionality of the electronic structure already occurs for the ideal (undistorted) structure.

The important step in understanding the band structure of low-dimensional perovskite-like materials as $Sr_5Nb_5O_{17}$ is the knowledge of the nature of the bottom t_{2g}-block bands, which depend on of the type of perovskite phase, transition metal nature, different local octahedral distortions and band filling. Charge carriers in $Sr_5Nb_5O_{17}$ are niobium $4d$ electrons [152, 169]. $Sr_5Nb_5O_{17}$ is thus a $d^{0.20}$ material which means that there are 0.20 electrons in d-orbitals of every Nb atom [171]. However, it should be noted that because of an oxygen excess the real stoichiometry of the material is $SrNbO_{3.41}$. Consequently, there are 0.18 electrons instead of 0.20 per Nb atom. All the calculations for this phase have been carried out with this electron filling. The unit cell in our calculations is made of two $Sr_5Nb_5O_{17}$ layers and therefore contains ten Nb atoms or five Nb atoms per each layer. Consequently, there are 1.8 d-electrons distributed between the niobium d-orbitals of the unit cell. According to a valence sum analysis the valence of niobium atoms at the borders of the slab is +4.8 and it decreases towards the center of slabs. The lower valence at the center of slabs indicates that the extra electrons in $4d$ orbitals of Nb are most probably settled at Nb sites in the middle of the slabs. Therefore, the electrical conduction in this compound is taking place mostly in the middle of the slab, where the NbO_6 octahedra are the least distorted [164].

We carried out the band structure and Fermi surface calculations for $Sr_5Nb_5O_{17}$ using the density functional theory (DFT) implemented in the SIESTA code [10–12, 172]. For these calculations we used the generalised gradient approximation (GGA), the energy cutoff of real space integration mesh of 300 Ry and the k-point grid of $15 \times 33 \times 45$. The calculated band structure of $Sr_5Nb_5O_{17}$ is shown in the Figure 5.4. In our study we used the experimental crystal structure of $Sr_5Nb_5O_{17}$ with unit cell parameters: $a = 32.456$ Å, $b = 5.674$ Å and

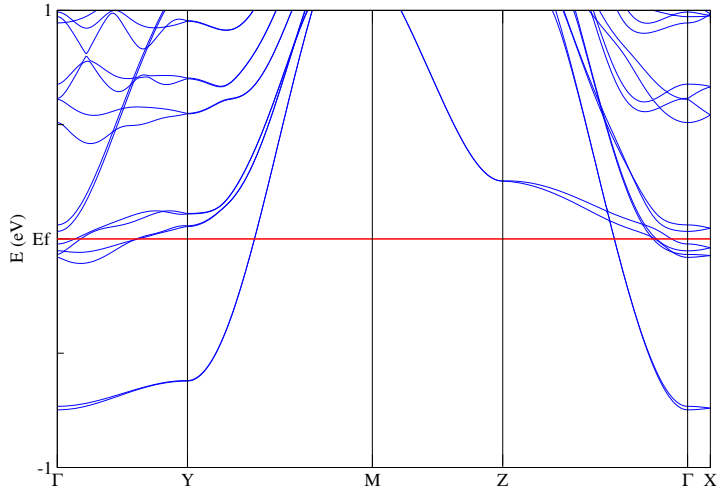

Fig. 5.4 The electronic band structure of $Sr_5Nb_5O_{17}$ (for labelling of the special points see Figure 5.5).

$c = 3.995$ Å [173]. The black crystals of $Sr_5Nb_5O_{17}$ are found to be in the *Pnnm* symmetry group [174].

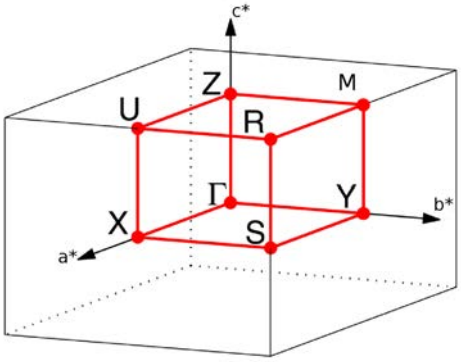

Fig. 5.5 Schematic Brillouin zone for the orthorhombic $Sr_5Nb_5O_{17}$ showing the high symmetry directions. The spatial points are: $\Gamma = (0,0,0)$, $Y = (0,0.5,0)$, $M = (0,0.5,0.5)$, $Z = (0,0,0.5)$ and $X = (0.5,0,0)$.

Because of the low electron count only the bottom part of the t_{2g}-block bands may be filled. Under such conditions, the shape of the band structure is easy to predict. The t_{2g}-block band levels of a perovskite-type slab are going to raise in energy when the orbitals of the bridging oxygen atoms are allowed by symmetry to mix with the metal t_{2g} orbitals [171]. As

there is no metal-metal interaction, knowing how many oxygen p-orbital contributions can be found in the crystal orbitals of each band for different points of the Brillouin zone, one could guess the energy dispersion and relative position of the t_{2g}-block band [175]. Thus, the band structure can be explained by counting the contribution of oxygen p-orbitals which are by symmetry allowed to mix with niobium d-orbitals.

On the basis of these ideas Tobias and Canadell [171] obtained a general qualitative band structure for the members of this family. They showed that for an ideal layer without octahedral distortions the $x^2 - y^2$ orbitals lead to 1D bands along the b direction whereas the xz/yz orbitals lead to 1D bands along the c direction. In addition they showed that the lowest band at Γ must be of the xz/yz type.

Shown in Figure 5.4 is the calculated band structure of $Sr_5Nb_5O_{17}$. The Fermi level cuts three pairs of bands and the lower part of another pair of bands is very near the Fermi level. The three lowest pairs of bands at Y are very dispersive along the Y-M and Γ-Z directions (i.e. parallel to the c direction). These orbitals are made of xz/yz Nb orbitals. The lower pair of bands at Z is very dispersive along the M-Z direction but weakly dispersive along Z-Γ. Around Γ this pair of bands undergoes an avoided crossing with the upper of the two pairs of bands strongly raising along the Γ-X line and become the third pairs of bands at Γ. This pair of bands is made of $x^2 - y^2$ orbitals of the Nb atoms. Consequently, the lower t_{2g}-block bands are all pseudo-1D bands although along different directions as predicted by the qualitative model. The lower band at Γ is an xz/yz band also in agreement with the qualitative model.

The bands occur in pairs because there are two equivalent slabs per unit cell and the interslab interactions are very weak. For simplicity, along this paragraph we will not refer to pairs of bands but simply to bands. The strongly dispersive band along M-Z which becomes the third band at Γ is built from the lowest combination of the $x^2 - y^2$ orbitals of the five Nb atoms of the repeat unit of the slab. This orbital makes δ-type interactions with the apical oxygen orbitals along the c direction but π-type interactions with part of the basal oxygen orbitals along the b direction. This is why they are 1D along the b direction. The xz/yz bands should occur in pairs for the ideal layer. However, this is not the case here because of the local distortions in the outer octahedra of the layer which make the two orbitals non equivalent. However, most of the interactions of these orbitals are δ-type with the basal oxygen orbitals but π-type with the apical oxygen orbitals so that they are 1D along the c direction.

On the Figure 5.6 is shown the calculated Fermi surface of $Sr_5Nb_5O_{17}$. It is a superposition of three contributions originating from the three pairs of bands that are crossing the Fermi level, Figure 5.4. The complete Fermi surface consists of three pairs of two types of contributions: one pair of quasi-1D Fermi surfaces perpendicular to the c^*-direction and two

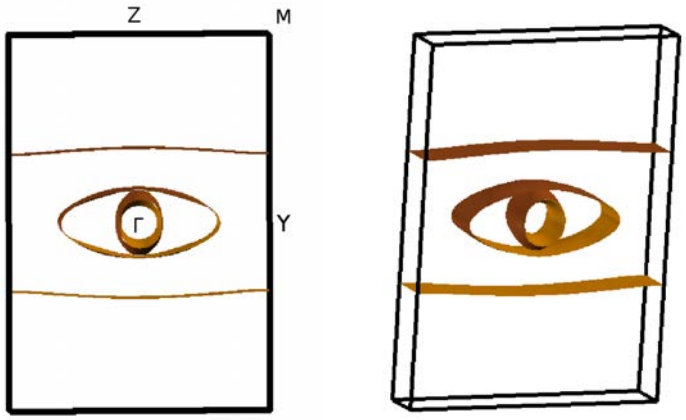

(a) (b)

Fig. 5.6 Calculated Fermi surface of $Sr_5Nb_5O_{17}$: (a) projection along the a^* direction; (b) 3D representation.

pairs of 2D Fermi surfaces with the shape of a cylinder with either circular or elliptical cross section, Figure 5.6.

The occurrence of the 1D component is in line with our previous discussion. However, the existence of two 2D components may seem at first sight surprising since the qualitative analysis lead to the prediction of the existence of just 1D components (although in orthogonal directions). Looking back to Figure 5.4 the situation becomes clear. The Fermi level falls just at the bottom of the second and third bands which are strongly dispersive along c. Because of the octahedral distortions, $Sr_5Nb_5O_{17}$ is not a perfect 1D system and these bands exhibit a small energy dispersion along the transverse direction, b. Since the filling of these bands is very low, the small curvature leads to a crossing of the Fermi level with the band along the transverse direction, closing the Fermi surface in the (b^*, c^*) plane. In addition, as mentioned above, the avoided crossing of the $x^2 - y^2$ band, which is 1D in the b direction, mixes with these bands and incorporates some dispersive character in this direction. Both, small carrier concentration and some mixing of the $x^2 - y^2$ orbitals lead to the two closed components of the Fermi surface.

The band structure and Fermi surface of $Sr_5Nb_5O_{17}$, Figures 5.4 and 5.6 respectively, show a strong one-dimensional character along the chain direction (c-direction) although the two cylinder-like components parallel to a^* should confer a non negligible 2D metallic character in the (b^*, c^*) plane. In agreement with our study, measurements of thermal and charge transport properties reveal high anisotropy of the conductivity of this compound with higher values along the chain direction [161].

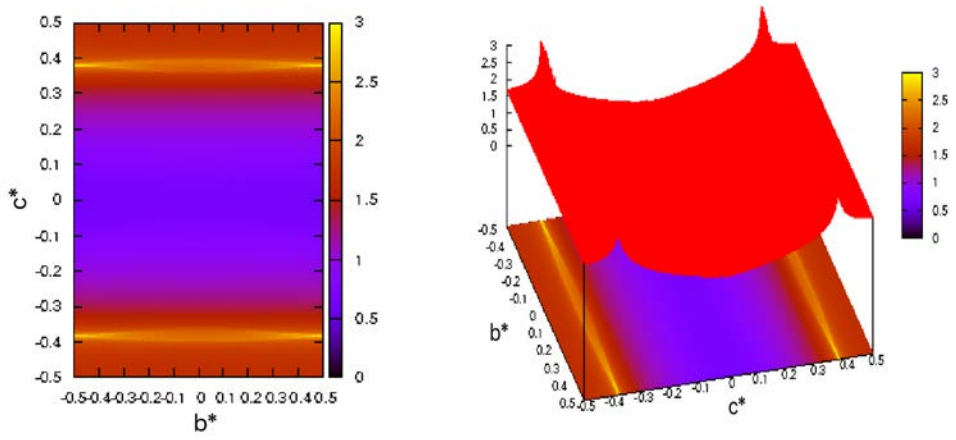

(a) (b)

Fig. 5.7 (a) (b^*, c^*) section and (b) 3D representation of the Lindhard response function for $Sr_5Nb_5O_{17}$.

The calculated Lindhard response function is shown in Figure 5.7. The more remarkable feature of this figure is the fact that the larger values occur as two lines perpendicular to c^* for the value of $0.38c^*$. In fact as one looks more carefully at the Figure it appears that the maxima occur at the border of the Brillouin zone, i.e. for $0.5b^* + 0.38c^*$ and the symmetry related points. What is the meaning of these results? For a perfect 1D system along a given direction, the Fermi surface is made of two parallel lines (really sheets in a three dimensional representation) perpendicular to the chain direction. The two lines can be nested by an infinite number of vectors having the same component along the chain direction ($2k_f$, where k_f is the Fermi wave vector) and all possible transverse components. In principle, such a system is susceptible to exhibit a density modulation with any of these wave vectors. However, if the system is not a perfect 1D and the two lines of the Fermi surface exhibit some warping, the situation is different. If the warping is weak and almost cosine-like, as it is the case in Figure 5.6, then there is only one vector that can nest the whole Fermi surface. This nesting vector has a 0.5 component in the transverse direction meaning that because of the interchain interaction, the modulation will bring also a doubling along the interchain direction. Inclusion of the 2D contributions in the calculation of the Lindhard function does not fundamentally alter the previous results although introduces additional contributions related to the flat portions of the elliptical section of the cylinders.

The Lindhard function of Figure 5.7 thus suggests that $Sr_5Nb_5O_{17}$ will behave as a pseudo-1D metal with a small but finite interchain coupling. In principle the system could exhibit a structural modulation with a wave-vector of $0.5b^* + 0.38c^*$, i.e. commensurate along the transverse direction but incommensurate along the chains direction. It is thus likely

that the 40 K transition is associated with such a kind of modulation. However, it should be noted that the Lindhard function has been calculated at 0 K. Since the transition occurs at 40 K and the temperature will lead to some smearing of the Fermi surface, it is possible that the $0.5b^*$ component is irrelevant. However, the occurrence of a $0.5b^*$ component is still possible because of the coulombic interaction between the modulations.

The present results are consistent with the 1D character of the system as found with different physical measurements [161–163]. Thus, it is tempting to assume that the 40 K transition results from a Peierls type transition associated with the nesting vector of the 1D component of the Fermi surface. However, the Fermi surface of Figure 5.6 suggests that if a Peierls modulation destroys the 1D component, the system should keep the metallic character because of the two 2D components. This is in conflict with the fact that a small but definite energy gap occurs after the 40 K transition. A possible explanation is that thermal contraction slightly modifies the structure such that the Fermi level does not cut anymore the bottom part of the second and third pairs of bands. In that case the Fermi level would only cut the lowest band and after the modulation the whole Fermi surface would be destroyed. If this is correct, the partially filled band would be filled with the extra electrons coming from the second and third pairs of bands.

Since the calculated nesting vector contains the $0.38c^*$ component, this means that the number of electrons in the 2D bands is $0.18 \cdot 5 - 2 \cdot 0.38 = 0.14$ electrons per repeat unit of the layer, i.e. $0.14/5 = 0.028$ electrons per *Nb* atom. This is a relatively small number, a 15.5% of the electrons in the *Nb d* bands. If all the electrons fill the lower 1D band as suggested then the c^* component of the nesting vector would be larger, 0.45. This explanation is puzzling in that the energy gap opened after the transition seems to be very small for a Peierls transition of a 1D system with largely dispersive partially filled band. The only way to reconcile the two facts would be that the Peierls modulation exhibits very small displacement amplitudes.

It can be argued that the thermal contraction may not be strong enough to depopulate completely the second and third bands. In that case, since the number of electrons in the 2D portions of the Fermi surface is small and can be even smaller at low temperature, it is likely that the development of the modulation due to the 1D bands induces the localization of these extra carriers in the 2D bands.

Although more experimental work is needed to solve this problem, we conclude that the 40 K transition of $Sr_5Nb_5O_{17}$ is most likely due to a Peierls like modulation with small displacement amplitudes originating from the lower xz/yz band of the layer. If a small number of extra carriers are localized as a result of the modulation or if they do not exist at low temperature where the metal to insulator transition occurs is an open question. X-ray

diffuse scattering measurements providing the c^* component of the modulation would be invaluable in providing useful information to discuss this point.

5.3 $2H$-$NbSe_2$

Since the 1960s, when the possibility of superconductivity in layered quasi-2D materials was proposed, the $2H$-$NbSe_2$ has been studied intensively. $2H$-$NbSe_2$ is metallic at room temperature, becomes superconducting at 7 K [176, 177] and there are strong indications that it is a two-gap superconductor [178–180]. Before reaching the superconducting state it undergoes a charge density wave transition at around 30 K [181, 182]. Close to 1.5 thousand papers were published to date about this compound. However, the main interest in $2H$-$NbSe_2$ has been shifted from the superconductivity to the charge density wave (CDW) instability [146, 154, 155, 182–187]. Although the occurrence of both superconductivity and CDW in this material has been known for many years [181, 182, 188], the controversy concerning the nature of the CDW has never been settled. In fact although it was known since the seventies that the CDW leads to a 3×3 superstructure [181, 188], it is only recently that the detailed crystal structure of the modulated phase has been reported [189]. In recent years, there has been an enormous interest on this material because of the possibility to prepare layers of different thickness [190, 191]. It is well established that the superconducting critical temperature diminishes when decreasing the number of layers [192, 193].

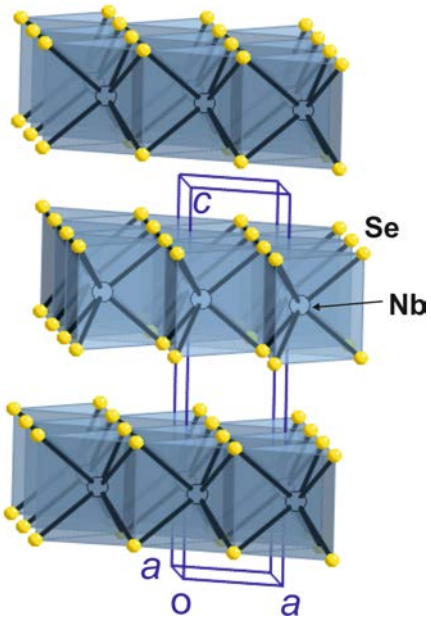

Fig. 5.8 The layered crystal structure of $NbSe_2$.

$2H$-$NbSe_2$ belongs to the group of $2H$-MX_2 phases ($M = Nb$ and $X = Se$ and Se or $M = Ta$ and $X = S$ or Se) transition metal dichalcogenides. The $NbSe_2$ structure is based on Nb layers being sandwiched between two Se layers, Figure 5.8. The Nb atoms are on a trigonal prismatic coordination. The unit cell of the solid contains two identical slabs related by a screw axis along the c direction. Successive layers are separated by van der Waals gaps through which there are relatively short Se-Se contacts, i.e., every Se atom makes three Se-Se contacts (3.537Å) shorter than the sum of the van der Waals radii with the Se atoms of the adjacent layer. The Se-Se contacts along the c direction within the hexagonal layers are even shorter, 3.347 Å. These two structural features give a considerable three-dimensional character to this layered material. The cell parameters of $2H$-$NbSe_2$ are $a = b = 3.4425$ Å and $c = 12.547$ Å, and the space symmetry group is $P6_3/mmc$ [182, 194].

The first band structure calculations for the $2H$-$NbSe_2$ were done in the 1973 using a non-self-consistent potential [145]. However, the results differ in some important aspects from the more recent DFT calculations [155, 179, 185, 195–198]. The first band structures of $2H$-$NbSe_2$ were showing two bands crossing the Fermi level, while nowadays we know that there are three bands coming from the Nb d-orbitals and Se p-orbitals.

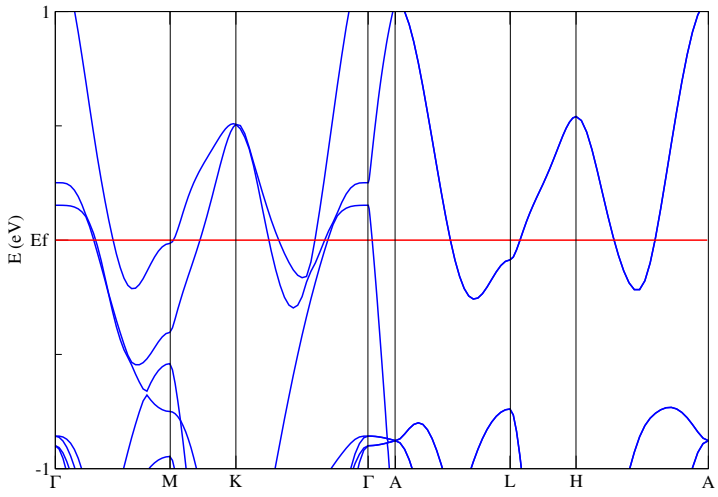

Fig. 5.9 Calculated band structure of $2H$-$NbSe_2$. (see Figure 5.10 for labelling of the special points.)

In our study the band structure and Fermi surface calculations for $2H$-$NbSe_2$ were done using density functional theory (DFT) as implemented in the SIESTA code [10–12]. The calculations were carried out with generalised gradient approximation (GGA), an energy cut

off of 300 Ry and k-point meshes of $30 \times 30 \times 15$. In the Figure 5.9 is shown the calculated band structure of $2H$-$NbSe_2$ and in the Figure 5.10 the schematic Brillouin zone.

There are three bands cutting the Fermi level, Figure 5.9. The two upper bands at Γ are coming from the *Nb* d-orbitals and contain a fairly large contribution of the *Se* p-orbitals. The third band is mainly built from the *Se* p-orbitals perpendicular to the layers, the p_z orbitals [155, 179]. Thus, the Fermi surface contains two types of contributions: those associated with the electron carriers originating from the *Nb* d-levels and those with the hole carriers originating from the *Se* p-levels. From the Figure 5.9 there are three bands cutting the Fermi level along Γ-M-K-Γ section of the Brillouin zone and only one band along the Γ-A direction. This band is coming from the *Se* p_z-orbital. The other two *Nb* d-bands remain always higher than the Fermi level along this direction.

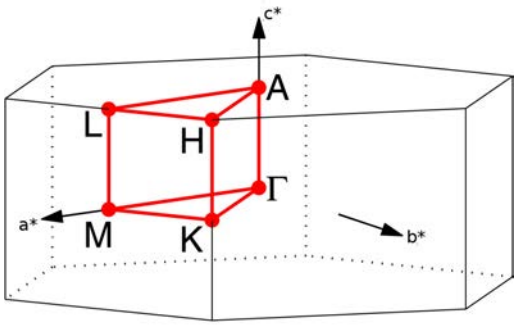

Fig. 5.10 Schematic Brillouin zone used for the band structure calculation of $2H$-$NbSe_2$. The spatial points are: $\Gamma = (0,0,0)$, $M = (0.5,0.0)$, $K = (0.33,0.33,0)$, $A = (0,0,0.5)$, $L = (0.5,0,0.5)$ and $H = (0.33,0.33,0.5)$

If it were not for the *Se* based band, the two *Nb* based bands would be half-filled since *Nb* is formally in a d^1 state. The main character of these bands changes along the Brillouin zone. At the zone center they are based on the d_{z^2} orbitals. However, around the K point they are based on the d_{xy} and $d_{x^2-y^2}$ orbitals. The unusual shape of the two bands, with minima along the Γ-M and the Γ-K directions (as well as the equivalent directions A-L and A-H at the border of the Brillouin zone) are due to this change in orbital character from the center to the border of the Brillouin zone. The two in-plane orbitals $d_{x^2-y^2}$ and d_{xy} are well oriented to interact with equivalent orbitals of neighboring *Nb* atoms. In contrast, the d_{z^2} orbital has lobes pointing outside the layer plane. Thus, the former can generate metal-metal interactions but not the latter. By symmetry, the two types of orbitals can not mix at Γ but within the Brillouin zone the two sets can smoothly mix and interchange character between different regions. Thus, the phase changes associated with the crystal orbitals of some regions of the Brillouin zone lead to bonding interactions between neighboring *Nb* atoms (the regions

around the minima) whereas in the region around Γ where the d_{z^2} character prevails, these bonding interactions are not possible and the energy is higher.

The Fermi surface contains two different contributions: one 3D hole contribution coming from *Se p*-orbitals and two 2D electron contributions coming from *Nb d*-orbitals [155, 179]. The Figure 5.11 shows the almost flat 3D portion of the Fermi surface around the Γ point arising from the *Se p* levels with the shape of a pancake and a series of tubes along the interlayer direction centered around the Γ and *K* points. originating from the *Nb d* levels.

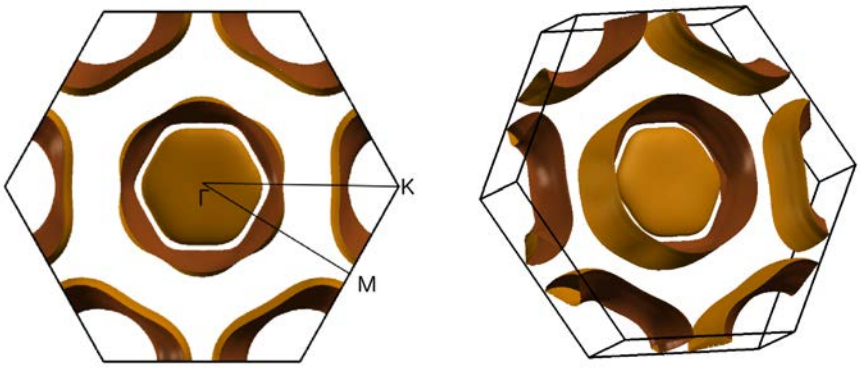

(a) (b)

Fig. 5.11 Calculated Fermi surface of $NbSe_2$; (a) projection along the c^* direction; (b) 3D representation.

Experimental works show that $2H$-$NbSe_2$ exhibits a phase transition at $T = 33.5$ K, which is assigned to be the Peierls temperature, T_p, of this compound [188]. The resistivity of $2H$-$NbSe_2$ remains metallic below T_p and shows only a small anomaly at the phase transition [199, 200]. This means that if this is a Peierls transition, the CDW does not involve a large modifications of the Fermi surface. It has been experimentally shown [188, 201] that below the temperature of the transition the system exhibits a modulation with a 3×3 supercell (in fact the system is slightly incommensurate [188] but the recent structural determination by Malliakas and Kanatzidis [189] has shown that refinement of the structure with a commensurate or incommensurate cell does not lead to any significant difference). The 3×3 modulation results from the existence of three modulations with wave vectors $q_1 = 1/3a^*$, $q_2 = 1/3b^*$ and $q_3 = (1/3a^* - 1/3b^*)$ along the three main directions of the hexagonal plane. The resistivity [200] and heat-capacity [199] measurements indicate that the decrease in the density of states at the Fermi level associated with CDW formation is only of the order of 1%. These facts seem to argue against a Fermi surface nesting mechanism origin of the 3×3 modulation in $2H$-$NbSe_2$.

The origin of the CDW in $2H$-$NbSe_2$ has been a matter of debate for around forty years. Initially, it was attributed to a Fermi surface driven CDW [181]. The suggestion was based on the shape of the Fermi surface for earlier calculations [145]. However this explanation has been challenged [154, 155, 185, 186, 198, 202]. Rice and Scott [186] soon proposed that the CDW was driven by saddle points lying within $k_B\ T_{CDW}$ of the Fermi level and separated by the $1/3a^*$ and equivalent wave vectors [186]. Doran et al [154, 202] used simple tight-binding models to evaluate the susceptibility and showed that indeed it did not exhibit sharp peaks. This led them to propose that strong coupling was at the origin of the instability. A similar conclusion was reached by Whangbo and Canadell on a basis of different tight-binding calculations [198]. Most of these calculations were not based on first-principles and for instance lacked an ingredient of the presently known Fermi surface of the material: the pancake-like hole contribution. More recently several first-principles calculations have been reported both for the bulk and single layers [153, 179, 196, 197, 203]. In a very detailed study, Mazin et al. [155] carried out DFT calculations for the Fermi surface and Lindhard response function and proposed that Fermi surface nesting was not at the origin of the CDW formation. However, the same type of calculations led to the wrong prediction of a 2×2 CDW modulation for $2H$-$NbSe_2$ single-layer [197] so that it is not clear if this type of approach correctly describes the electronic structure of the material. In addition, no microscopic mechanism was proposed to explain the origin of the modulation. Finally, a recent DFT study of our group [203] could successfully explain most of the physical measurement for single-layer $NbSe_2$. It was shown that the driving force for the modulation originates from levels which are around 1.3 eV lower than the Fermi level and that the transition leads to an increase of the *Nb-Nb* bonding. It must be mentioned that a similar debate concerning the origin of the CDW modulation has developed within the photoemission community. A useful account can be found in the review by Rossnagel [204]. Thus we decided to apply the same kind of calculations used previously for single-layer $2H$-$NbSe_2$ to the bulk.

From the calculated electronic band structure and Fermi surface, Figures 5.9 and 5.11 respectively, one can notice that there could be a so called "self-nesting" of the pancake shaped Fermi surface sheets inside themselves. According to the calculated band structure and Fermi surface, there could be nesting in the Γ-M direction between the flat parts of tubular Fermi surfaces with a nesting vector which is not far from the experimental one. However, the warping along c^* of the pseudo-cylindrical walls is non-negligible so that it is not clear if such feature would provide a sizeable driving force.

Thus, we carried out the Lindhard response function calculation for $2H$-$NbSe_2$ and the results are shown in Figure 5.13. This Figure exhibits six very weak and broad maxima along

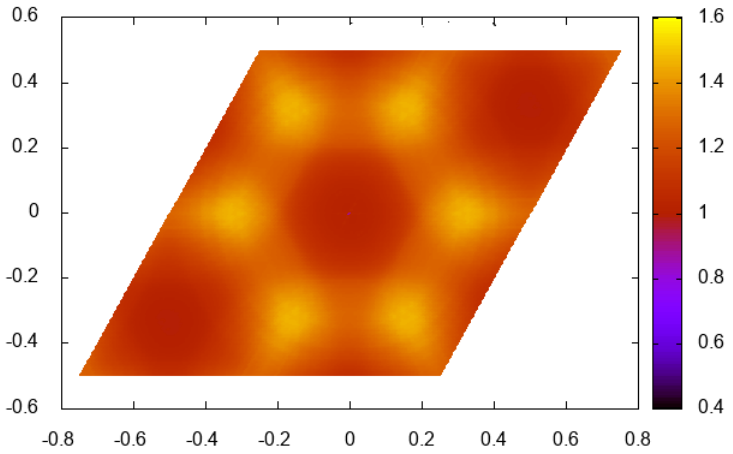

Fig. 5.12 (a^*,b^*) section of the response function for $2H$-$NbSe_2$.

the Γ-M line. These peaks are not far from the $1/3a^*$ value. However, as it is clear from the very diffuse maxima as well as from a 3D representation of Figure 12, there are no sharp maxima in the response function as required to have a Peierls type instability. Consequently, the 3×3 modulation of $2H$-$NbSe_2$ can not originate from a Fermi surface nesting driven mechanism. The possible self-nesting of the cylinders is not effective in stabilizing the modulation observed for $2H$-$NbSe_2$.

We are thus led to the conclusion that the low temperature structural modulation in $2H$-$NbSe_2$ must originate from levels which are not at the Fermi level. This is in agreement with the very low effect of the modulation on the conductivity. The origin of the 3×3 modulation was analysed in detail for the case of a single-layer [203]. In that case it was found that the largest change in the density of states occur around 1.3 eV below the Fermi level and leads to the splitting of a large *Se*-based peak which however contains an important participation of the *Nb* d_{xy} and $d_{x^2-y^2}$ orbitals making *Nb-Nb* in-plane interactions. When the CDW occurs the peak splits in two peaks; the lower peak is mostly associated with the *Nb-Nb* interactions which are shortened in the CDW structure and provide a stabilization. The upper peak is mostly associated with the *Nb-Nb* interactions which are lengthened in the CDW and thus provide a destabilization. The stabilized levels have a stronger weight in the density of states so that the distortion associated with the CDW provides a small but finite stabilization to the system. We have verified that the density of states of the bulk and single-layer exhibit essentially the same features. Thus, we propose that the origin of the CDW modulation of bulk $2H$-$NbSe_2$ is the same as for the isolated single-layer and is unrelated to the Fermi

surface. Despite being one of the first materials for which a Fermi surface driven mechanism was proposed to explain the CDW and the debate originated through almost forty years, we believe that the source of stabilization is simply an optimization of the extended *Nb-Nb* bonding along the hexagonal layers.

5.4 $TaTe_4$

The polychalcogenides are an interesting group of quasi-one-dimensional compounds, some of them containing linear chains of metal atoms. In many of these compounds CDW-like distortions have been observed. The tetratellurides, MTe_4 (where $M = Nb$ or Ta), have been found in the 1960s when their basic structure was determined [205, 206].

The $TaTe_4$ crystal structure consists of columns of $TaTe_4$ containing linear chains of metal atoms, like the ones on the Figure 5.13. *Ta* atoms are coordinated by eight *Te* atoms, which are making successive squares. These squares are being rotated with respect to each other, so that *Ta* atoms are in the centre of a square antiprism. The $TaTe_4$ chains run along the c-axis and repeat forming a tetragonal structure. $NbTe_4$ occurs with the same structure. Both systems exhibit metallic properties at room temperature [148, 207]. Thus, we can say that this is a quasi-1D system with metallic properties. Both systems exhibit a modulated structure already at room temperature [208, 209]. $TaTe_4$ exhibits a structural transition around 823 K [206] towards a commensurate $2a \times 2a \times 3c$ modulation, the structure of which was solved by De Boer et al. [208]. $NbTe_4$ exhibits a more complex behaviour with several intermediate transitions towards incommensurate structures [156, 209, 210] before the lock-in to the same commensurate structure as $TaTe_4$ is reached at 50 K [211]. Boswell et al. [156] observed three types of superlattice spots for $TaTe_4$. They proposed that they were due to the formation of three different CDWs with wave vectors $(0,0,c^*/3)$, $(a^*/2,a^*/2,c^*/3)$ and $(a^*/2,0,c^*/3)$. In the case of $NbTe_4$, the c^* is near but not exactly $1/3$ leading above 50 K to incommensurate structures [156, 209, 210].

Conventionally, this structure can be presented as in the Figure 5.14. The closest approaches between *Te* atoms in the same chain are the edges of the *Te* squares and are 3.287Å and the closest distance between *Te* atoms between neighbouring chains is 2.928 Å[206]. This indicates that the *Te-Te* interactions are strong between the neighbouring chains, and thus, maybe a better description of the system would be provided by Figure 5.14b where Te-Te bonds linking the different chains have been highlighted whereas the Te atoms of the square units are considered as non bonded. In fact, both figure 5.14a and 5.14b highlight different aspects of the structure and the real situation should be something in-between the

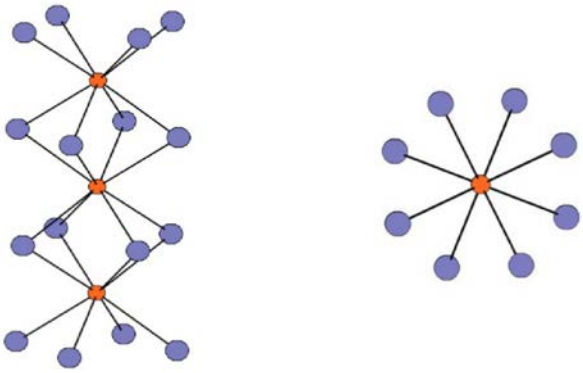

(a) (b)

Fig. 5.13 The structure of $TaTe_4$; orange -*Ta* atoms, violet -*Te* atoms; (a) lateral view, (b) top view along the *c*-axis.

two descriptions. In anyway, this clearly suggests that these solids must be less clearly 1D than usually considered and the electronic structure should be rather 3D.

Both $NbTe_4$ and $TaTe_4$ are room temperature metals when the system exhibits a modulation [148, 207]. The resistivity of $TaTe_4$ does not exhibit major anomalies in the investigated temperature range because the commensurate modulation already is present at room temperature. The conductivity is almost isotropic in the (a,c) plane. For $NbTe_4$ there is a variation on the derivative of the resistivity around 50 K when the lock-in of the modulation occurs and there is a decrease of the conductivity below this temperature.

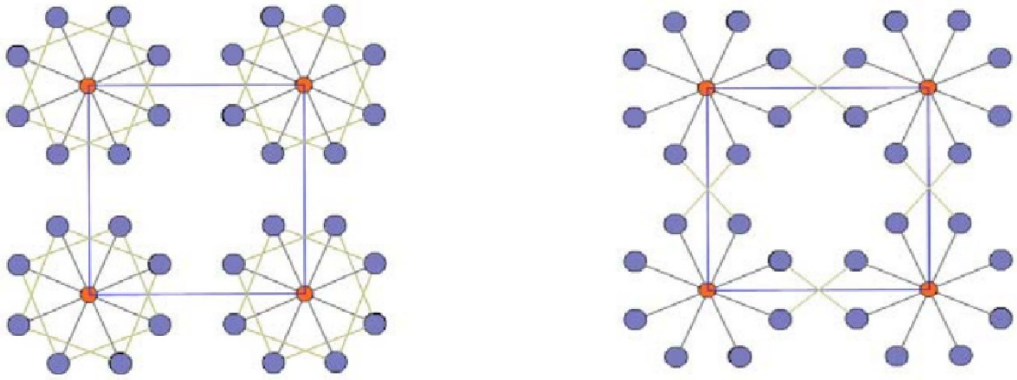

(a) (b)

Fig. 5.14 The structure of $TaTe_4$ along the *c*-direction (a) each *Ta* atom is surrounded by eight *Te* atoms in a square anti-prismatic coordination; (b) Representation emphasising that the closest distances between the *Te* atoms are amongst the *Te* atoms of the neighbouring chains.

From the theoretical viewpoint not much has been done concerning these materials. The only electronic structure works from which we are aware are those of Bullett [212] and Whangbo and Gressier [213]. Bullet proposed that the interchain interactions are strong but no detailed mechanism for the modulation was proposed. Whangbo and Gressier reported tight binding electronic structure calculations for $NbTe_4$. They suggested that the Fermi surface of these system exhibits flat but warped sheets and the c^* component of the possible nesting vectors was around $1/4$ which is not in good agreement with the experimental values of $1/3$ or nearly $1/3$. Walker and Morelli [214] put forward an interpretation of the different transitions in $NbTe_4$ on the basis of a Guinzburg-Landau free energy approach of interacting chains. Finally, let us note that the electronic structure of $TaTe_4$ was experimentally studied by Zwick et al. [215] by means of angular resolved photoemission spectroscopy. These authors concluded that both 1D and 3D features were present at the Fermi level. Thus, the electronic structure of these materials is clearly not yet well understood and we decided to revisit the electronic structure of $TaTe_4$ on the basis of first-principles DFT calculations using the average structure of $TaTe_4$ [208].

We calculated the electronic band structure and the Fermi surface of $TaTe_4$ using the SIESTA code [10–12]. Our calculations were done with the mesh cutoff of 200 Ry and the k-grid of $30 \times 30 \times 10$. The band structure is represented on the Figure 5.15 and the Brillouin zone used for the band structure calculation is schematically shown on the Figure 5.16. The unit cell vectors of the average structure of $TaTe_4$ are $a = 6.5154$ Å, $b = 6.5154$ Å and $c = 6.8118$ Å, and the compound crystallizes in the $P4cc$ space symmetry group [208].

The calculated band structure of the average, non modulated structure of $TaTe_4$ is shown in Figure 5.15 (see Figure 5.16 for the labelling of the special points). Essentially there are two bands crossing the Fermi level. The first one is the band crossing the Fermi level along the Γ-Z line. This band meets at Z a descending one along the same line. In fact these two bands are simply a folded band because there are two Ta atoms per unit cell along c related by a two-fold screw axis. This band is strongly based on the Ta d_{z^2} orbitals and thus has a strong dispersion along the chains direction (this band also crosses the X-R and M-S lines which are parallel to the c^* direction). However it is clear from Figure 5.15 that the lower of these bands has also quite a large dispersion along the interchains direction (see for instance the dispersion along the Γ-M line). Consequently, the character of this band is in-between those of a pseudo-1D and 2D bands. The second band crosses the Fermi level along the Γ-M and M-X directions and along both directions exhibits a very strong dispersion. This band is also folded along the c^* direction and the upper subband crosses also the Fermi level so that it has a character between 2D and 3D. This band results from a complex mixing between Te and Ta orbitals. The π^* orbitals of the Te_2 units which must be formally full in a $(Te_2)^{2-}$

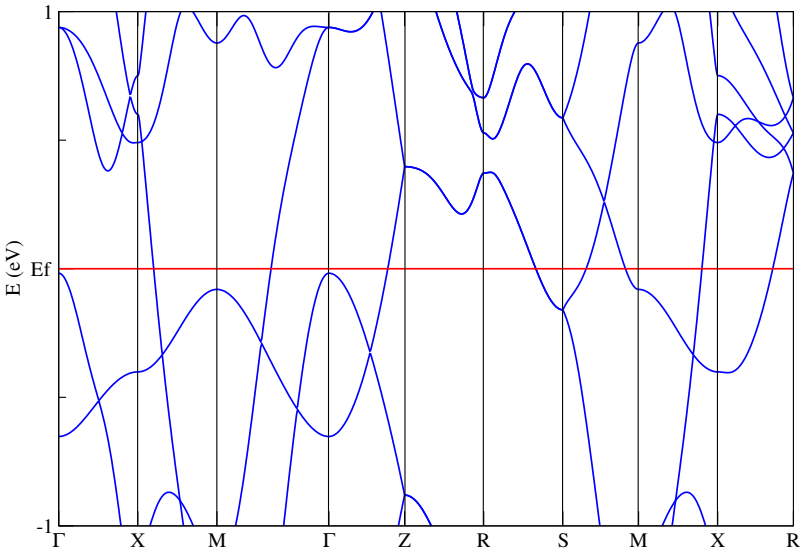

Fig. 5.15 Calculated band structure of $TaTe_4$ using the non modulated average structure [208].

unit interact strongly with the *Ta* d_{xy} and $d_{x^2-y^2}$ orbitals. The bands based on the *Ta* d_{xy} and $d_{x^2-y^2}$ orbitals should formally be higher than the *Ta* d_{z^2} band and consequently they should be empty. However because of the very strong mixing between *Ta* d_{xy} and $d_{x^2-y^2}$ and *Te* π^* orbitals this band is strongly stabilized in several parts of the Brillouin zone and becomes partially filled. Since the Te_2 units are inclined with respect to the c axis, this type of interaction provides good coupling along the (a^*, a^*) plane but also along c^*.

In transition metal tellurides the relatively low electronegativity of tellurium frequently leads to complex scenarios of competition between metals and non-metals about the valence electrons. As a consequence, valence electron localizations in either sub-lattice introduce various types of homonuclear bonding and numerous examples are known where the *Te-Te* distances fall bellow the sum of the Van-der-Waals radii [216, 217]. This is exactly what happens here. If we consider that the *Te* atoms are bonded into Te_2 dimers, each Te_2 dimer is then counted as a Te_2^{2-} unit and each *Ta* atom in $TaTe_4$ would exist as Ta^{+4} (d^1) ion [213]. This means that the *Te* valence bands should be completely filled and the lower *Ta d* band should be half-filled. Is this in agreement with the calculated band structure? Let us note that the unit cell of the average structure of $TaTe_4$ contains two *Ta* atoms related through a twofold screw axis. This means that all bands are folded along the c direction and can

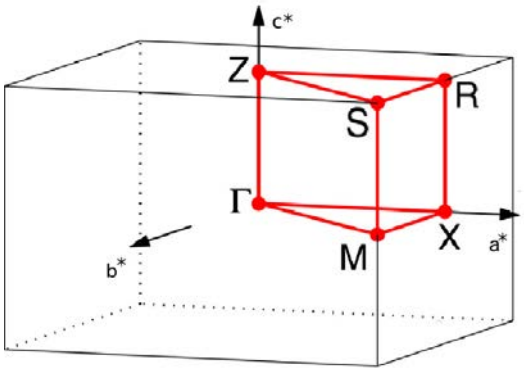

Fig. 5.16 Schematic Brillouin zone used for the calculation of the band structure of $TaTe_4$. The spacial points are $\Gamma = (0,0,0)$, $Z = (0,0,0.5)$, $R = (0.5,0,0.5)$, $X = (0.5,0,0)$, $S = (0.5,0.5,0.5)$ and $M = (0.5,0.5,0)$

be seen as an upper and a lower subband touching at the Z point. Consequently the $Ta\ d_{z^2}$ subband must contain two electrons if the Ta atoms are formally in a d^1 situation. As we have discussed above, this subband is not completely filled since it crosses the Fermi level. The reason is that another band, the second band discussed above, which should be empty is in fact partially filled. As we discussed above the last band contains large contributions of the $Ta\ d_{xy}$ and $d_{x^2-y^2}$ orbitals (as well as $Te_2\ \pi^*$). Consequently, the both $Ta\ d_{z^2}$,d_{xy} and $d_{x^2-y^2}$ are partially filled at the Fermi level. Formally, since all Te based levels below the Ta ones are filled, the description based on Te_2 units is correct and the Ta atoms must be $Ta\ d^1$. However, because of the strong Ta-Te interactions described by the second band, there is an internal and partial electron transfer between the d_z^2 and the d_{xy} and $d_{x^2-y^2}$ orbitals.

The X-ray and electron diffraction studies show that $TaTe_4$ undergoes structural modulation towards $2a \times 2a \times 3c$ superstructure [156, 205, 206]. If the modulation was due, as it was previously proposed, to a Peierls distortion of the $TaTe_4$ chains, then the commensurate $c^*/3$ component along the chain direction would mean that the Ta based d_{z^2} band must be either one-third empty or one-third filled. In principle, from a qualitative viewpoint, if the Ta is d^1, one should expect that because of some transfer from Te to Ta, the upper $Ta\ d_{z^2}$ subband becomes one-third filled and leads to a new structure with a c parameter three times larger through a Peierls scenario. However, this is in contradiction with our analysis of the band structure. To begin with the interchain interactions associated with the $Ta\ d_{z^2}$ band are quite noticeable and the system is at most pseudo 1D. In addition, we have seen that there is an internal transfer between the $Ta\ d_{z^2}$, d_{xy} and $d_{x^2-y^2}$ levels. Although in principle one could think that because of this internal electron transfer the lower $Ta\ d_{z^2}$ subband becomes one-third empty, it is virtually impossible that with such complex band structure with two bands undergoing avoided and real crossing, the filling was a commensurate one, i.e., just

one-third empty. According to the present band structure, if there was some kind of Peierls distortion it should be incommensurate, in disagreement with the experimental observation. From this analysis we are left with the conclusion that the structural modulation is most likely due to a scenario not involving nesting of the Fermi surface. However, before concluding in that way we should first consider the nature of the Fermi surface of the system.

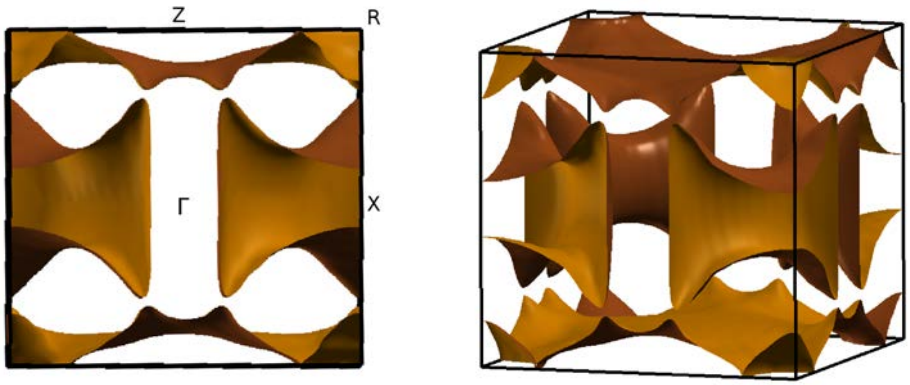

(a) (b)

Fig. 5.17 Calculated Fermi surface for the average structure of $TaTe_4$: (a) projection view along the one of the a^* directions; (b) 3D representation.

The calculated Fermi surface is shown in Figure 5.17. It contains two different contributions associated with the two partially filled bands discussed above. The two contributions relatively flat near the top and bottom of the Brillouin zone borders along the c^* direction are associated with the $Ta\ d_{z^2}$ band. These portions are strongly related to those calculated by Whangbo and Gressier [213]. Note that they are very irregular and considerably warped. When taking into account the periodicity, these contributions can be considered as a 3D object with several holes and many peaks. It is then expected that this object does not have good nesting properties. The second contribution is made up of four pieces around the M points of the Brillouin zone which, taking into account the periodicity of the lattice, are really 3D objects. These objects do not exhibit nesting properties along the c^* direction. In contrast, they have quite large flat portions perpendicular to the diagonal directions of the (a^*,a^*) plane. Thus, none of the two components of the Fermi surface seem to exhibit good nesting properties along the c^* direction; in any case, there could be some nesting along the perpendicular directions.

In order to quantify these observations we have calculated the Lindhard response function. Shown in Figures 5.18 and 5.19 are two different sections, (a^*,c^*) and (a^*,a^*) respectively. The (a^*,c^*) section is very flat and no clear maxima appears. In the (a^*,a^*) section there are some peaks which occur by pairs not far from the $(0.2a^*,0.2a^*)$ and diffuse lines parallel to

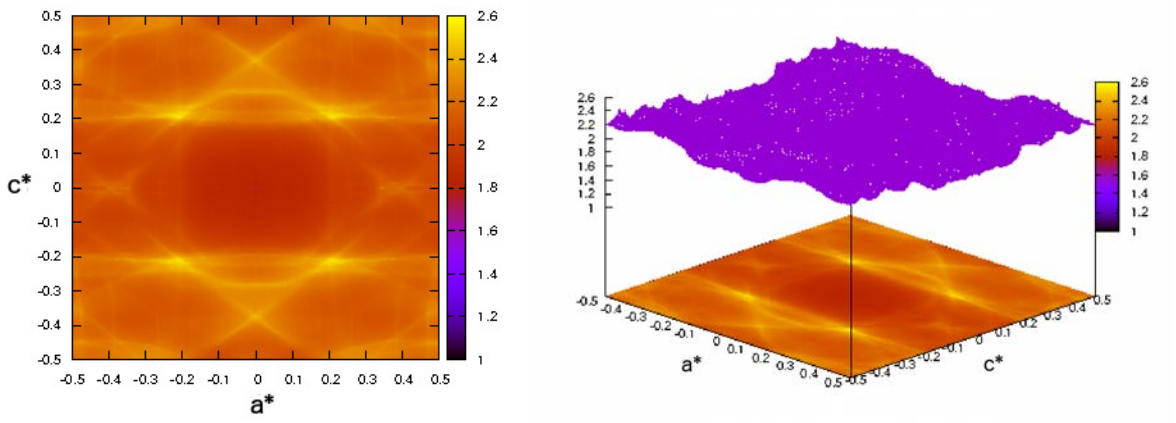

(a) (b)

Fig. 5.18 The results of the Lindhard function calculation for $TaTe_4$ in the a^*-c^* plane.

the diagonal directions going through the $(0.5a^*, \sim 0.2a^*)$ and $(\sim 0.2a^*, 0.5a^*)$ and those related by symmetry. These features are those related to the nesting associated with the Fermi surface contributions of the band with strong Ta d_{xy} and $d_{x^2-y^2}$ character. Thus, we may conclude that there are no maxima in the Lindhard function which can provide support for a Fermi surface nesting driven mechanism for the structural modulation exhibited by $TaTe_4$.

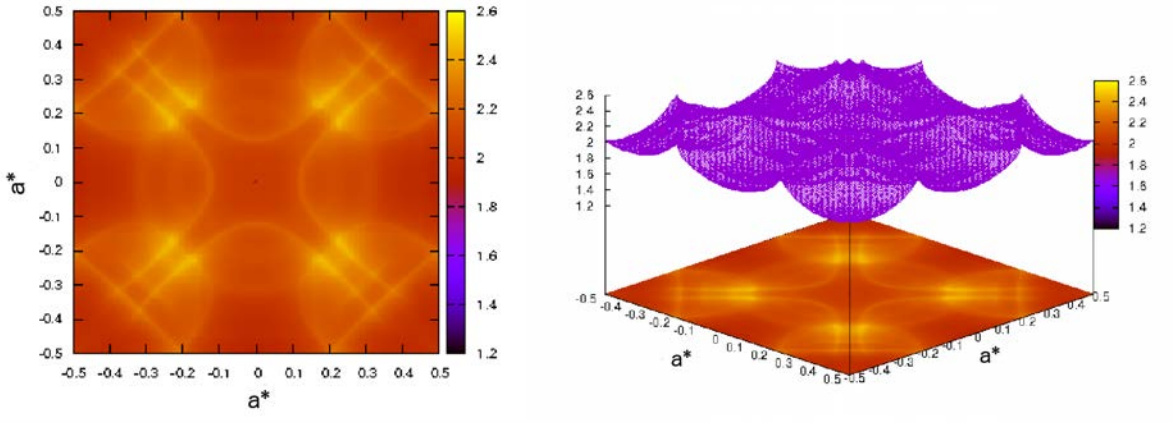

(a) (b)

Fig. 5.19 Calculated Lindhard function for $TaTe_4$ in the $a^* - a^*$ plane.

As it was the case for $2H$-$NbSe_2$, we are led to the conclusion that the driving force for the modulation occurring in this compound is due to energy levels which do not occur at the Fermi level. The calculated band structure for the $(2a \times 2a \times 3c)$ modulated structure

of $TaTe_4$ is shown in Figure 5.20. It is clear that it corresponds to a metallic system, in agreement with the experimental observations. We have also optimised the structures of the average non modulated and modulated structures of $TaTe_4$. In these calculations we fully optimised the positions of the atoms keeping the cell constants fixed at their experimental values (identical in both cases except for the multiplication of the basic cell). We found that the modulated structure is more stable by 45 meV per formula unit. Comparison of both the experimental or optimised structures for the modulated and non modulated systems suggest that the driving force for the modulation is an optimization of the interchain *Te-Te* contacts.

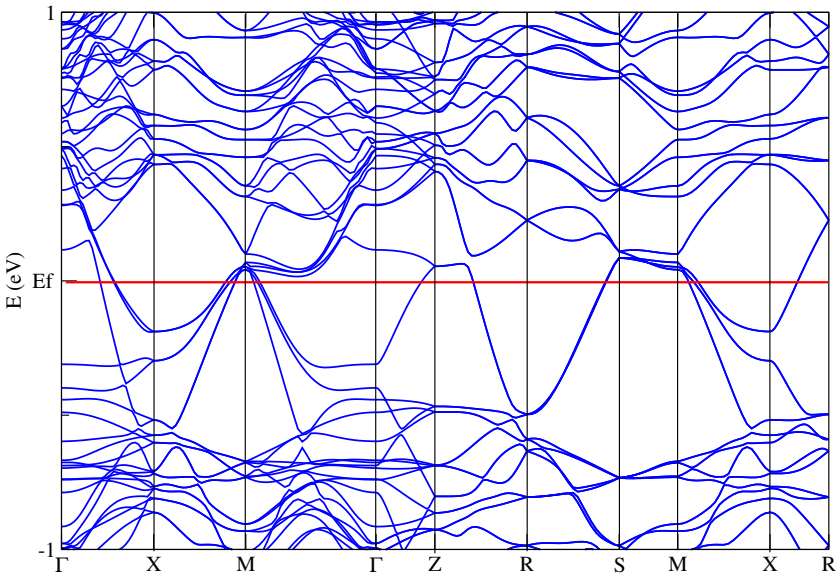

Fig. 5.20 Calculated band structure of the modulated structure of $TaTe_4$

$2H$-$NbSe_2$ and $TaTe_4$ thus provide two examples of non Fermi surface driven CDWs: whereas in the first case the driving force was optimization of the transition metal bonding, in the second, it is optimization of the chalcogen-chalcogen bonding.

5.5 Ta_2NiSe_7

Some transition-metal chalcogenides are layered compounds, of which several representatives have a commensurate or incommensurate charge density wave (CDW) state at low temperatures. The puzzling properties of $NbSe_3$ and TaS_3 [218–220] associated with the occurrence

of two different incommensurate CDWs, have launched a lot of effort in the search of ternary transition-metal chalcogenides which may exhibit unexpected transport properties. In the last decades many ternary transition-metal chalcogenides have been synthesized [221–224] but only a few of them really undergo a charge density wave transition [225, 226]. One of the few compounds for which a structural modulation has been characterized is Ta_2NiSe_7 [159, 160, 225, 227] although its origin has not been elucidated yet. The obvious structural relations with $NbSe_3$ and $Fe_3Nb_3Se_{10}$, two CDW materials, suggest that as in the case of these materials, the modulation could be Fermi surface driven. We consider this problem in this section by means of DFT calculations.

The layered ternary chalcogenides, Ta_2MSe_7, where M can be Ni or Pt, have a structure related to that of $FeNb_3Se_{10}$ [226]. Therefore, it was believed that the Ta_2MSe_7 group of compounds are going to exhibit similar physical properties as $FeNb_3Se_{10}$ and show as well the charge density wave transitions.

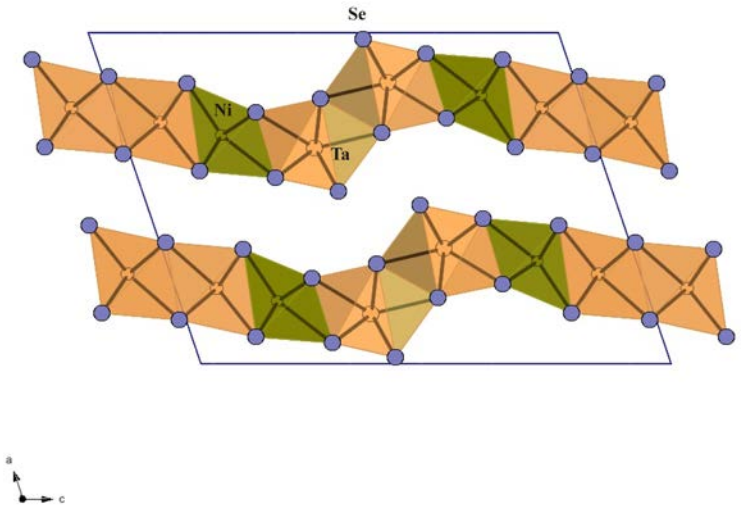

Fig. 5.21 View of the structure of Ta_2NiSe_7 perpendicular to the (a,c) plane. The three types of chains run along the b-axis.

The Ta_2MSe_7 has a laminar structure with layers extending parallel to the c-axis, Figure 5.21. Each slab is composed of three types of chains that run along the b-axis. Each of these chains occurs four times in the unit cell, twice in each slab. The first type of chains contains edge sharing octahedra centered by Ta atoms. The second chain type consists of edge sharing octahedra with Ni atoms displaced from the centers of these octahedra to give square-pyramidal geometry about the metal atoms. The reason of the distortion of the square-pyramidal geometry is not clear but may be the consequence of interactions between Ni and Ta atoms. The third chain type is made of Ta-centered bicapped trigonal prisms of

Se atoms that share triangular faces along the *b*-axes. These trigonal prisms contain *Se*-*Se* bonds.

As suggested by the oxidation formalism $(Ta^{5+})_2(M^{2+})(Se^{2-})_5(Se_2^{2-})$, these ternary chalcogenides are supposed to have semiconducting properties but Ta_2NiSe_7 is found to be a semimetal [159, 225]. As shown by Canadell and Whangbo [151] by means of a tight-binding study the origin of this fact lies in the fact that the bottom *d*-block bands of the *Ta* octahedral chains overlaps wit the top of the *Se p*-block bands of the trigonal prismatic chains. These authors suggested that a CDW along the *b* direction originating from nesting of the Fermi surface could occur for this compound. As a matter of fact, a structural modulation associated with a resistivity anomaly was later reported [227]. Although the modulation occurs along the *b* direction, as predicted, the wavevector is different from the proposed one. Here we must take into account that the correct description of the small band overlap in a semi-metal is a notoriously difficult question for a tight-binding approach. Consequently, it is not clear if the disagreement is simply due to a lack of accuracy of the tight-binding calculations or if it is a more fundamental question. In view of results in the preceding sections it could be that the modulation was not driven by the Fermi surface of the system. In what follows we examine this question by means of first-principles DFT calculations.

On the Figure 5.22 is shown the calculated band structure of Ta_2NiSe_7. The calculation was done with the SIESTA code [10–12] using the k-grid of $15 \times 50 \times 15$ and the mesh cutoff of 300 Ry. The lattice is C-centered monoclinic, with the lattice parameters $a = 13.827$ Å, $b = 3.482$ Å , $c = 18.577$ Å and $\beta = 108.80$ [225].

Figure 5.22 shows that bands are dispersive along the chain axis, the *b*-axis, but relatively flat along the direction perpendicular to the chain, the *c*-axis. The dispersion along the interlayer direction is comparable to that along the interchains direction. Thus one could think that the system is simply a pseudo-1D metal. However, as Figure 5.22 shows, the situation is more complex.

The Fermi level cuts four bands three of which are quite dispersive along the chains direction, Γ-*Y*. To describe them it is best to first concentrate on the Γ-*Y* direction of Figure 5.22b. Apparently the Fermi level cuts four bands but it can be seen that one of the bands undergoes a strongly avoided crossing with an empty band and then crosses again the Fermi level. Starting at the Γ point and moving along the Γ-*Y* line the Fermi level almost immediately crosses the very top of a strongly descending band. This band (**band 1** from now on) is not dispersive at all along the two transverse directions and is kept above even if very near the Fermi level all along the (a^*, c^*) section of the Brillouin zone passing through Γ. Thus, this is a strongly 1D band. This band is mostly build from the *Se p* orbitals of *Se*1 which are shared between the two octahedral chains. Continuing along the Γ-*Y* line the

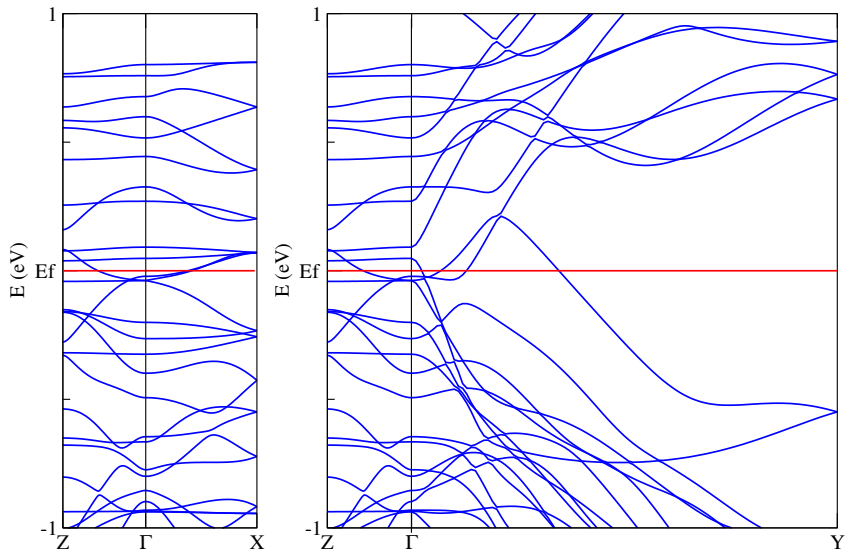

Fig. 5.22 The band structure of Ta_2NiSe_7 in the Z-Γ-X direction and in the Z-Γ-Y direction of the Brillouin zone. The spatial points are: $\Gamma = (0,0,0)$, $X = (0.5,0,0)$, $Y = (0,0.5,0)$ and $Z = (0,0,0.5)$ in units of the reciprocal lattice vectors.

Fermi level cuts a second band (from now on **band 2**) dispersive along the Γ-Y line which then undergoes the above mentioned avoided crossing. This band becomes the second filled band at the Γ point through a very weakly avoided crossing and is somewhat dispersive along the interchain (Γ-Z) direction. Along the Γ-X direction goes weakly up in energy and finally crosses the Fermi level in this direction. This band is built from the *Ta* atoms of the octahedral chains and one should expect a Fermi surface contribution where the 1D nature is however overshadowed by a strong warping. After raising in energy and undergoing a strongly avoided crossing this band goes down and crosses again the Fermi level at around one-third of the Γ-Y line (we will refer to this second part as **band 2'**). Since there is a strongly avoided crossing, the nature of the band before and after the avoided crossing is however very different. Band 2' is build from the *Ni* orbitals of the chains in between the two types of *Ta* chains. Tracing back this band at Γ it is possible to see that it has dispersion along the two transverse directions. Thus one should expect a quasi-3D behaviour. The third band crossing the Fermi level along Γ-Y (**band 3** from now on), which is undergoing an avoided crossing just before crossing the Fermi level, is also based on the *Ta* orbitals of the octahedral chains. Tracing back the character of this band at Γ it is possible to see that it

becomes the sixth filled band at this point which has nil dispersion along the two transverse lines. Thus, this band should lead to a completely flat contribution in the Fermi surface. This band is also made of the *Ta* orbitals in the octahedral chains. There is a fourth band crossing the Fermi level which can be seen when looking carefully to the band structure of the Figure 5.22a. This band (**band 4**) which originates from a *Se* based band strongly raising in energy around Γ, where it becomes the first filled band. This band is quite flat along the interlayer (Γ-*X*) direction bur crosses the Fermi level around the middle of this line and acquires dispersion along the interchain direction (Γ-*Z*). This band is going to give quite extended hole pockets. The band is based on the *p* orbitals of the *Se*4 which are part of the octahedral chains but facing the *Ni* atoms of the next chain.

It is clear from the previous discussion that the main carriers for the conductivity should be electrons of the *Ta* atoms in octahedral chains, electrons of the *Ni* atoms, and holes of the *Se* atoms of the octahedral chains. The bicapped *Ta* trigonal prismatic chains apparently do not contribute at all to the conductivity and act only as a kind of glue keeping together the other chains.

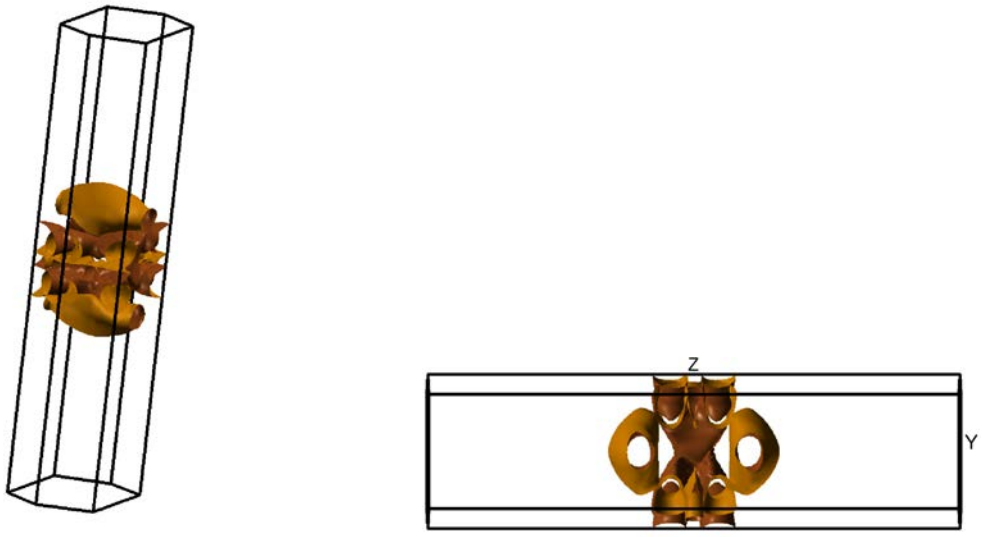

(a) (b)

Fig. 5.23 Two different views of the calculated Fermi surface of Ta_2NiSe_7.

From the previous discussion we should expect a relatively complex Fermi surface. As noted, band 1 should lead to a strongly 1D contribution along the *b* direction, i.e. two planes perpendicular to b^*, very near the center of the Brillouin zone (associated with the *Se* atoms shared by the two octahedral chains). In contrast the contributions of band 2 (octahedral *Ta* states) and 2' (*Ni* states) should be very warped and irregular. Let us note that since bands

3 and 4 undergo a strongly avoided crossing near the Fermi level, the two bands will mix quite strongly at the Fermi level. In this situation it is not convenient to work with the two bands separately to understand their topological features but with both at the same time. Only in that way the hidden features of each of them clearly appear. In the present case we should expect a complex mixing of two hidden components: (i) one very flat pair of planes associated with band 3 (octahedral *Ta* states) and a series of pockets quite irregular associated with band 4 (*Se* states of the octahedral chains)). The Fermi surface should result from the hybridization of these four components. The calculated Fermi surface is shown in Figure 5.23. It is indeed quite complex at the first sight. However we can recognise the two main 1D or pseudo-1D components discussed above. The flat component very near the center of the Brillouin zone perpendicular to the long direction (b^*) is quite clearly visible in Figure 5.23a (the two planes at both sides of Γ are so near each other that they look as if they were collapsed). The pairs of 1D component related to band 3 are more clearly visible in the Fermi surface cut of Figure 5.23b. Superposed and hybridized with these planes are two very warped planes coming from band 2 and an almost 3D component near the middle of the Brillouin zone associated to band 2' and finally several closed but extended pockets associated with band 4.

It is obviously not easy to guess the possible nesting properties associated with this Fermi surface. We have thus calculated the Lindhard response function which is shown in Figure 5.24. What is immediately clear from there is that despite the puzzling shape of the Fermi surface there are two clearly 1D components. As we explained before the presence of lines in the Lindhard function are associated with the presence of flat planes in the Fermi surface, i.e., 1D states. The lines associated with a very small value of the b^* component, i.e. the yellow lines almost at the center of the drawing, are associated with the flat planes originating from band 1. The lines associated with a value of the b^* component around 0.07 are associated with the nesting between the planes originating from band 3 and the planes of band 1. Other than this there is no indication of good conditions for a CDW to develop in this system. At this point we must remind that the modulation observed in this material has a b^* component of 0.48 [159], which is completely different from those of the two series of lines in the Lindhard function. Consequently, we must conclude that the structural modulation in Ta_2NiSe_7 does not have a Fermi surface nesting origin.

Are there some reasons for the fact that the nesting in the Fermi surface is not at the origin of the modulation? We believe that none of the two types of nesting may be very effective in providing an energy gain. First, the pair of planes very near the center of the Brillouin zone are to near the center and consequently, the gaps opened by the modulation should be very small. Second, the nesting of the band 3 and 1 is coupling *Ta* states with *Te*

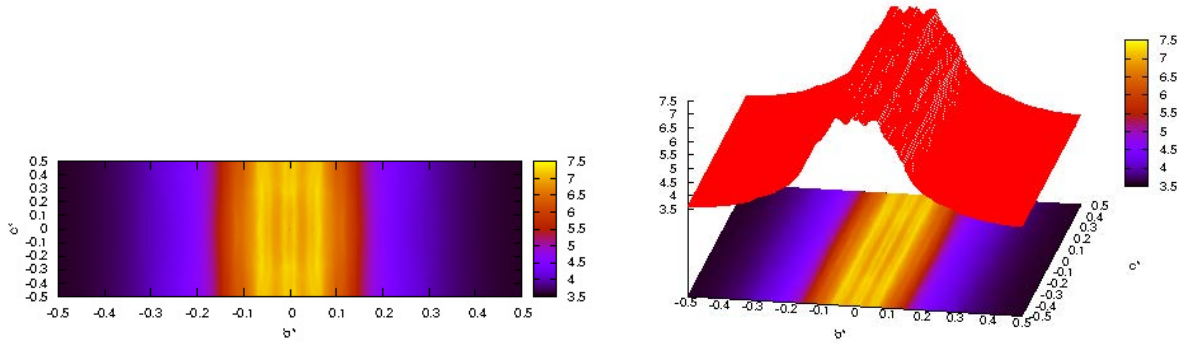

(a) (b)

Fig. 5.24 b^*-c^* section of the response function calculated for Ta_2NiSe_7.

states. When the matrix element in the numerator of the real response function are taken into account they are most likely very small because of the different orbital nature. Thus, we conclude that the Fermi surface does not provide a real driving force towards a modulation.

What is then the origin of the structural modulation in this compound? Looking at the modulated structure, the atoms that are more strongly affected by the modulation are the *Ni* atoms and the *Se*2 ones. The latter are those in the octahedral chains which are leading to the long *Ni*-*Se* contact that is taken as an indication that the coordination of the *Ni* atom is not octahedral but square pyramidal. However this distance is not extremely longer (2.73 Å) compared to the opposite one (2.47 Å). This means that there is indeed some bonding associated with the *Ni* and *Se*2 atoms and that the *Ni* atom should not be described as being square pyramidally coordinated. Thus the modulation is most likely associated with an attempt to optimise the bonding between this pair of atoms. The question is now: why a b^* component very near 0.5 thus meaning that the modulation is almost a dimerization? The *Se*2 is making a *Se*-*Se* bond with the nearest *Se* of the bicapped trigonal prismatic *Ta* chain. Thus, when the *Se*2 tries to approach the *Ni* atom to provide some stabilization the *Se*-*Se* bond is lengthened, thus providing a destabilization. Consequently, the *Se*2 atoms experiences two conflicting forces and the dimerization is the result of this trade. The global stabilization must be relatively weak and this is why the modulation only occurs at low temperature (52 K). The fact that the wave vector of the modulation is $0.48b^*$ instead of $0.5b^*$ is most likely due to the presence of defects, quite usual in these ternary compounds. Let us note that this interpretation is consistent with the fact that the modulation is accompanied by an anomaly in the resistivity. As the calculated band structure shows, the *Ni* states are contributing at the Fermi level so that the modulation in the *Ni*-*Se*2 distances must affect the partial density of states of the *Ni* atoms at the Fermi level and consequently, the resistivity of the material. We

thus conclude that the CDW in Ta_2NiSe_7 does not originate from its Fermi surface but subtly affects it.

5.6 Conclusions

We have studied four compounds which have in their structure group V transition metals Nb and Ta. These compounds are low dimensional with layered or chain-like structure and have anisotropic physical properties. Because of their low dimensionality, metallic properties and occurrence of structural modulations, these compounds are often discussed as possible Fermi surface driven CDW materials. However the real origin of the CDWs in these materials has never been elucidated. Thus we have decided to examine if some instability of the Fermi surface is really at the origin of these modulations. Calculation of the band structure, Fermi surface and the Lindhard response function for $Sr_5Nb_5O_{17}$, $2H$-$NbSe_2$, $TaTe_4$ and Ta_2NiSe_7 has led us to the following conclusions:

- The 40K transition of $Sr_5Nb_5O_{17}$ is most likely due to a Peierls like modulation with small displacement amplitudes originating from the lower Nb d_{xz}/d_{yz} band of the layers. The pseudo-1D character of the bottom t_{2g}-block bands is not due to the octahedral distortions but to the topology of the octahedral layers. This is the only compound of those examined in this chapter for which a Fermi surface driven instability is found to be at the origin of the CDW.

- The 3×3 modulation of $2H$-$NbSe_2$ can not originate from a Fermi surface nesting driven mechanism because the calculated Lindhard function does not exhibit sharp peaks but very broad and weak maxima. The possible self-nesting of the cylinders is not effective in stabilizing the modulation observed for $2H$-$NbSe_2$. In analogy with recent works of our group concerning single-layers of $NbSe_2$, we propose that the source of stabilization of the CDW is simply an optimization of the extended Nb-Nb bonding along the hexagonal layers.

- The Lindhard function for $TaTe_4$ does not exhibit sharp maxima which can provide support for a Fermi surface nesting driven mechanism for its structural modulation. We suggest that the driving force for the modulation is simply an optimization of the interchain Te-Te contacts. $2H$-$NbSe_2$ and $TaTe_4$ provide two examples of non Fermi surface driven CDWs: whereas in the first case the driving force is optimization of the transition metal bonding, in the second, it is optimization of the chalcogen-chalcogen bonding.

- The Fermi surface of Ta_2NiSe_7 results from the hybridization of both flat and very warped components leading to a complex shape. The Lindhard calculation suggest some possible instabilities of the Fermi surface. However they are unrelated to the observed structural modulation. Again, the structural modulation in Ta_2NiSe_7 does not have a Fermi surface nesting origin. We suggest that the modulation results from the competition of the tendency of the *Ni* atoms to complete their coordination towards an octahedral environment and the strength of the *Se-Se* bonds occurring in the bicapped trigonal prismatic *Ta* chains of this material.

Chapter 6

Conclusions

Organic semiconductors became scientifically very interesting group of materials because of their good charge-transport properties and massive technological applications. Among all of them, rubrene gained grate interest because it is a organic semiconductor with the highest carrier mobility which can reach a few tens of cm^2/Vs. However, a full *ab initio* characterization of the electronic properties and electron-phonon coupling (including Holstein and Peierls type of couplings) is representing a difficult tusk, which might be due to the sizeable structure of the rubrene unit cell consisting of 280 atoms and resulting in 840 vibrational modes.

There has been a great interest in low dimensional transition metal compounds for several decades because of their peculiar electric, magnetic and structural properties. Such specific characteristics originate from the possibility to obtain partial oxidation states of the transition metal atoms. Low dimensional compounds are known for having anisotropic physical properties and because of their low dimensionality, metallic properties and occurrence of structural modulations, these compounds are often discussed as possible Fermi surface driven CDW materials. However, the real origin of the CDWs in these materials has never been clarified and thus we have decided to examine if some instability of the Fermi surface is really at the origin of these modulations.

In this thesis we have studied electron-phonon coupling in rubrene and the electronic properties of some of the low-dimensional compounds:

- In the Chapter 3 we derived reliable method for calculation of material parameters from DFT approach and applied it on rubrene crystal. For the calculation of electronic, phononic and electron-phonon coupling parameters of rubrene we were using DFT base methods. Hereby, we showed a practical way to calculate accurate phonon frequencies and avoid imaginary frequencies in low-frequency modes. The accuracy of phonon

frequencies is of the great importance in the calculation of electron-phonon interaction because the highest electron-phonon coupling constants are coming from the low frequency modes. We derived TB model to compute parameters for the Holstein-Peierls type Hamiltonian and the results are in a very good agreement with the ones in the literature. The calculation of phenyl group motions led us to the conclusion that the flipping configuration of rubrene is not stable but that it might be possible in the longer time scale

- In the Chapter 4 was shown a detailed study of the electronic structure for several $MPTB_p$ phases, the ones with $m = 4, 5, 6, 7, 8$ and 12. Calculation of the band structure, Fermi surface and Lindhard response function showed that for all of the selected $MPTB_p$ members (except for the $m = 4$) there are six different maxima in the Lindhard response function which are associated with common nesting vectors for two of the three different 1D partially filled bands of these bronzes. Our results show that the structural modulations occurring in the low members of the series, $m = 4, 5$ and 6, originate from the Fermi surface driven CDWs of the step layers while for the high m members of the series, $m = 8, 12$, the structural modulations are due to non Fermi surface related mechanisms.The $m = 7$ phase is a borderline compound where one of the modulations originates from the Fermi surface instability whereas the other is unrelated to the Fermi surface.

- In the Chapter 5 we have studied four compounds which have in their structure group V transition metals Nb and Ta:

  - $Sr_5Nb_5O_{17}$ is the only compound of those studied in this chapter that shows a Fermi surface driven CDW transition. The transition at 40K is due to a Peierls like modulation with small displacement amplitudes originating from the lower *Nb d*-band of the layers. The 1D character of the bottom t_{2g}-block bands is due to the topology of the octahedral layers.
  - The Lindhard response function calculation for $2H\text{-}NbSe_2$ shows that there are no sharp peaks but broad maxima and that the observed 3×3 modulation is not driven by Fermi surface nesting. In relation with recent works of our group on single layers of $NbSe_2$ we suggest that the source of stabilization of the CDW is an optimization of the extended *Nb-Nb* bonding along the hexagonal layers instead of previously thought self-nesting of the cylinders.
  - In the case of $TaTe_4$ Lindhard response function does not show sharp maxima and we conclude that there is no a Fermi surface nesting driven mechanism in the

origin of its structural modulation. Along with 2H-$NbSe_2$, $TaTe_4$ is an example of non Fermi surface driven CDWs where in the origin of the modulation lies optimization of the Te-Te bonding.

– The Lindhard calculation in Ta_2NiSe_7 shows some possible instabilities of the very complex Fermi surface which cannot be related to the observed structural modulations. The structural modulation in this compound is not driven by Fermi surface nesting and is probably appearing under the influence of Ni and Se_2 atoms.

References

[1] H.Sirringhaus, "Device Physics of Solution-Processed Organic Field-Effect Transistors," *Advanced Materials*, vol. 17, no. 20, pp. 2411–2425, 2005.

[2] M. E. Gershenson, V.Podzorov, and A.F.Morpurgo, "Colloquium: Electronic transport in single-crystal organic transistors," *Reviews of Modern Physics*, vol. 78, no. 3, pp. 973–989, 2006.

[3] Z.Bao and J.Locklin, *Organic Field-Effect Transistors*. CRC Press, Boca Raton, 2007.

[4] E.Revolinsky, B.E.Brown, D.J.Beerntsen, and C.H.Armitage, "The selenide and telluride systems of niobium and tantalum," *Journal of the Less Common Metals*, vol. 8, no. 1, pp. 63–72, 1965.

[5] J.A.Wilson and A.D.Yoffe, "The transition metal dichalcogenides discussion and interpretation of the observed optical, electrical and structural properties," *Advances in Physics*, vol. 18, no. 73, pp. 193–335, 1969.

[6] G.Grüner, *Density Waves in Solids*. Addison-Wesley Publishing Company, 1994.

[7] R.M.Martin, *Electronic Structure: Basic Theory and Practical Methods*. Cambridge University Press, 2004.

[8] P.Hohenberg and W.Kohn, "Inhomogeneous Electron Gas," *Physical Review*, vol. 136, no. 3B, pp. B864–B871, 1964.

[9] W.Kohn and L.J.Sham, "Self-Consistent Equations Including Exchange and Correlation Effects," *Physical Review*, vol. 140, no. 4A, pp. A1133–A1138, 1965.

[10] J.M.Soler, E.Artacho, J. Gale, A.García, J.Junquera, P.Ordejón, and D.Sánchez-Portal, "The SIESTA method for ab initio order-N materials simulation," *Journal of Physics: Condensed Matter*, vol. 14, no. 11, p. 2745, 2002.

[11] E.Artacho, J.M.Cela, J. Gale, A.García, J.Junquera, R.M.Martin, P.Ordejón, D.Sánchez-Portal, and J.M.Soler, "User's Guide for SIESTA," https://launchpad.net/siesta.

[12] P. Ordejón, "Linear Scaling ab initio Calculations in Nanoscale Materials with SIESTA," *Physica Status Solidi B*, vol. 217, no. 1, pp. 335–356, 2000.

[13] E.Artacho, E.Anglada, O.Diéguez, J. Gale, A.García, J.Junquera, R.M.Martin, P.Ordejón, J.M.Pruneda, and D.Sánchez-Portal, "The SIESTA method; developments and applicability," *Journal of Physics: Condensed Matter*, vol. 20, no. 6, p. 064208, 2008.

[14] D.Sánchez-Portal, P.Ordejón, E. Artacho, and J.M.Soler, "Density-functional method for very large systems with LCAO basis sets," *International Journal of Quantum Chemistry*, vol. 65, no. 5, pp. 453–461, 1997.

[15] M.Born and R.Oppenheimer, "Zur Quantentheorie der Molekeln (On the Quantum Theory of Molecules)," *Annalen der Physik*, vol. 389, no. 20, pp. 457–484, 1927.

[16] M.A.El'yashevich, "From the origin of quantum concepts to the establishment of quantum mechanics," *Soviet Physics-Uspekhi*, vol. 20, no. 8, pp. 656–682, 1977.

[17] E.H.Lieb and B.Simon, "Thomas-Fermi Theory of Atoms, Molecules and Solids," *Advances in Mathematics*, vol. 23, pp. 22–116, 1977.

[18] J. C. Philips and L. Kleinman, "New Method for Calculating Wave Functions in Crystals and Molecules," *Physical Review*, vol. 116, no. 2, pp. 287–294, 1959.

[19] N.Troullier and J.Martins, "Efficient pseudopotentials for plane-wave calculations," *Physical Review B*, vol. 43, no. 3, pp. 1993–2006, 1991.

[20] L.Kleinman and D.M.Bylander, "Efficacious Form for Model Pseudopotentials," *Physical Review Letters*, vol. 48, no. 20, pp. 1425–1428, 1982.

[21] J. Junquera, Ó. Paz, D. Sánchez-Portal, and E. Artacho, "Numerical atomic orbitals for linear-scaling calculations," *Phys. Rev. B*, vol. 64, no. 235111, 2001.

[22] F.Bloch, "Über die Quantenmechanik der Elektronen in Kristallgittern (German)," *Zeltschrift für Physik*, vol. 52, no. 7, pp. 555–600, 1929.

[23] J.C.Slater and G.F.Koster, "Simplified LCAO Method for the Periodic Potential Problem," *Physical Review*, vol. 94, no. 6, pp. 1498–1524, 1954.

[24] H.Jones, N.F.Mott, and H.W.B.Skinner, "A Theory of the Form of the X-Ray Emission Bands of Metals," *Physical Review*, vol. 45, no. 6, pp. 379–384, 1934.

[25] F.Ortmann, F.Bechstedt, and K. Hannewald, "Charge transport in organic crystals: Theory and modelling," *Physica Status Solidi B*, vol. 248, no. 3, pp. 511–525, 2011.

[26] F.O, K.Hannewald, and F. Bechstedt, "Ab initio description and visualization of charge transport in durene crystals," *Applied Physics Letters*, vol. 93, no. 22, 2008.

[27] G.Grüner, "The dynamics of charge-density waves," *Reviews of Modern Physics*, vol. 60, no. 4, pp. 1129–1181, 1988.

[28] P.Monceau, "Electronic crystals: an experimental overview," *Advances in Physics*, vol. 61, no. 4, pp. 325–581, 2012.

[29] H.Fröhlich, "On the Theory of Superconductivity: The One-Dimensional Case," *Proceedings of the Royal Society A*, vol. 233, no. 1154, 1954.

[30] P.Monçeau, N.P.Ong, A.M.Portis, A.Meerschaut, and J.Rouxel, "Electric Field Breakdown of Charge-Density-Wave-Induced Anomalies in $NbSe_3$," *Physical Review Letters*, vol. 37, no. 10, pp. 602–606, 1976.

[31] E.Canadell and M.-H.Whangbo, "Charge-density-wave instabilities expected in monophosphate tungsten bronzes," *Physical Review B*, vol. 43, no. 1894, 1991.

[32] E.Canadell, M-L.Doublet, and C.Iung, *Orbital Approach to the Electronic Structure of Solids*. Oxford University Press, 2011.

[33] Y.Kitamura, E.Shikoh, S.Z.Bisri, T.Takenobu, and M.Shiraishi, "Electrical investigation of the interface band structure in rubrene single-crystal/nickel junction," *Applied Physics Letters*, vol. 99, no. 4, p. 043505, 2011.

[34] T.Petrenko, O.Krylova, F.Neese, and M.Sokolowski, "Optical absorption and emission properties of rubrene: insight from a combined experimental and theoretical study," *New Journal of Physics*, vol. 11, no. 1, p. 015001, 2009.

[35] C. Silva, "Organic semiconductors: A little energy goes a long way," *Nature Materials*, vol. 9, no. 11, pp. 884–885, 2010.

[36] D. Wang, L. Tang, M. Long, and Z. Shuai, "First-principles investigation of organic semiconductors for thermoelectric applications," *The Journal of Chemical Physics*, vol. 131, no. 22, p. 224704, 2009.

[37] Z. Li, V. Podzorov, N. Sai, M. Martin, M. Gershenson, M. Di Ventra, and D. Basov, "Light Quasiparticles Dominate Eletronic Transport in Molecular Crystal Field-Effect Transistors," *Physical Review Letters*, vol. 99, no. 1, p. 016403, 2007.

[38] G.Horowitz, "Organic Field-Effect Transistors," *Advanced Materials*, vol. 10, no. 5, pp. 365–377, 1998.

[39] H.Kleemann, S.Schumann, U.Jörges, F.Ellinger, K.Leo, and B.Lüssem, "Organic pin-diodes approaching ultra-high-frequencies," *Organic Electronics*, vol. 13, no. 6, pp. 1114–1120, 2012.

[40] H.Kleemann, A.A.Günther, K.Leo, and B.Lüssem, "High-Performance Vertical Organic Transistors," *Small*, vol. 9, no. 21, pp. 3670–3677, 2013.

[41] S.Steudel, K.Myny, V.Arkhipov, C.Deibel, S.De Vusser, J.Gence, and P.Heremans, "50 MHz rectifier based on an organic diode," *Nature Materials*, vol. 4, no. 8, pp. 597–600, 2005.

[42] F. Ortmann, K. Radke, A. Günther, D. Kasemann, K. Leo, and G. Cuniberti, "Materials Meets Concepts in Molecule-Based Electronics," *Advanced Functional Materials*, vol. 25, no. 13, pp. 1933–1954, 2014.

[43] D. A. da Silva Filho, E.-G. Kim, and J. L. Brédas, "Transport Properties in the Rubrene Crystal: Electronic Coupling and Vibrational Reorganization Energy," *Advanced Materials*, vol. 17, no. 8, pp. 1072–1076, 2005.

[44] E. Menard, A. Marchenko, V. Podzorov, M. Gershenson, D. Fichou, and J.A.Rogers, "Nanoscale Surface Morphology and Rectifying Behavior of a Bulk Single-Crystal Organic Semiconductor," *Advanced Materials*, vol. 18, no. 12, pp. 1552–1556, 2006.

[45] A. Troisi, "Prediction of the absolute charge mobility of molecular semiconductors: the case of rubrene," *Advanced Materials*, vol. 19, no. 15, pp. 2000–2004, 2007.

[46] J. Weinberg-Wolf, L. McNeil, S. Liu, and C. Kloc, "Evidence of low intermolecular coupling in rubrene single crystals by Raman scattering," *Journal of Physics: Condensed Matter*, vol. 19, no. 27, p. 276204, 2007.

[47] R. Zeis, C. Besnard, T. Siegrist, C. Schlockermann, X. Chi, and C. Kloc, "Field Effect Studies on Rubrene and Impurities of Rubrene," *Chemistry of Materials*, vol. 18, no. 2, pp. 244–248, 2006.

[48] Y. Okada, M. Uno, Y. Nakazawa, K. Sasai, K. Matsukawa, M. Yoshimura, Y. Kitaoka, Y. Mori, and J. Takeya, "Low-temperature thermal conductivity of bulk and film-like rubrene single crystals," *Physical Review B*, vol. 83, no. 11, p. 113305, 2011.

[49] H.Burroughes, D.D.C.Bradley, A.R.Brown, R.N.Marks, K.Mackay, R.H.Friend, P.L.Burns, and A.B.Holmes, "Light-emitting diodes based on conjugated polymers," *Nature*, vol. 347, pp. 539–541, 1990.

[50] C.Murawski, K.Leo, and M.C.Gather, "Efficiency Roll-Off in Organic Light-Emitting Diodes," *Advanced Materials*, vol. 25, no. 47, pp. 6801–6827, 2013.

[51] S.Reineke, M.Thomschke, B.Lüssem, and K.Leo, "White organic light-emitting diodes: Status and perspective," *Reviews of Modern Physics*, vol. 85, no. 3, pp. 1245–1293, 2013.

[52] C.W.Tang and S.A.VanSlyke, "Organic electroluminescent diodes," *Applied Physics Letters*, vol. 51, no. 12, pp. 913–915, 1987.

[53] M.Riede, B.Lüssem, and K.Leo, *Comprehensive Semiconductor Science and Technology*, ch. 4.13 - Organic Semiconductors, pp. 448–507. Amsterdam: Elsevier, 2011.

[54] J.-L.Brédas, J.E.Norton, J.Cornil, and V.Coropceanu, "Molecular Understanding of Organic Solar Cells: The Challenges," *Accounts of Chemical Research*, vol. 42, no. 11, pp. 1691–1699, 2009.

[55] M.Riede, C.Uhrich, J.Widmer, R.Timmreck, D.Wynands, G.Schwartz, W.-M.Gnehr, D.Hidebrandt, A.Weiss, J.Hwang, S.Sundarraj, P.Erk, M.Pfeiffer, and K.Leo, "Efficient Organic Tandem Solar Cells based on Small Molecules," *Advanced Functional Materials*, vol. 21, no. 16, pp. 3019–3028, 2011.

[56] V. C. Sundar, J. Zaumseil, V. Podzorov, E. Menard, R. L. Willett, T. Someya, M. E. Gershenson, and J. A. Rogers, "Elastomeric Transistor Stamps: Reversible Probing of Charge Transport in Organic Crystals," *Science*, vol. 303, no. 5664, pp. 1644–1646, 2004.

[57] V. Podzorov, E. Menard, J. A. Rogers, and M. E. Gershenson, "Hall Effect in the Accumulation Layers on the Surface of Organic Semiconductors," *Physical Review Letters*, vol. 95, no. 22, p. 226601, 2005.

[58] O.D.Jurchescu, A.Meetsma, and T.T.M.Palstra, "Low-temperature structure of rubrene single crystals grown by vapor transport," *Acta Crystallographica Section B*, vol. 62, no. 2, pp. 330–334, 2006.

[59] S. Machida, Y. Nakayama, S. Duhm, Q. Xin, A. Funakoshi, N. Ogawa, S. Kera, N. Ueno, and H. Ishii, "Highest-Occupied-Molecular-Orbital Band Dispersion of Rubrene Single Crystals as Observed by Angle-Resolved Ultraviolet Photoelectron Spectroscopy," *Physical Review Letters*, vol. 104, no. 15, p. 156401, 2010.

[60] Y. Okada, K. Sakai, T. Uemura, Y. Nakazawa, and J. Takeya, "Charge transport and Hall effect in rubrene single-crystal transistors under high pressure," *Physical Review B*, vol. 84, no. 24, p. 245308, 2011.

[61] K. A. McGarry, W. Xie, C. Sutton, C. Risko, Y. Wu, V. G. Young, J.-L. Brédas, C. D. Frisbie, and C. J. Douglas, "Rubrene-based single-crystal organic semiconductors: Synthesis, electronic structure, and charge-transport properties," *Chemistry of Materials*, vol. 25, no. 11, pp. 2254–2263, 2013.

[62] B. Lee, Y. Chen, D. Fu, H. T. Yi, K. Czelen, H. Najafov, and V. Podzorov, "Trap healing and ultralow-noise Hall effect at the surface of organic semiconductors," *Nature Materials*, vol. 12, no. 12, pp. 1125–1129, 2013.

[63] S. Karak, J. Ah Lim, S. Ferdous, V. V. Duzhko, and A. L. Briseno, "Photovoltaic Effect at the Schottky Interface with Organic Single Crystal Rubrene," *Advanced Functional Materials*, vol. 24, no. 8, pp. 1039–1046, 2014.

[64] G. Nan, X. Yang, L. Wang, Z. Shuai, and Y. Zhao, "Nuclear tunneling effects of charge transport in rubrene, tetracene, and pentacene," *Physical Review B*, vol. 79, no. 11, p. 115203, 2009.

[65] S. J. Konezny, M. N. Bussac, and L. Zuppiroli, "Trap-limited transport in rubrene transistors," *Applied Physics Letters*, vol. 95, no. 26, p. 263311, 2010.

[66] J. Dacuña, A. Desai, W. Xie, and A. Salleo, "Modeling of the effect of intentionally introduced traps on hole transport in single-crystal rubrene," *Physical Review B*, vol. 89, no. 24, p. 245302, 2014.

[67] C.-H. Lee, T. Schiros, E. J. G. Santos, B. Kim, K. G. Yager, S. J. Kang, S. Lee, J. Yu, K. Watanabe, T. Taniguchi, J. Hone, E. Kaxiras, C. Nuckolls, and P. Kim, "Epitaxial Growth of Molecular Crystals on van der Waals Substrates for high-Performance Organic Electronics," *Advanced Materials*, vol. 26, no. 18, pp. 2812–2817, 2014.

[68] D. D. T. Mastrogiovanni, J. Mayer, A. S. Wan, A. Vishnyakov, A. V. Neimark, V. Podzorov, L. C. Feldman, and E. Garfunkel, "Oxygen Incorporation in Rubrene Single Crystals," *Scientific Reports*, vol. 4, no. 4753, 2014.

[69] A. Girlando, L. Grisanti, M. Masino, I.Bilotti, A.Brillante, R.G.Della Valle, and E.Venuti, "Peierls and Holstein carrier-phonon coupling in crystaline rubrene," *Phys. Rev. B*, vol. 82, no. 3, p. 035208, 2010.

[70] D.Käfer and G.Witte, "Growth of crystalline rubrene films with enhanced stability," *Physical Chemistry Chemical Physics*, vol. 7, no. 15, pp. 2850–2853, 2005.

[71] D.M.Coperley and B.J.Alder, "Ground State of the Electron Gas by a Stochastic Method," *Physical Review Letters*, vol. 45, no. 7, pp. 566–569, 1980.

[72] J.P.Perdew and A.Zunger, "Self-interaction correction to density-functional approximations for many-electron systems," *Physical Review B*, vol. 23, no. 10, pp. 5048–5079, 1981.

[73] Z. Ren, L. McNeil, S. Liu, and C. Kloc, "Molecular motion and mobility in an organic single crystal: Raman study and model," *Physical Review B*, vol. 80, no. 24, p. 245211, 2009.

[74] N.N.Greenwood and A.Earnshaw, *Chemistry of the Elements*. Pergamon Press, 1993.

[75] P.Hagenmuller, "Tungsten and vanadium bronzes," in *Comprehensive Inorganic Chemistry*, vol. 4, Pergamon, 1973.

[76] R. Brusetti, B. K. Chakraverty, J. Devenyi, J. Dumas, J. Marcus, and C. Schlenker, "Transport properties of the Blue Bronze $K_{0.30}MoO_3$," in *Recent Developments in Condensed Matter Physics* (J.T.Deeveese, L.F.Lemmens, V.E.Van Doren, and J.Van Royen, eds.), vol. 2, pp. 181–190, Plenum, New York, 1981.

[77] R.Buder, J. Devenyi, J. Dumas, J. Marcus, J.Mercier, C. Schlenker, and H.Vincent, "Two-dimensional electronic properties of the purple potassium molybdenum bronze $K_{0.9}Mo_6O_{17}$," *Journal de Physique Letters*, vol. 43, no. 2, pp. 69–55, 1982.

[78] N.Witkowski, M.Garnier, D.Purdie, Y.Baer, D.Malterre, and D.Groult, "High-energy-resolution photoemission investigation of monophosphate tungsten bronzes," *Solid State Communications*, vol. 103, no. 8, pp. 471–475, 1997.

[79] P.Roussel, O.Pérez, and Ph.Labbé, "Phosphate tungsten bronze series: crystallographic and structural properties of low-dimensional conductors," *Acta Crystallographica Section B*, vol. 57, no. 5, pp. 603–632, 2001.

[80] C.Schlenker, C. Le Touze, C. Hess, A.Rötger, J. Dumas, J.Marcus, M.Greenblatt, Z.S.Teweldemedhin, A.Ottolenghi, P. Foury, and J.-P.Pouget, "Transport properties of the charge density wave quasi two-dimensional compounds $(PO_2)_4(WO_3)_{2m}$," *Synthetic Metals*, vol. 70, pp. 1263–1266, 1995.

[81] M.Greenblatt, "Monophosphate Tungsten Bronzes. A New Family of Low-Dimensional, Charge-Density-Wave Oxides," *Accounts of Chemical Research*, vol. 29, no. 5, pp. 219–228, 1996.

[82] C. Schlenker, J. Dumas, M. Greenblatt, and S.van Smaalen, eds., *Physics and Chemistry of Low-Dimensional Inorganic Conductors*, vol. 354 of *Nato Science Series B*. Springer US, 1 ed., 1996.

[83] O.Pérez, L.Elcoro, J.M.Pérez-Mato, and V.Petrícek, "Monophosphate tungsten bronzes with pentagonal tunnels: reinvestigation through the peephole of the superspace," *Acta Crystallographica Section B*, vol. 69, no. 2, pp. 122–136, 2013.

[84] J.Beille, U.Beierlein, J. Dumas, C. Schlenker, and D. Groult, "Pressure effect on the charge density wave instabilities in the quasi-two-dimensional conductors $(PO_2)_4(WO_3)_{2m}$ $(m = 4,5,6)$ and $\eta - Mo_4O_{11}$," *Journal of Physics: Condensed Matter*, vol. 13, no. 7, pp. 1517–1527, 2001.

[85] C. Schlenker, C. Hess, C. Le Touze, and J. Dumas, "Charge Density Wave Properties of Quasi Low-Dimensional Transition Metal Oxide Bronzes," *Journal de Physique I (France)*, vol. 6, no. 12, pp. 2061–2078, 1996.

[86] P.Foury-Leylekian and J.-P. Pouget, "Peierls transition in two-dimensional metallic monophosphate tungsten bronzes," *Solid State Sciences*, vol. 4, no. 3, pp. 387–396, 2002.

[87] Q.Yuan, T.Nunner, and T.Kopp, "Imperfect nesting and Peierls instability for a two-dimensional tight-binding model," *The European Physical Journal B*, vol. 22, no. 37, 2001.

[88] P.Foury, J.-P. Pouget, Z.S.Teweldemedhin, E.Wang, M.Greenblatt, and D.Groult, "Charge density wave phenomena in the family of two dimensional monophosphate tungsten bronzes: $(PO_2)_4(WO_3)_{2m}$," *Journal de Physique IV France*, vol. 3, no. C2, pp. 133–136, 1993.

[89] P.Foury-Leylekian, E.Sandré, S.Ravy, J.-P. Pouget, E.Elkaim, P.Roussel, D.Groult, and Ph.Labbé, "Sliding charge density wave in the monophosphate tungsten bronze $(PO_2)_4(WO_3)_{2m}$ with alternate stacking of $m = 4$ and $m = 6$ WO_3 layers," *Physical Review B*, vol. 66, no. 075116, 2002.

[90] E.Canadell and M.-H.Whangbo, "Conceptual Aspects of Structure-Property Correlations and Electronic Instabilities, with Applications to Low-Dimensional Transition-Metal Oxides," *Chemical Reviews*, vol. 91, no. 5, pp. 965–1034, 1991.

[91] J. Dumas, C. Hess, C. Schlenker, G. Bonfait, E. Gomez Marin, D. Groult, and J. Marcus, "Localization effects in the charge density wave state of the quasi-two-dimensional monophosphate tungsten bronzes $(PO_2)_4(WO_3)_{2m}$ $(m = 7,8,9)$," *The European Physical Journal B*, vol. 14, no. 1, pp. 73–82, 2000.

[92] E.Canadell and M-H.Whangbo, "Structural and Electronic Origin of the Hidden Nesting and Charge Density Waves in Transition Metal Oxides and Bronzes," *International Journal of Modern Physics B*, vol. 7, pp. 4005–4043, 1993.

[93] Z.-T.Zhu, J. Musfeldt, Z.S.Teweldemedhin, and M.Greenblatt, "Vibrational Properties of Monophosphate Tungsten Bronzes $(PO_2)_4(WO_3)_{2m}$ $(m = 4,6)$," *Chemistry of Materials*, vol. 13, no. 9, pp. 2940–2944, 2001.

[94] Z.S.Teweldemedhin, K.V.Ramanujachary, and M.Greenblatt, "Anomalous electrical and magnetic behavior in $(PO_2)_4(WO_3)_{2m}$ $(m = 4)$," *Physical Review B*, vol. 46, no. 7897, 1992.

[95] J.P.Giroult, M.Goreaud, Ph.Labbé, and B.Raveau, "$P_4W_8O_{32}$: A Mixed-Valence Tunnel Structure Built up of ReO_3-Type Slabs Connected trough PO_4 Tetrahedra," *Acta Crystallographica Section B*, vol. 37, no. 12, pp. 2139–2142, 1981.

[96] A.Benmoussa, Ph.Labbé, D.Groult, and B.Raveau, "Mixed valence tungsten oxides with a tunnel structure, $P_4W_{4n}O_{12n+8}$: A nonintegral member $P_4W_{10}O_{38}$ $(n = 2.5)$," *Journal of Solid State Chemistry*, vol. 44, no. 3, pp. 318–325, 1982.

[97] Ph.Labbé, M.Goreaud, and B.Raveau, "Monophosphate tungsten bronzes with pentagonal tunnels $P_4W_{12}O_{44}(m = 6)$ and $P_4W_{16}O_{56}(m = 8)$," *Journal of Solid State Chemistry*, vol. 61, no. 3, pp. 324–331, 1986.

[98] S.L.Wang, C.C.Wang, and K.H.Lii, "Crystal structure of WPO_5, the second member of the monophosphate tungsten bronze series $(WO_3)_{2m}(PO_2)_4$," *Journal of Solid State Chemistry*, vol. 82, no. 2, pp. 298–302, 1989.

[99] B.Domengès, M.Harvieu, B.Raveau, and R. Tilley, "The monophosphate tungsten bronzes with pentagonal tunnels $(MPTB_p)$, $P_4O_8(WO_3)_{2m}$: A high-resolution electron microscopy study," *Journal of Solid State Chemistry*, vol. 54, no. 1, pp. 10–28, 1984.

[100] P. Roussel, P. Labbé, and D.Groult, "Symmetry and twins in the monophosphate tungsten bronze series $(PO_2)_4(WO_3)_{2m}$ $(2 \leq m \leq 14)$," *Acta Crystallographica Section B*, vol. 56, pp. 371–391, 2000.

[101] P.Rousel, P. Labbé, H.Leligny, D. Groult, P. Foury-Leylekian, and J.-P. Pouget, "$P_4W_20O_{68}$: A complex charge-density-wave modulated structure with an antiferroelectric-like lattice distortion," *Physical Review B*, vol. 62, no. 176, 2000.

[102] P. Roussel, P. Foury-Leylekian, B. Domengès, D. Groult, P. Labbé, and J.-P. Pouget, "Structural investigation of a new variety of the low dimensional conductor $(PO_2)_4(WO_3)_{2m}$ with $2m = 5 + 5$: $P_4W_{10}O_{38}$," *The European Physical Journal B*, vol. 12, pp. 497–508, 1999.

[103] B.Domengès, F.Studer, and B.Raveau, "$P_4O_8(WO_3)_{2m}$: A series of phosphate tungsten bronzes characterized by empty pentagonal tunnels," *Materials Research Bulletin*, vol. 18, no. 6, pp. 669–676, 1983.

[104] P.Roussel, Ph.Labbé, D.Groult, B.Domengès, H.Leligny, and D.Grebille, "Structural Study of $P_4W_{14}O_{50}$, a New Odd Member in the Series $(PO_2)_4(WO_3)_{2m}$," *Journal of Solid State Chemistry*, vol. 122, no. 2, pp. 281–290, 1996.

[105] P.Roussel, G.Mather, B.Domengès, D.Groult, and P.Labbé, "Structural Investigation of $P_4W_{24}O_{80}$: A New Monophosphate Tungsten Bronze," *Acta Crystallographica Section B*, vol. 54, no. 4, pp. 365–375, 1998.

[106] A.Magnéli, "The Crystal Structure of Mo_4O_{11} (gamma-Molybdenum oxide)," *Acta Chemica Scandinavica*, vol. 2, pp. 861–871, 1948.

[107] L.Kihlborg, "Crystal structure studies on monoclinic and orthorhombic M_4O_{11}," *Arkiv foer Kemi*, vol. 21, pp. 365–377, 1963.

[108] M.Ghedira, H.Vincent, M.Marezio, J.Marcus, and G.Furcaudot, "Structure cristalline du conducteur métallique bidimensionnel Mo_4O_{11}-γ (French)," *Journal of Solid State Chemistry*, vol. 56, no. 1, pp. 66–73, 1985.

[109] M.Greenblatt, "Molybdenum oxide bronzes with quasi-low-dimensional properties," *Chemical Reviews*, vol. 88, no. 1, pp. 31–53, 1988.

[110] E.Canadell, M.-H.Whangbo, C.Schlenker, and C.Escribe-Filippini, "Band Electronic Structure Study of the Electronic Instability in the Magnéli Phase Mo_4O_{11}," *Inorganic Chemistry*, vol. 28, no. 8, pp. 1466–1472, 1989.

[111] G.-H.Gweon, S.-K.Mo, J.W.Allen, C.R.Ast, H.Höchst, J.L.Sarrao, and Z.Fisk, "Hidden one-dimensional electronic structure and non-fermi-liquid angle-resolved photoemission line shapes of $\eta - Mo_4O_{11}$," *Physical Review B*, vol. 72, no. 035126, 2005.

[112] C.Le Touze, G. Bonfait, C. Schlenker, J. Dumas, M. Almeida, M. Greenblatt, and Z. Teweldemedhin, "Quantum Transport in the Charge-Density-Wave State of the Quasi Two-Dimensional Bronzes $(PO_2)_4(WO_3)_{2m}$ $(m = 4,6)$," *Journal de Physique I (France)*, vol. 5, no. 4, pp. 437–442, 1995.

[113] C.Hess, C.Schlenker, J.Dumas, M.Greenblatt, and Z.S.Teweldemedhin, "Magneto-transport and termopower properties of the quasi-two-dimensional charge-density-wave compounds $(PO_2)_4(WO_3)_{2m}$ $(m = 4,6)$," *Physical Review B*, vol. 54, no. 4581, 1996.

[114] U. Beierlein, C. Hess, C. Schlenker, J. Dumas, R. Buder, D. Groult, E. Steep, D. Vignolles, and G. Bonfait, "Charge-density-wave instabilities and quantum transport in the monophosphate tungsten bronzes with $m = 5$ alternate structure," *The European Physical Journal B*, vol. 17, no. 2, pp. 215–226, 2000.

[115] E.Canadell, M-H.Whangbo, and I.El-Idrissi Rachidi, "Similarity of the Electronic Properties of the Monophosphate Tungsten Bronzes," *Inorganic Chemistry*, vol. 29, no. 19, pp. 3871–3875, 1990.

[116] E.Wang, M.Greenblatt, I.El-Idrissi Rachidi, E.Canadell, M.-H.Whangbo, and S.Vadlamannati, "Electronic instabilities of the quasi-two-dimensional monophosphate tungsten bronze $P_4W_{12}O_{44}$," *Physical Review B*, vol. 39, no. 12969(R), 1989.

[117] C. Hess, C. Schlenker, G. Bonfait, T. Ohm, C. Paulsen, D. Dumas, Z. Teweldemedhin, M. Greenblatt, J.Marcus, and M.Almeida, "CDW state and superconductivity in the quasi-two-dimensional monophosphate tungsten bronze $P_4W_{14}O_{50}$," *Solid State Communications*, vol. 104, no. 11, pp. 663–668, 1997.

[118] C.Hess, C.Le Touze, C.Schlenker, J.Dumas, D.Groult, and J.Marcus, "Localization effects in the Peierls state of the quasi two-dimensional compounds," *Synthetic Metals*, vol. 86, no. 1, pp. 2419–2422, 1997.

[119] E.Canadell and M.-H.Whangbo, "On the possible electronic instability of the monophosphate tungsten bronze $(WO_3)_4(PO_2)_4$," *Journal of Solid State Chemistry*, vol. 86, no. 1, pp. 131–134, 1990.

[120] M-H.Whangbo and R.Hoffmann, "The band structure of the tetracyanoplatinate chain," *Journal of the American Chemical Society*, vol. 100, no. 19, pp. 6093–6098, 1978.

[121] E.Sandré, P.Foury-Leylekian, S.Ravy, and J.-P. Pouget, "Ab initio Fermi Surface Calculation for Charge-Density Wave Instability in Transition Metal Oxide Bronzes," *Physical Review Letters*, vol. 86, no. 5100, 2001.

[122] S. Paul, A. Ghosh, T. Sato, D. D. Sarma, T. Takahashi, E. Wang, M. Greenblatt, and S. Raj, "Electronic band structure and Fermi surfaces of the quasi-two-dimensional monophosphate tungsten bronze, $P_4W_{12}O_{44}$," *EPL (Europhysics Letters)*, vol. 105, no. 47003, 2014.

[123] A.Mascaraque, L.Roca, J.Avila, S.Drouard, H.Guyot, and M.C.Asensio, "Electronic structure analysis of quasi-one-dimensional monophosphate tungsten bronzes," *Physical Review B*, vol. 66, no. 115104, 2002.

[124] M-H.Whangbo, E.Canadell, P. Foury, and J.-P. Pouget, "Hidden Fermi Surface Nesting and Charge Density Wave Instability in Low-Dimensional Metals," *Science*, vol. 252, no. 5002, pp. 96–08, 1991.

[125] L.Roca, A.Mascaraque, J.Avila, S.Drouard, H.Goyot, and M.C.Asensio, "Fermi-surface analysis of quasi-two-dimensional monophosphate tungsten bronze," *Physical Review B*, vol. 69, no. 075114, 2004.

[126] J.Lüdecke, A. Jobst, and S. Van Smaalen, "The CDW structure of the $m = 4$ phosphate bronze $(PO_2)_4(WO_3)_{2m}$," *EPL (Europhysics Letters)*, vol. 49, no. 3, pp. 357–361, 2000.

[127] J.Lüdecke, A. Jobst, S.Geupel, and S. van Smaalen, "Structure of the two-dimensional incommensurate charge-density wave in $(PO_2)_4(WO_3)_8$ at 20 K," *Physical Review B*, vol. 64, no. 104105, 2001.

[128] A.Ottolenghi and J.-P. Pouget, "Evidence of High Critical Temperature Charge Density Wave Transitions in the $(PO_2)_4(WO_3)_{2m}$ Family of Low Dimensional Conductors for $m \geq 8$," *Journal de Physique I*, vol. 6, no. 8, pp. 1059–1083, 1996.

[129] B.Domengès, N.K.McGuire, and M.O'Keeffe, "Bond lengths and valences in tungsten oxides," *Journal of Solid State Chemistry*, vol. 56, no. 1, pp. 94–100, 1985.

[130] P.Foury and J.-P. Pouget, "Charge Density Wave Transitions in Two-Dimensional Transition Metal Bronzes and Oxides," *International Journal of Modern Physics B*, vol. 7, pp. 3973–4003, 1993.

[131] P.Foury, P.Roussel, D.Groult, and J.-P. Pouget, "Structural investigation of two varieties of the quasi-2D conductors $(PO_2)_4(WO_3)_{2m}$ $(m = 5)$," *Synthetic Metals*, vol. 103, no. 1, pp. 2624–2627, 1999.

[132] U.Beierlein, C. Schlenker, J.Dumas, and M.Greenblatt, "Fermi surface of the charge-density-wave state of the quasi-two-dimensional monophosphate tungsten bronze $P_4W_{12}O_{44}$," *Physical Review B*, vol. 67, no. 235110, 2003.

[133] J.Lehmann, C.Schlenker, C.Le Touze, A.Rotger, J.Dumas, J.Marcus, Z.S.Teweldemedhin, and M.Greenblatt, "Magnetotransport and specific heat properties in the charge density wave state of the quasi two-dimensional bronzes $(PO_2)_4(WO_3)_{2m}$ $(m = 4,6,7)$," *Journal de Physique IV Colloque*, vol. 3, no. C2, pp. 243–246, 1993.

[134] P.Foury, J.-P.Pouget, E.Wang, and M.Greenblatt, "Charge Density Wave Transitions with Multiple Nesting in the Monophosphate Tungsten Bronzes: $P_4W_{12}O_{44}$ and $P_4W_{14}O_{50}$," *EPL (Europhysics Letters)*, vol. 16, no. 5, p. 485, 1991.

[135] W. L. McMillan, "Landau theory of charge-density waves in transition-metal dichalcogenides," *Physical Review B*, vol. 12, no. 4, pp. 1187–1196, 1975.

[136] R. Chianelli and M. Dines, "Low-temperature solution preparation of group 4B, 5B and 6B transition-metal dichalcogenides," *Inorganic Chemistry*, vol. 17, no. 10, pp. 2758–2762, 1978.

[137] H.Wang, H.Yuan, S.S.Hong, Y.Li, and Y.Cui, "Physical and chemical tuning of two-dimensional transition metal dichalcogenides," *Chemical Society Reviews*, vol. 44, pp. 2664–2680, 2015.

[138] C.Ataca, H.Sahin, and S.Ciraci, "Stable, Single-Layer MX_2 Transition-Metal Oxides and Dichalcogenides in a Honeycomb-Like Structure," *The Journal of Physical Chemistry C*, vol. 116, no. 16, pp. 8983–8999, 2012.

[139] J. Coleman, M. Lotya, A. O'Neill, S. D. Bergin, P. J. King, U. Khan, K. Young, A. Gaucher, S. De, R. J. Smith, I. V. Shvets, S. K. Arora, G. Stanton, H.-Y. Kim, K. Lee, G. T. Kim, G. S. Duesberg, T. Hallam, J. J. Boland, J. J. Wang, J. F. Donegan, J. C. Grunlan, G. Moriarty, A. Shmeliov, R. J. Nicholls, J. M. Perkins, E. M. Grieveson, K. Theuwissen, D. W. McComb, P. D. Nellist, and V. Nicolosi, "Two-dimensional nanosheets produced by liquid exfoliation of layered materials," *Science*, vol. 331, no. 6017, pp. 568–571, 2011.

[140] Q.H.Wang, K.Kalantar-Zadeh, A.Kis, J. N. Coleman, and M.S.Strano, "Electronics and optoelectronics of two-dimensional transition metal dichalcogenides," *Nature Nanotechnology*, vol. 7, no. 11, pp. 699–712, 2012.

[141] I.Žutić, J.Fabian, and S.D.Sarma, "Spintronics: Fundamentals and applications," *Reviews of Modern Physics*, vol. 76, no. 2, pp. 323–410, 2004.

[142] Z.Y.Zhu, Y.C.Cheng, and U.Schwingenschlögl, "Giant spin-orbit-induced spin splitting in two-dimensional transition-metal dichalcogenide semiconductors," *Physical Review B*, vol. 84, no. 15, p. 153402, 2011.

[143] K.Kośmider, J.W.González, and J.Fernández-Rossier, "Large spin splitting in the cundiction band of transition metal dichalcogenide monolayers," *Physical Review B*, vol. 88, no. 24, p. 245436, 2013.

[144] L.F.Mattheiss, "Band Structures of Transition-Metal-Dichalcogenide Layer Compounds," *Physical Review B*, vol. 8, no. 8, pp. 3719–3740, 1973.

[145] L.F.Mattheiss, "Energy Bands for 2H-$NbSe_2$ and 2H-$MoSe_2$," *Physical Review Letters*, vol. 30, no. 17, pp. 784–787, 1973.

[146] H.N.S.Lee, M.García, H.McKinzie, and A.Wold, "The low-temperature electrical and magnetic properties of $TaSe_2$ and $NbSe_2$," *Journal of Solid State Chemistry*, vol. 1, no. 2, pp. 190–194, 1970.

[147] E.Ehrenfreund, A.C.Gossard, F.R.Gamble, and T.H.Geballe, "Absence of Antiferromagnetism in $NbSe_2$ and $TaSe_2$," *Journal of Applied Physics*, vol. 42, no. 4, p. 1491, 1971.

[148] S.Tadaki, N.Hino, T.Sambongi, K.Nomura, and F.Lévy, "Electrical properties of $NbTe_4$ and $TaTe_4$," *Synthetic Metals*, vol. 38, no. 2, pp. 227–234, 1990.

[149] V.Bobnar, P.Lunkenheimer, J.Hemberger, A.Loidl, F.Lichtenberg, and J. Mannhart, "Dielectric properties and charge transport in the $(Sr,La)NbO_{3.5-x}$ system," *Physical Review B*, vol. 65, no. 15, p. 155115, 2002.

[150] F.Lichtenberg, A. Herrnberger, and K.Wiedenmann, "Synthesis, structural, magnetic and transport properties of layered perocskite-related titanates, niobates and tantalates of the type $A_nB_nO_{3n+2}$, $A'A_{k-1}B_kO_{3k+1}$ and $A_mB_{m-1}O_{3m}$," *Progress in Solid State Chemistry*, vol. 36, no. 4, pp. 253–387, 2008.

[151] E.Canadell and M.-H. Whangbo, "Metallic versus nonmetallic properties of ternary chalcogenides: tantalum metal selenide, Ta_2MSe_7 (M= nickel, platinum), and tantalum nickel chalcogenide, Ta_2NiX_5 (X= sulfide, selenide)," *Inorganic Chemistry*, vol. 26, no. 24, pp. 3974–3976, 1987.

[152] F.Lichtenberg, A.Herrnberger, K.Wiedenmann, and J.Mannhart, "Synthesis of perovskite-related layered $A_nB_nO_{3n+2} = ABO_x$ type niobates and titanates and study of their structural, electric and magnetic properties," *Progress in Solid State Chemistry*, vol. 29, pp. 1–70, 2001.

[153] M.D.Johannes and I.I.Mazin, "Fermi surface nesting and the origin of charge density waves in metals," *Physical Review B*, vol. 77, no. 16, p. 165135, 2008.

[154] N.J.Doran, "A calculation of the electronic response function in 2H-$NbSe_2$ including electron-phonon matrix element effects," *Jornal of Physics C: Solid State Physics*, vol. 11, no. 24, pp. 959–962, 1978.

[155] M.D.Johannes, I.I.Mazin, and C.A.Howells, "Fermi-surface nesting and the origin of the charge-density wave in $NbSe_2$," *Physical Review B*, vol. 73, no. 20, p. 205102, 2006.

[156] F.W.Boswell, A.Prodan, and J.K.Brandon, "Charge-density waves in the quasi-one-dimensional compounds $NbTe_4$ and $TaTe_4$," *Jornal of Physics C: Solid State Physics*, vol. 16, no. 6, pp. 1067–1076, 1983.

[157] D. J. Eaglesham, D. Bird, R. L. Withers, and J. W. Steeds, "Microstructural behaviour in the CDW states of $NbTe_4$ and $TaTe_4$; domains, discommensurations and superlattice symmetry," *Journal of Physics C: Solid State Physics*, vol. 18, no. 1, p. 1, 1985.

[158] R.L.Withers and J.A.Wilson, "An examination of the formation and characteristics of charge-density waves in inorganic materials with special reference to the two- and one-dimensional transition-metal chalcogenides," *Journal of Physics C: Solid State Physics*, vol. 19, no. 25, pp. 4809–4845, 1986.

[159] A.Spijkerman, A.Meetsma, J.L.de Boer, Y.Gao, and S. van Smaalen, "Modulated structure of $NiTa_2Se_7$ in its incommensurate charge-density-wave state at 16 K," *Physical Review B*, vol. 52, no. 6, pp. 3892–3899, 1995.

[160] Z.Dai, C.G.Slough, W.W.McNairy, and R.V.Coleman, "Charge-density-wave formation in Ta_2NiSe_7 studied by scanning tunneling microscopy," *Physical Review Letters*, vol. 69, no. 12, pp. 1769–1772, 1992.

[161] C. A. Kuntscher, S. Schuppler, P. Haas, B. Gorshunov, M. Dressel, M. Grioni, F. Lichtenberg, A. Herrnberger, F. Mayr, and J. Mannhart, "Extremely Small Energy Gap in the Quasi-One-Dimensional Conducting Chain Compound $SrNbO_{3.41}$," *Physical Review Letters*, vol. 89, no. 23, p. 236403, 2002.

[162] C.A.Kuntscher, S.Schuppler, P.Haas, B.Gorshunov, M.Dressel, M.Grioni, and F.Lichtenberg, "Electronic and vibrational properties of the low-dimensional perovskites $Sr_{1-y}La_yNbO_{3.5-x}$," *Physical Review B*, vol. 70, no. 24, p. 245123, 2004.

[163] J.-E. Weber, C.Kegler, N.Büttgen, H.-A.Krug fon Nidda, A.Loidl, and F.Lichtenberg, "NMR, EPR, and bulk susceptibility measurements of one-dimensional $SrNbO_{3.41}$," *Physical Review B*, vol. 64, no. 23, p. 235414, 2001.

[164] A.Sakai, T.Kanno, K.Takahashi, Y.Yamada, and H.Adachi, "Large anisotropic thermoelectricity in perovskite related layered structure: $Sr_nNb_nO_{3n+2}$ $(n = 4, 5)$," *Journal of Applied Physics*, vol. 108, no. 10, p. 103706, 2010.

[165] J.Guevarra, S. van Smaalen, N.Rotiroti, C.Paulmann, and F.Lichtenberg, "Crystal structure of $Ca_5Nb_5O_{17}$," *Journal of Solid State Chemistry*, vol. 178, no. 9, pp. 2934–2941, 2005.

[166] N.Ishizawa, F.Marumo, T.Kawamura, and M.Kimura, "The Crystal Structure of $Sr_2Nb_2O_7$, a Compound with Perovskite-Type Slabs," *Acta Crystallographica Section B*, vol. 31, no. 7, pp. 1912–1915, 1975.

[167] M.Gasperin, "Dititanate de Lanthane (French)," *Acta Crystallographica Section B*, vol. 31, no. 8, pp. 2129–2130, 1975.

[168] H.W.Schmalle, T.Williams, A.Reller, A.Linden, and J.G.Bednorz, "The twin structure of $La_2Ti_2O_7$: X-ray and transmission electron microscopy studies," *Acta Crystallographica Section B*, vol. 49, no. 2, pp. 235–244, 1993.

[169] C.A.Kuntscher, S.Gerhold, N.Nücker, T.R.Cummins, D.-H.Lu, S.Schuppler, C.S.Gopinath, F.Lichtenberg, J.Mannhart, and K.-P.Bohnen, "Electronic structure of layered perovskite-related $Sr_{1-y}La_yNbO_{3.5-x}$," *Physical Review B*, vol. 61, no. 3, pp. 1876–1883, 2000.

[170] H.Winter, S.Schuppler, and C.A.Kuntscher, "The electronic structure and the O 1*s* x-ray absorption cross section of the perovskite-derived compound $SrNbO_{3.4}$," *Journal of Physics: Condensed Matter*, vol. 12, no. 8, pp. 1735–1751, 2000.

[171] G.Tobias and E.Canadell, "Nature of the Bottom t_{2g}-Block Bands of Layered Perovskites. Implications for the Transport Properties of Phases Where These Bands Are Partually Filled," *Journal of the American Chemical Society*, vol. 128, no. 13, pp. 4318–4329, 2006.

[172] D.Sánchez-Portal, P.Ordejón, and E.Canadell, *Principles and Applications of Density Functional Theory in Inorganic Chemistry II*, vol. 113 of *Structure and Bonding*, ch. Computing the Properties of Materials from First Principles with SIESTA, pp. 103–170. Springer Berlin Heidelberg, 2004.

[173] H.W.Schmalle, T.Williams, A.Reller, F.Lichtenberg, D.Widmer, and J.G.Bednorz, "A Novel Semiconducting Perovskite-Related Phase: $Sr_5Nb_5O_{17}$," *Acta Crystallographica Section C*, vol. C51, pp. 1243–1246, 1995.

[174] S.C.Abrahams, H.W.Schmalle, T.Williams, A.Reller, F.Lichtenberg, D.Widmer, J.G.Bednorz, R.Spreiter, Ch.Bosshard, and P.Günter, "Centrosymmetric or Noncentrosymmetric? Case Study, Generalization and Structural Redetermination of $Sr_5Nb_5O_{17}$," *Acta Crystallographica Section B*, vol. B54, no. 399-416, 1998.

[175] R.Rousseau, M.R.Palacín, P.Gómez-Romero, and E.Canadell, "Electronic Structure of Layered Oxides Containing M_2O_7 $(M = V, Nb)$ Double Octahedral Slabs," *Inorganic Chemistry*, vol. 35, no. 5, pp. 1179–1184, 1996.

[176] E.Revolinsky, E.P.Lautenschlager, and C.H.Armitage, "Layer structure superconductor," *Solid State Communications*, vol. 1, no. 3, pp. 59–61, 1963.

[177] E.Revolinsky, G.A.Spiering, and D.J.Beerntsen, "Superconductivity in the niobium-selenium system," *Journal of Physics and Chemistry of Solids*, vol. 26, no. 6, pp. 1029–1034, 1965.

[178] T.Yokoya, T.Kiss, A.Chainani, S.Shin, M.Nohara, and H.Takagi, "Fermi Surface Sheet-Dependent Superconductivity in $2H$-$NbSe_2$," *Science*, vol. 294, no. 5551, pp. 2518–2520, 2001.

[179] Y.Noat, J.A.Silva-Guillén, T.Cren, V.Cherkez, C.Brun, S.Pons, F.Debontridder, D.Roditchev, W.Sacks, L.Cario, P.Ordejón, A.García, and E.Canadell, "Quasiparticle spectra of $2H$-$NbSe_2$: Two-band superconductivity and the role of tunneling selectivity," *Physical Review B*, vol. 92, no. 13, p. 134510, 2015.

[180] C.L.Huang, J.-Y.Lin, Y.T.Chang, C.P.Sun, H.Y.Shen, C.C.Chou, H.Berger, T.K.Lee, and H.D.Yang, "Experimental evidence for a two-gap structure of superconducting $NbSe_2$: A specific-heat study in external magnetic fields," *Physical Review B*, vol. 76, no. 21, p. 212504, 2007.

[181] J.A.Wilson, F.J.Di Salvo, and S.Mahajan, "Charge-density waves and superlattices in the metallic layered transition metal dichalcogenides," *Advances in Physics*, vol. 24, no. 2, pp. 117–201, 1975.

[182] J.A.Wilson, F.J.Di Salvo, and S.Mahajan, "Charge-Density Waves in Metallic, Layered, Transition-Metal Dichalcogenides," *Physical Review Letters*, vol. 32, no. 16, pp. 882–885, 1974.

[183] K.Rossnagel, E.Rotenberg, H.Koh, N.V.Smith, and L.Kipp, "Fermi-surface, charge-density-wave gap, and kinks in $2H$-$TaSe_2$," *Physical Review B*, vol. 72, no. 12, p. 121103, 2005.

[184] C.J.Arguello, S.P.Chockalingam, E.P.Rosenthal, L.Zhao, C.Gutiérrez, J.H.Kang, W.C.Chung, R.M.Fernandes, S.Jia, A.J.Millis, R.J.Cava, and A.N.Pasupathy, "Visualizing the charge density wave transition in $2H$-$NbSe_2$ in real space," *Physical Review B*, vol. 89, no. 23, p. 235115, 2014.

[185] K. Rossnagel, O. Seifarth, L. Kipp, M. Skibowski, D. Voss, P. Krüger, A. Mazur, and J. Pollmann, "Fermi surface of $2H$-$NbSe_2$ and its implications on the charge-density-wave mechanism," *Physical Review B*, vol. 64, no. 23, p. 235119, 2001.

[186] T.M.Rice and G.K.Scott, "New Mechanism for a Charge-Density-Wave Instability," *Physical Review Letters*, vol. 35, no. 2, pp. 120–123, 1975.

[187] N.J.Doran, D.J.Titterington, B.Ricco, and G.Wexler, "A tight binding fit to the band-structure of $2H$-$NbSe_2$ and $NbSe_2$," *Journal of Physics C: Solid State Physics*, vol. 11, no. 4, pp. 685–698, 1978.

[188] D. E. Moncton, J. D. Axe, and F. J. Di Salvo, "Study of Superlattice Formation in $2H$-$NbSe_2$ and $2H$-$TaSe_2$ by Neutron Scattering," *Physical Review Letters*, vol. 34, no. 12, pp. 734–737, 1975.

[189] C.D.Malliakas and M.G.Kanatzidis, "*Nb-Nb* Interactions Define the Charge Density Wave Structure of $2H$-$NbSe_2$," *Journal of the American Chemical Society*, vol. 135, no. 5, pp. 1719–1722, 2013.

[190] M.M.Ugeda, A.J.Bradley, Y.Zhang, S.Onishi, Y.Chen, W.Ruan, C.Ojeda-Aristizabal, H.Ryu, M.T.Edmonds, H.-Z.Tsai, A.Riss, S.-K.Mo, D.Lee, A.Zetti, Z.Hussain, Z.-X.Shen, and M.F.Crommie, "Characterization of collective ground states in single-layer $NbSe_2$," *Nature Physics*, vol. 12, no. 1, pp. 92–97, 2016.

[191] Y.Cao, A.Mishchenko, G.L.Yu, E.Khestanova, A.P.Rooney, E.Prestat, A.V.Kretinin, P.Blake, M.B.Shalom, C.Woods, J.Chapman, G.Balakrishnan, I.V.Grigorieva, K.S.Novoselov, B.A.Piot, M.Potemski, K.Watanabe, T.Taniguchi, S.J.Haigh, A.K.Geim, and R.V.Gorbachev, "Quality Heterostructures from Two-Dimensional Crystals Unstable in Air by Their Assembly in Inert Atmosphere," *Nano Letters*, vol. 15, no. 8, pp. 4914–4921, 2015.

[192] R.F.Frindt, "Superconductivity in Ultrathin $NbSe_2$ Layers," *Physical Review Letters*, vol. 28, no. 5, pp. 299–301, 1972.

[193] N.E.Staley, J.Wu, P.Eklund, Y.Liu, L.Li, and Z.Xu, "Electric field effect on superconductivity in atomically thin flakes of $NbSe_2$," *Physical Review B*, vol. 80, no. 18, p. 184505, 2009.

[194] M. Marezio, P. Dernier, A. Menth, and G. Hull Jr., "The crystal structure of $NbSe_2$ at 15°K," *Journal of Solid State Chemistry*, vol. 4, no. 3, pp. 425–429, 1972.

[195] R.Corcoran, P.J.Meeson, Y.Onuki, P.A.Probst, M.Springford, K.Takita, H.Harima, G.Y.Guo, and B.L.Gyorffy, "Quantum oscilations in the mixed state of the type II superconductor 2H-$NbSe_2$," *Journal of Physics: Condensed Matter*, vol. 6, pp. 4479–4492, 1994.

[196] S.Lebègue and O.Eriksson, "Electronic structure of two-dimensional crystals from ab initio theory," *Physical Review B*, vol. 79, no. 11, p. 115409, 2009.

[197] M.Calandra, I.I.Mazin, and F.Mauri, "Effect of dimensionality on the charge-density wave in few-layer 2H-$NbSe_2$," *Physical Review B*, vol. 80, no. 24, p. 241108, 2009.

[198] M.-H.Whangbo and E.Canadell, "Analogies between the Concepts of Molecular Chemistry and Solid-State Physics concerning Structural Instabilities. Electronic Origin of the Structural Modulations in Layered Transition-Metal Dichalcogenides," *Journal of the American Chemical Society*, vol. 114, no. 24, pp. 9587–9600, 1992.

[199] J. M. E. Harper, T. H. Geballe, and F. J. Di Salvo, "Heat capacity of 2H-$NbSe_2$ at the charge density wave transition," *Physics Letters A*, vol. 54, no. 1, pp. 27–28, 1975.

[200] J. R. Long, S. P. Bowen, and N. E. Lewis, "Anomalous resistivity of iodine-free 2H-$NbSe_2$," *Solid State Communications*, vol. 22, no. 6, pp. 363–366, 1977.

[201] P.M.Williams, C.B.Scruby, and G.J.Tatlock, "Charge density waves in 2H-$NbSe_2$," *Solid State Communications*, vol. 17, no. 9, pp. 1197–1200, 1975.

[202] N.J.Doran, D.J.Titterington, B.Ricco, M.Schreiber, and G.Wexler, "The electronic susceptibility and charge density waves in 2H layer compound," *Journal of Physics C: Solid State Physics*, vol. 11, no. 4, pp. 699–705, 1978.

[203] J.A.Silva-Guillén, P.Ordejón, F.Guinea, and E.Canadell, "Electronic structure of 2H-$NbSe_2$ single-layers in the CDW," *2D Materials*, vol. 3, no. 3, p. 035028, 2016.

[204] K.Rossnagel, "On the origin of charge-density waves in select layered transition-metal dichalcogenides," *Journal of Physics: Condensed Matter*, vol. 23, no. 21, p. 213001, 2011.

[205] K.Selte and A.Kjekshus, "On the Crystal Structure of $NbTe_4$," *Acta Chemica Scandinavica*, vol. 18, no. 3, pp. 690–696, 1964.

[206] E.Bjerkelund and A.Kjekshus, "On the crystal structure of $TaTe_4$," *Journal of the Less Common Metals*, vol. 7, no. 3, pp. 231–234, 1964.

[207] T.Sambongi, S.Tadaki, N.Hino, and K.Nomura, "Shubnikov de Haas study of $TaTe_4$," *Synthetic Metals*, vol. 58, no. 1, pp. 109–114, 1993.

[208] K.D.Bronsema, S.Van Smaalen, J. De Boer, G.A.Wiegers, F.Jellinek, and J.Mahy, "The determination of the commensurately modulated structure of tantalum tetratelluride," *Acta Crystallographica Section B*, vol. 43, no. 4, pp. 305–313, 1987.

[209] S. van Smaalen, K.D.Bronsema, and J.Mahy, "The determination of the incommensurately modulated structure of niobium tetrateluride," *Acta Crystallographica Section B*, vol. 42, no. 1, pp. 43–50, 1986.

[210] F.W.Boswell and A.Prodan, "Charge-density-waves of variable incommensurability in the system $TaTe_4$ $NbTe_4$," *Materials Research Bulletin*, vol. 19, no. 1, pp. 93–97, 1984.

[211] J.Kusz and H.Böhm, "The Low Temperature Structure of $NbTe_4$," *Acta Crystallographica Section B*, vol. 50, no. 6, pp. 649–655, 1994.

[212] D.W.Bullett, "*p-d* band overlap and the electronic structure of $NbTe_4$," *Journal of Physics C: Solid State Physics*, vol. 17, no. 2, pp. 253–257, 1984.

[213] M.-H.Whangbo and P.Gressier, "Band structure of niobium tetratelluride ($NbTe_4$)," *Inorganic Chemistry*, vol. 23, no. 9, pp. 1228–1232, 1984.

[214] M.B.Walker and R.Morelli, "$NbTe_4$: A model for a class of incommensurate-to-incommensurate phase transitions," *Physical Review B*, vol. 38, no. 7, pp. 4836–4839, 1988.

[215] F.Zwick, H.Berger, M.Grioni, G.Margaritondo, L. Forró, J. LaVeigne, D. B. Tanner, and M. Onellion, "Coexisting one-dimensional and three-dimensional spectral signatures in $TaTe_4$," *Physical Review B*, vol. 59, no. 11, pp. 7762–7766, 1999.

[216] T.Sörgel, J.Nuss, U.Wedig, R.K.Kremer, and M.Jansen, "A new low temperature modification of $TaTe_2$ - Comparison to the room temperature and the hypothetical 1T-$TaTe_2$ modification," *Materials Research Bulletin*, vol. 41, pp. 987–1000, 2006.

[217] E. Canadell, S. Jobic, R. Brec, J. Rouxel, and M. Whangbo, "Importance of short layer *Te–Te* contacts for the structural distortions and physical properties of CdI_2-type layered transition-metal ditellurides," *Journal of Solid State Chemistry*, vol. 99, no. 1, pp. 189–199, 1992.

[218] P. Monçeau, N. P. Ong, A. M. Portis, A. Meerschaut, and J. Rouxel, "Electric Field Breakdown of Charge-Density-Wave-Induced Anomalies in $NbSe_3$," *Physical Review Letters*, vol. 37, no. 10, pp. 606–606, 1976.

[219] A.Meerschaut, L.Guemas, and J.Rouxel, "Structure and properties of the new phase of the pseudo one-dimensional compound TaS_3," *Journal of Solid State Chemistry*, vol. 36, no. 1, pp. 118–123, 1981.

[220] J.A.Wilson, "Bands, bonds and charge-density waves in the $NbSe_3$ family of compounds," *Physical Review B*, vol. 19, no. 12, pp. 6456–6468, 1979.

[221] S.A.Sunshine, D. Keszler, and J.A.Ibers, "Coordination Chemistry and the Solid State," *Accounts of Chemical Research*, vol. 20, no. 11, pp. 395–400, 1987.

[222] A.P.Tiwari, D.Kim, Y.Kim, O.Prakash, and H. Lee, "Highly active and stable layered ternary transition metal chalcogenide for hydrogen evolution reaction," *Nano Energy*, vol. 28, pp. 366–372, 2016.

[223] M.A.Pell and J.A.Ibers, "Layered ternary and quaternary metal chalcogenides," *Chemische Berichte*, vol. 130, no. 1, pp. 1–8, 1997.

[224] D.A.Keszier, J.A.Ibers, S.Maoyu, and L.Jiaxi, "New ternary and quaternary transition-metal selenides: Synthesis and characterization," *Journal of Solid State Chemistry*, vol. 57, no. 1, pp. 68–81, 1985.

[225] S.A.Sunshine and J.A.Ibers, "Synthesis, structure and transport properties of tantalum nickel selenide (Ta_2NiSe_7) and tantalum platinum selenide (Ta_2PtSe_7)," *Inorganic Chemistry*, vol. 25, no. 24, pp. 4355–4358, 1986.

[226] S.J.Hillenius, R.V.Coleman, R.M.Fleming, and R.J.Cava, "Metal-insulator transition and charge-density wave in $Fe_{0.25}Nb_{0.75}Se_3$," *Physical Review B*, vol. 23, no. 4, pp. 1567–1575, 1981.

[227] R.M.Fleming, S.A.Sunshine, C.H.Chen, L.F.Schneemeyer, and J.V.Waszczak, "Defect-inhabited incommensurate distortion in Ta_2NiSe_7," *Physical Review B*, vol. 42, no. 8, pp. 4954–4959, 1990.

Appndx A

Electron-phonon coupling in rubrene

On the Figures A.1, A.2 and A.3 are shown the results of the electron-phonon coupling calculation in rubrene for the X, Y and Z points of the Brillouin zone. As for the Γ point, Figure 3.6, the highest electron-phonon coupling constants are coming from the low frequency modes.

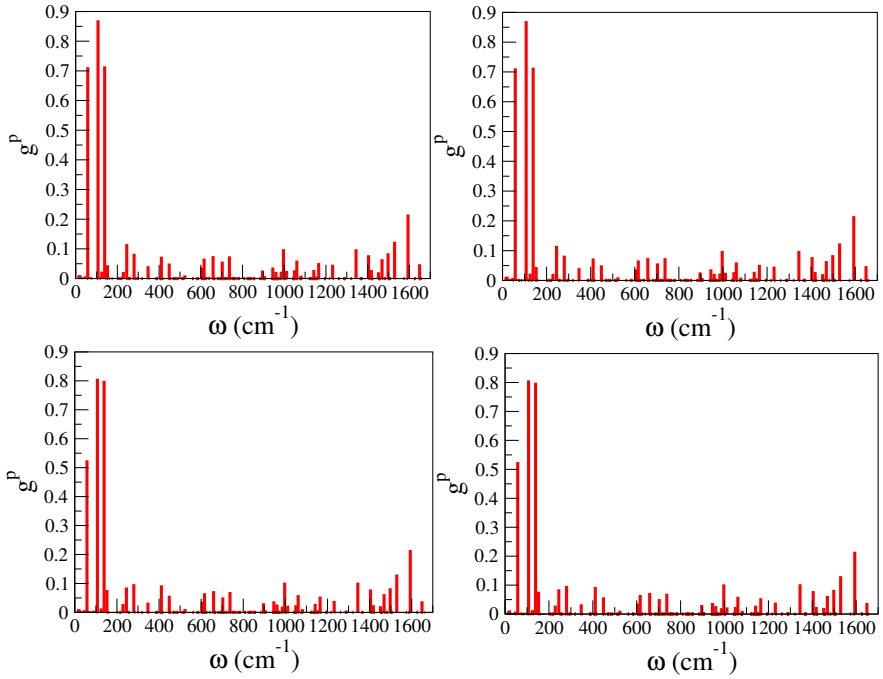

Fig. A.1 Calculated electron-phonon coupling constants g for the four molecules of rubrene as a function of phonon frequencies ω for the X point of the Brillouin zone. The highest electron-phonon coupling constants are coming from the three low-frequency modes with averaged coupling constants: $g^{107.3} = 0.84$, $g^{139.1} = 0.76$ and $g^{57.8} = 0.62$.

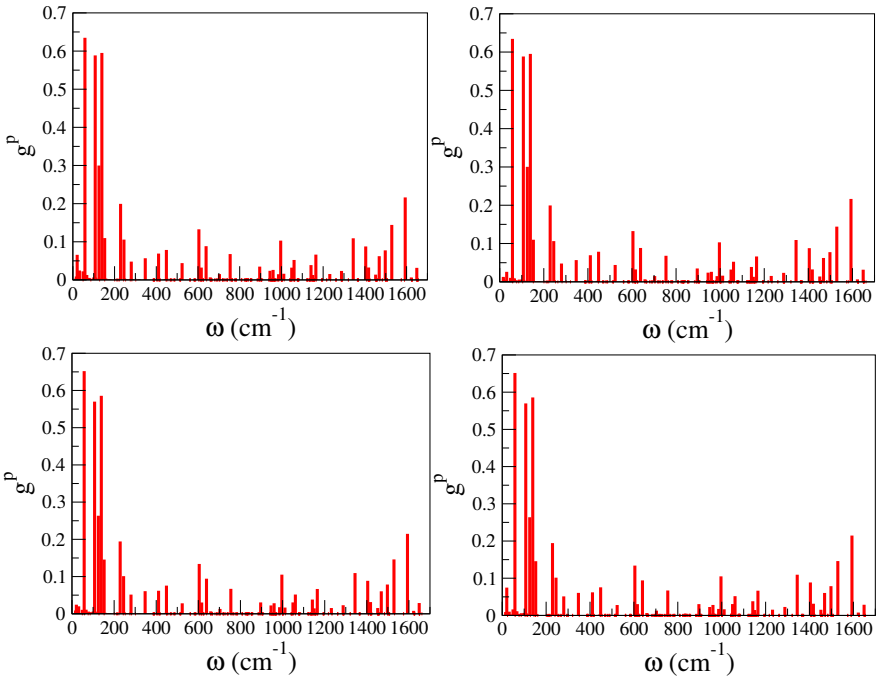

Fig. A.2 Calculated electron-phonon coupling constants g as a function of phonon frequencies ω for the Y point of the Brillouin zone with the highest coupling constants: $g^{107.3} = 0.58$, $g^{139.1} = 0.60$ and $g^{57.8} = 0.64$.

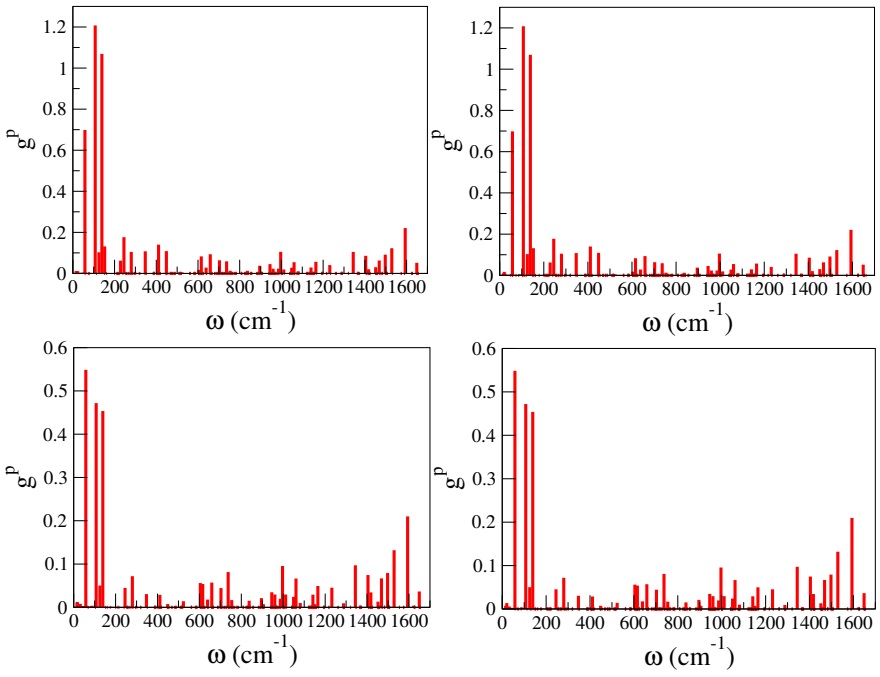

Fig. A.3 Calculated electron-phonon coupling constants g as a function of phonon frequencies ω for the Z point of the Brillouin zone. The highest coupling constants calculated for the Z point are: $g^{107.3} = 0.84$, $g^{139.1} = 0.76$ and $g^{57.8} = 0.62$.

Appndx B

Molecular dynamics simulations

The influence of finite temperature on the phenyl group dynamics was analysed by studying their motions with Molecular dynamics simulations. For these simulations we were following the change of the angles defined as in the Figure 3.10 in the Chapter 3 over time for different temperatures. On the Figures B.1a, B.1b, B.2a and B.2b are shown results of the phenyl group dynamics at 100K, 200K, 300K and 500K.

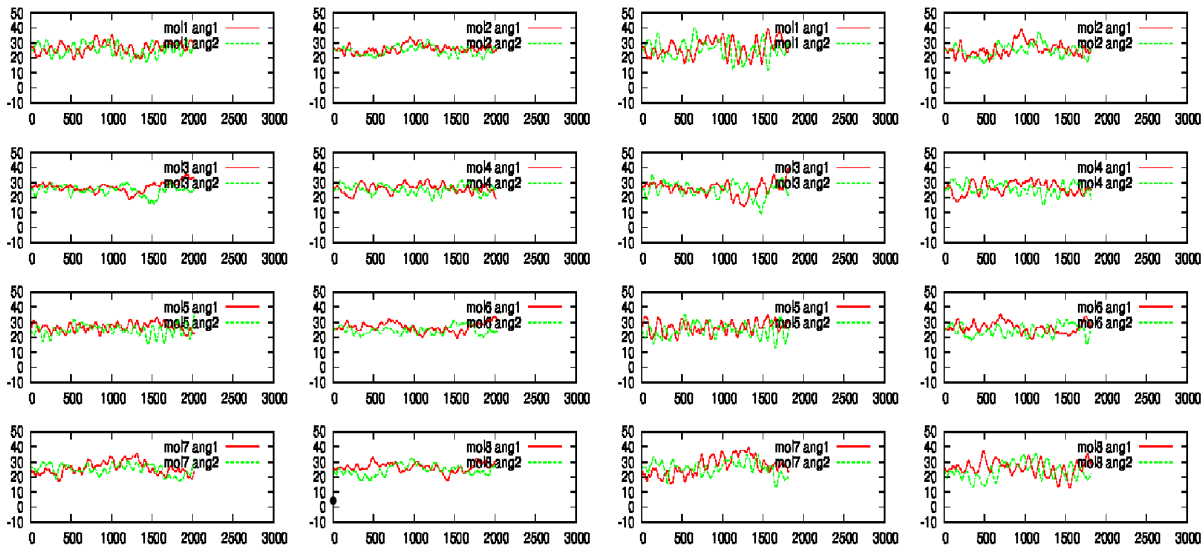

(a) $T = 100$K (b) $T = 200$K

Fig. B.1 Phenyl group dynamics measured with angles ang_1 (red) and ang_2 (green) at 100K and 200K. Eight graphs on each figure correspond to the eight molecules of the supercell.

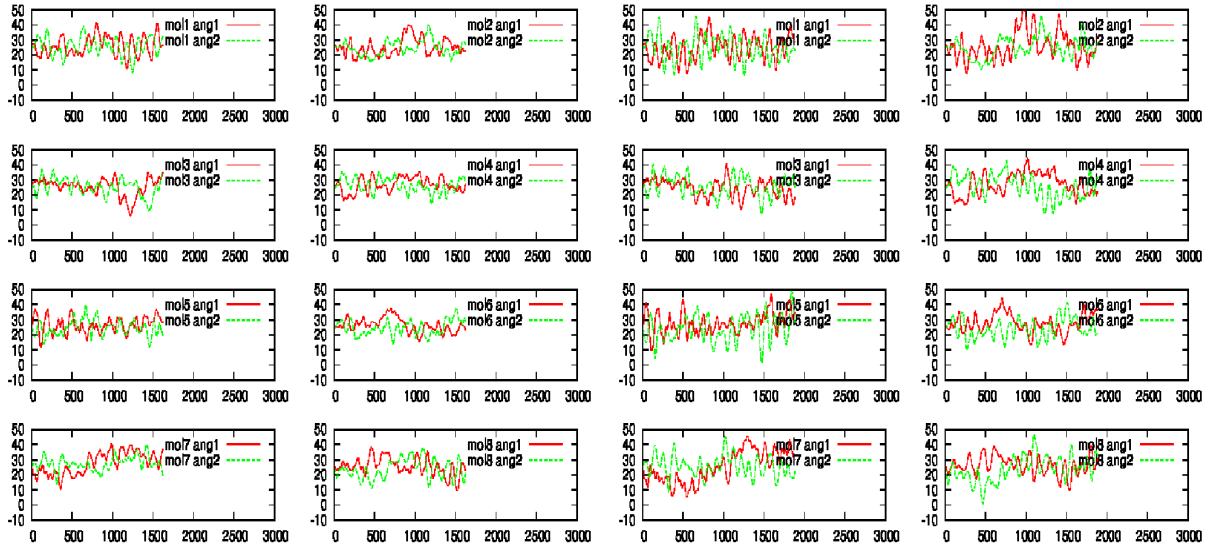

(a) $T = 300$K (b) $T = 500$K

Fig. B.2 Phenyl group dynamics measured with angles ang_1 (red) and ang_2 (green) at 300K and 500K.

Appndx C

Lindhard response function calculation at finite temperatures

In the Chapter 2 Section 2.5 we defined the LIndhard response function with the equation 2.56:

$$\chi(\vec{q}) = -\frac{1}{(2\pi)^d}\int_{1BZ} d\vec{k}\frac{f(\vec{k}+\vec{q})-f(\vec{k})}{E_{\vec{k}+\vec{q}}-E_{\vec{k}}}$$

When the Fermi surface is nested a quasi-1D material at $T = 0$K is energetically unstable and reduces its energy by developing a CDW. This is followed with opening of energy gap on the Fermi surface at the positions $\pm k_F$. Increasing the temperature, some electrons become thermally excited across the energy gap. This lowers the reduction in energy associated with the CDW formation and eventually quenches the CDW at the transition temperature, T_p.

The $MPTB_p$ member with $m = 6$, $P_4W_{12}O_{44}$, has three Peierls instabilities: at $T_{p1} = 120$K, $T_{p2} = 62$K and $T_{p3} = 30$K. In the Chapter 4 section 4.4.3 we gave results of the Lindhard response function calculation for $m = 6$ member at $T = 0$K. Here are shown results of the Lindhard calculation for this $MPTB_p$ member at several different temperatures: 50K, 150K, 300K and 500K. Going from the Figure C.1a to the Figure C.1d we can see that increasing the temperature sharp peaks are gradually becoming broad maxima, which is in the agreement with the equation 2.59 as $\chi \sim 1/T$.

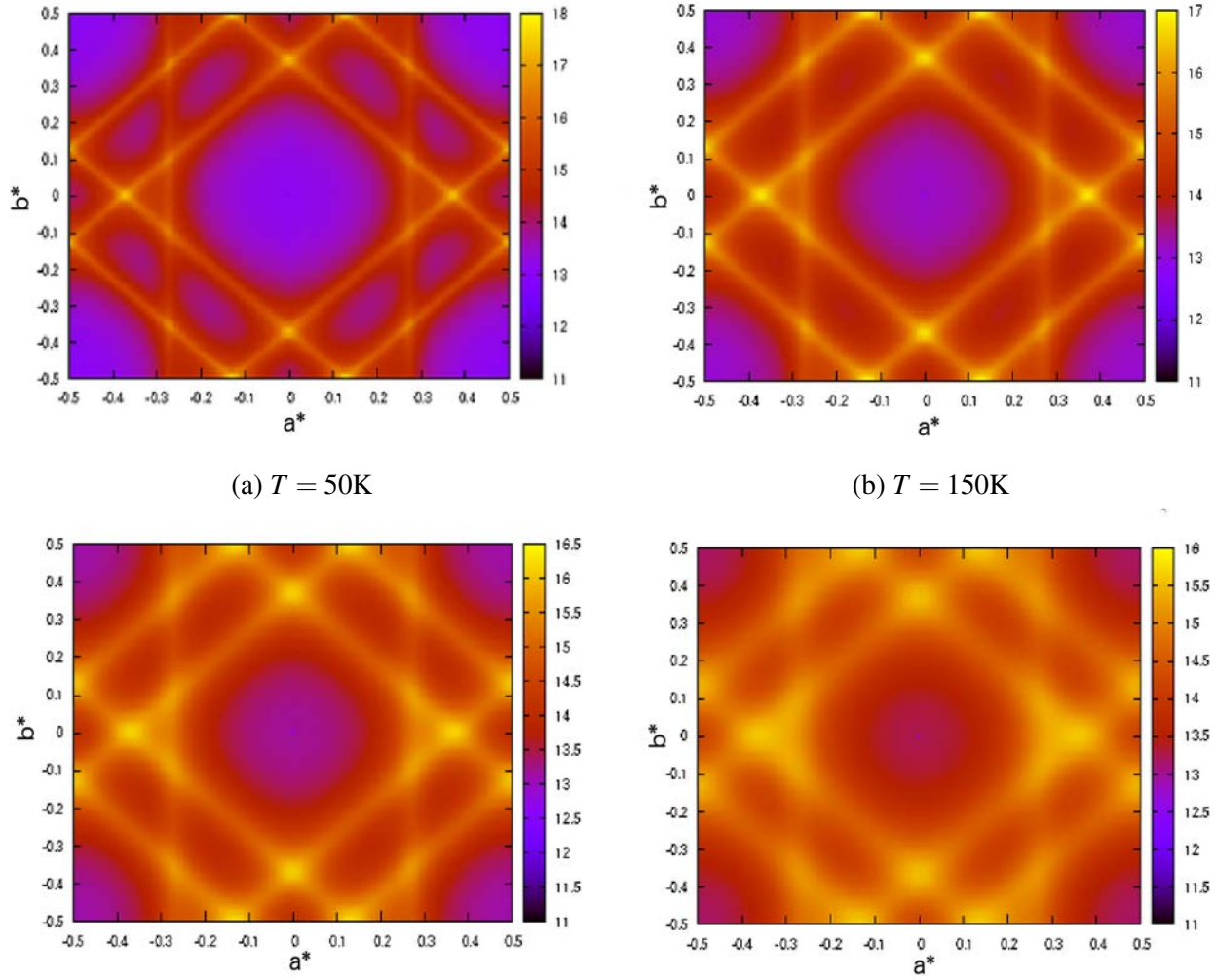

(a) $T = 50$K

(b) $T = 150$K

(c) $T = 300$K

(d) $T = 500$K

Fig. C.1 (a^*, b^*) section of the Lindhard response function calculated for $P_4W_{12}O_{44}$ at different temperatures.